UNIVERSITÀ DEGLI STUDI DI PADOVA

FACOLTÀ DI INGEGNERIA

Corso di Laurea Magistrale in Ingegneria dei Materiali

Dipartimento di Ingegneria Industriale

Tesi di Laurea Magistrale

Development of porous refractory targets for nuclear physics and medical applications

Relatore: Prof. Paolo Colombo

Correlatori: Dott. Stefano Corradetti

Dott. Alberto Andrighetto

Laureando: Alberto Girotto

A.A. 2016-2017

Abstract

This thesis is dedicated to develop porous refractory target materials characterized by a high isotopes release efficiency for the SPES project, which is aimed to produce radioactive ion beams useful for nuclear physics research, as well as for other applications in different branches of science. Specifically, three ceramic materials will be discussed: zirconium carbide, zirconium germanide and titanium carbide.

Zirconium carbide and zirconium germanide disc-shaped targets production stages consist of powders mixture preparation, pressing and heat treatment, therefore the optimization of each of these phases will be described.

Titanium carbide circular-shaped targets will be produced by additive manufacturing for the first time in SPES history. In particular, this production method allows the realization of 3D structure controlled targets helpful to maximize the isotopes release efficiency.

These materials will be characterized performing SEM, EDS and XRD analysis, moreover physisorption will be used to evaluate the porosity features of zirconium carbide targets, while a permeability measurement will define the permeability of titanium carbide 3D targets.

Most of this thesis work was developed at *Istituto Nazionale di Fisica Nucleare (INFN)*, *Laboratori Nazionali di Legnaro (LNL)* in which the production stages of both zirconium carbide and zirconium germanide, and all the aforementioned characterization techniques (XRD excluded) were performed. Delta Wasp 2040 Turbo®and X-Ray Diffractometer were available at Department of Industrial Engineering, University of Padova.

Contents

Introduction

Research in nuclear physics aims at the understanding of the rich variety of phenomena exhibited by the atomic nucleus leading to the development of new technologies and applications that can be useful in our common life experience.
This field of research in Italy is mainly represented by INFN (*Istituto Nazionale di Fisica Nucleare*) which often collaborates with CERN (*Organisation Européenne pour la Recherche Nucléaire*), that is the world's largest particle physics laboratory, and other several international institutes.
In particular SPES (*Selective Production of Exotic Species*) is one of the most important project purposed by INFN: it is located at LNL (*Laboratori Nazionali di Legnaro*) and its aim is to develop a Radioactive Ion Beam (RIB) facility as an intermediate step to cover interdisciplinary applied physics in the fields of material science and medical applications.
The facility provides and delivers to users both proton-rich and neutron-rich nuclei (range of mass 80-160 amu) employed for nuclear physics research, as well as other applications in different branches of science. The isotopes generation occurs by nuclear reactions inside a properly designed target thanks to the interaction with the primary beam provided by a driver accelerator. The reaction products are extracted from the target by thermal process due to the high temperature of the target-ion source system (exceeding 2000 °C). Thus the target's material selection and its properties are of fundamental importance in determining the quantity and type of the produced isotopes and it is the core of the whole project.
The synthesis and characterization of new target concepts and materials in order to satisfy the requirements imposed by the facility is presented in this work. Chapter 1 gives a general overview of the SPES project and the related ISOLPHARM project, while chapter 2 introduces the main topics related to the on-line behavior of the SPES target, relative to both its layout and to the properties of the material constituting it. Chapter 3 explains the importance of the materials which are treated in this work; Finally, Chapters 4,5,6 present the methods to synthesize and characterize rispectively Zirconium Carbide, Titanium carbide 3D printed with additive manufacturing and Zirconium Germanide.

CHAPTER 1

SPES and ISOLPHARM projects at Legnaro National Laboratories

1.1 Introduction

The atom nucleus contains most of the mass of the whole atom (about the 99%). It is composed of nucleons having different electronic charge: positively charged particles (protons, p) and neutral particles (neutrons, n), whose masses are very similar to each other $\left(1.67 \cdot 10^{-27} Kg\right)$. These particles are bound together by the strong interaction, the most intense above all the fundamental forces acting in nature – the others are gravitation, electromagnetism and weak interaction - thus guaranteeing the stability of the nucleus. The ratio between the number of protons (Z) and neutrons (N) establishes the stability of the nucleus: the nuclide chart (Figure 1.1) represents with the x axis the neutron number , while with the y axis the proton number, and it shows with the black squares the stable or extremely long-lived nuclei, forming the so-called "valley of stability" [29]. For low Z, stable nuclei are those with N = Z, since in this case the interaction between protons and neutrons is slightly stronger than the proton-proton and neutron-neutron ones. When the mass number $A = Z + N \geq 40$, the stability curve diverges from the ideal N = Z line towards the nuclei with N > Z (neutron-rich nuclei), because the electrostatic repulsion between protons leads to prevail over the other stabilizing forces. Therefore more neutrons, which do not contribute to electrostatic repulsion (indeed they are uncharged), need to stabilize the nucleus. For extremely high values of A, and consequently very big atomic radii, the strong interaction tends to lose its efficacy respect to electrostatic repulsion, thus this fact limits the stability of the so-called Super Heavy Elements (SHE). Nuclei with the same number of protons but with different number of neutrons are called isotopes: in order to distinguish between them one must indicate clearly their mass number, in the form , ${}^{A}_{Z}E$ where E is the element symbol and Z is optional since it is uniquely associated to the element.

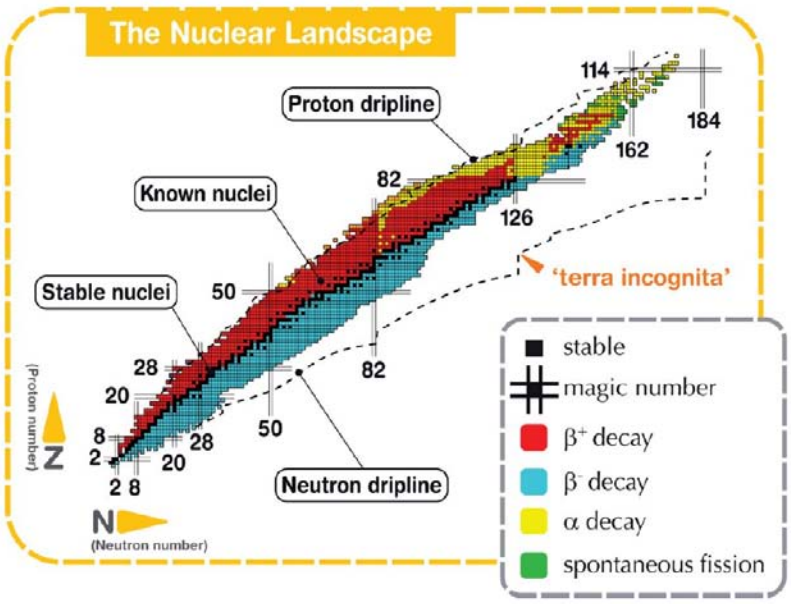

Figure 1.1: The nuclide chart.[3]

Nuclides having an unfavorable ratio between the proton and neutron number tend to spontaneously transform emitting both particles and electromagnetic radiation until they become stable: this phenomena is called radioactive decay. Nuclei with a shortage of neutrons can be defined as proton-rich, while nuclei having an excess of neutrons are called neutron-rich. They are both unstable and they decay emitting electromagnetic radiation depending on their nature, indeed 4 kind of decay exist:

- α **decay**: the α radiation characterizes radionuclides having Z>82 and A>200 and it is substantially made by Helium nuclei, composed of two protons and two neutrons. The transformation of a nuclide due to and α emission can be schematized as:

$$^{A}_{Z}X \rightarrow ^{A-4}_{Z-2}Y + ^{4}_{2}\alpha$$

  Therefore the emission of an α particle leads to decreasing both the atomic number and the mass number, thus the starting nuclide transforms into another one isotope of a different element. The emitted α particles have initially a high kinetic energy, but relatively low speed (about 1/10 of the speed of light). Due to their high mass, they have a low penetration power and they lose abruptly lose their energy when the interaction with the matter occurs.

- β^- **decay**: the β^- radiation is characterized by to electrons expelled from the nucleus when a neutron is transformed into a proton:

$$^{1}_{0}n \rightarrow {}^{0}_{-1}\beta^- + ^{1}_{1}p^+ + \overline{\nu}$$

  The $\overline{\nu}$ particle is called antineutrino, it is without charge and it is characterized by a mass value close to 0.

After the β^- emission, a nuclide will transform to another nuclide with the same mass number (*isobaric*) but with the atomic number which is increased by a unit:

$$^{A}_{Z}X \rightarrow_{Z+1}{}^{A} Y +_{-1}{}^{0} \beta^- + \overline{\nu}$$

The β^- particles have a very low mass (about 7000 times less than the α particle) so they have a higher penetration power with respect to α particles.

- β^+ **decay**: the β^+ particles characterizes only few artificial nuclides; their mass is the same of electrons, while their charge is positive, indeed they are called *positrons*. It is supposed that they are formed when a proton is transformed into a neutron forming also a neutrino ν :

  $$^{1}_{1}p^+ \rightarrow {}^{0}_{1}\beta^+ +^{1}_{0} n + \nu$$

  When the positron is emitted, the nuclide transforms into its corresponding isobar but with the atomic mass decreased by a unit:

  $$^{A}_{Z}X \rightarrow_{Z-1}{}^{A} Y +^{0}_{1} \beta^+ + \nu$$

- γ **decay**: γ rays are an electromagnetic radiation characterized by a very high frequency which sometimes follow either a α or β particle emission from radionuclides. They come from the nucleus resettlement due to a particle emission which causes the nucleus excitation, i.e. its energy state will be larger and it emitsγ rays at the same time. The nucleus is characterized by discrete energy levels and the γ rays energy is given by the difference between them, thus the γ radiation that follows can assume only certain defined values. γ rays are also identified by a penetration power so much larger than both α and β emission.

1.2 SPES project

The aim of the SPES project [16] is to provide high intensity and high-quality beams of neutron-reach nuclei to perform forefront research in nuclear structure, reaction dynamics and interdisciplinary fields like medical, biological and material sciences. It can be considered as composed of four phases:

- SPES-α: at the heart of SPES: the cyclotron and ISOL target.
  It foresees the acquisition, installation and commissioning of a high performance cyclotron with high output current ($0,7\ mA$) and high energy (up to 70 MeV), together with the related infrastructure for the accelerator and experimental stations. The cyclotron will be provided with two exit ports, a configuration well suited for the double mission of the laboratory:

basic research and technological applications. One of the two beams will be dedicated to the nuclear physics facility (producing mainly neutron-rich ions by collisions of protons onto a UC_x target); the second will be dedicated to applied physics;

- SPES-β: the acceleration of neutron-rich unstable nuclei
  Neutron-rich species will be accelerated against suitable targets. In the collisions, new, extremely neutron-rich nuclei will be produced, which are similar to those generated in advanced stellar stages and are not present on Earth due to their short lifetime. The investigation on such systems is a new frontier of physics, for extending our knowledge of nuclei at extreme conditions and for providing basic information in the study of stellar evolution;

- SPES-γ: production of radionuclides for applications.
  It concerns the production of radionuclides of medical interest by using the SPES-α cyclotron. The goal is the production of innovative radiopharmaceutical both for ISOLPHARM (explained in Section 1.3) and LARAMED (LAboratory for the production of Radioisotopes of MEDical interest) as well as the production of conventional radionuclides with new accelerator-based approaches;

- SPES-δ: multidisciplinary neutron sources.
  It foresees the development of an intense neutron source, from the cyclotron and/or from a high intensity linear accelerator based on radio-frequency quadri pole (RFQ) technology. Applications of the neutron source range from nuclear astrophysics to test of electronics in space, characterization of nuclear waste or experimental tumor treatments.

Figure 1.2: The SPES project's logo representing the four phases α, β,γ, δ [5].

The SPES facility will be mainly devoted to the production of few selected neutron-rich radioactive nuclei with mass number in the range 80-160 by the ^{238}U fission at a rate of 10^{13} fission/s. The facility's layout is shown in Figure 1.3.

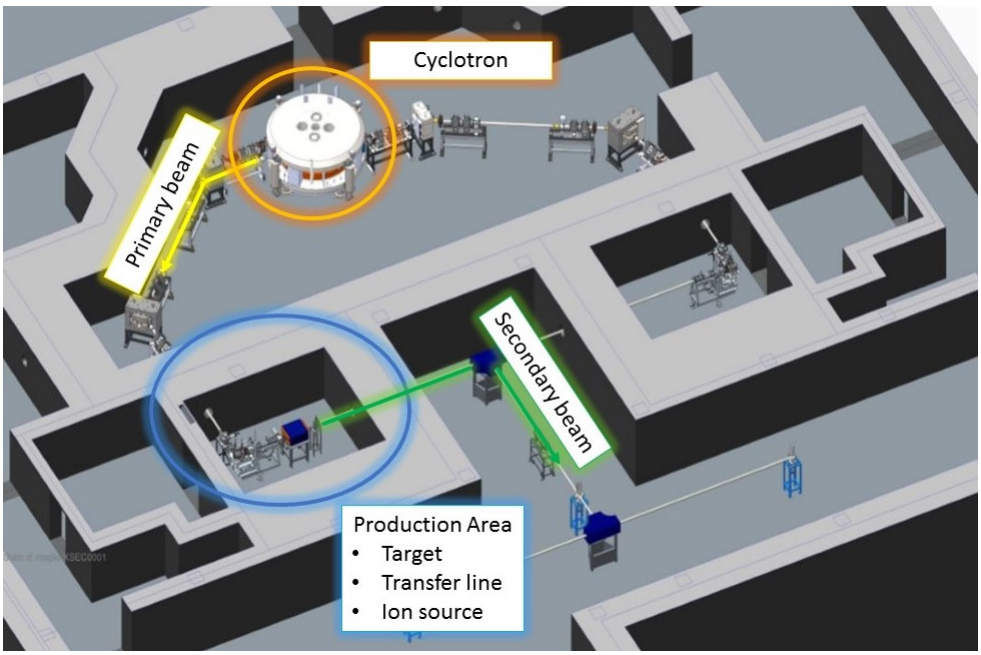

Figure 1.3: The SPES facility layout.

1.2.1 Radioactive Ion Beams (RIBs) production

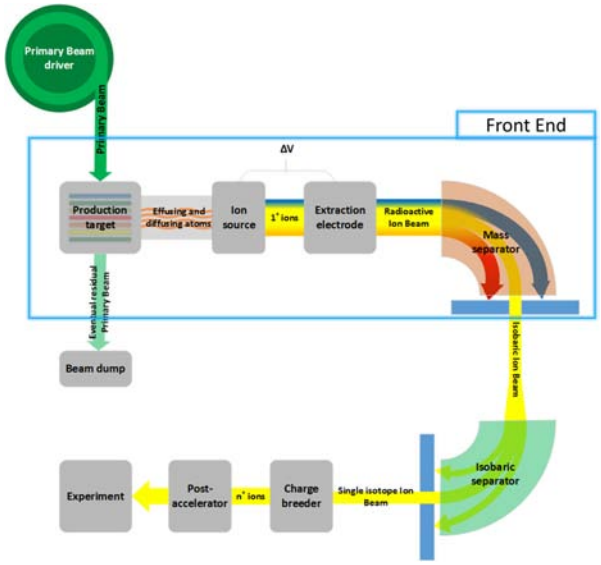

Figure 1.4: The ISOL method phases.

In order to produce RIBs, firstly the exotic species must be generated by a nuclear reaction occurring in a well confined area; finally the produced species must be transported towards a dedicated experimental area passing through identification and purification operations to obtain pure beams of a desired isotope. The production yield improves if the reaction cross section[1] is large,

[1]The cross section is the probability that a given atomic nucleus or subatomic particle will exhibit a specific reaction in relation to a particular species of incident particle. Cross section is expressed in terms of area, and its numerical value is chosen so that, if the bombarding particle hits a circular area of this size perpendicular to its path and centred at the target nucleus or particle, the given reaction occurs.

the contamination of unwanted species coming from the production target is low, the half-lives of the produced isotopes are long (generally the nuclei far from the stability valley have short half-lives which means that they decay quickly).

The technique to produce RIBs which is employed by the SPES project is the **"Isotope Separation On-Line method (ISOL)"** [39, 26] which is schematized in Figure 1.4: The Primary Proton Beam (PPB), in case of SPES, is provided by a **cyclotron** that produces a proton beam having the desired energy which hits the **target** where the nuclear reactions occur. The chosen cyclotron is the "*BEST 70p*" one, developed by *Best Cyclotron* (Figure 1.5), which provides two independent proton beams that can achieve energies up to 70 MeV and a maximum current of 750 μA.

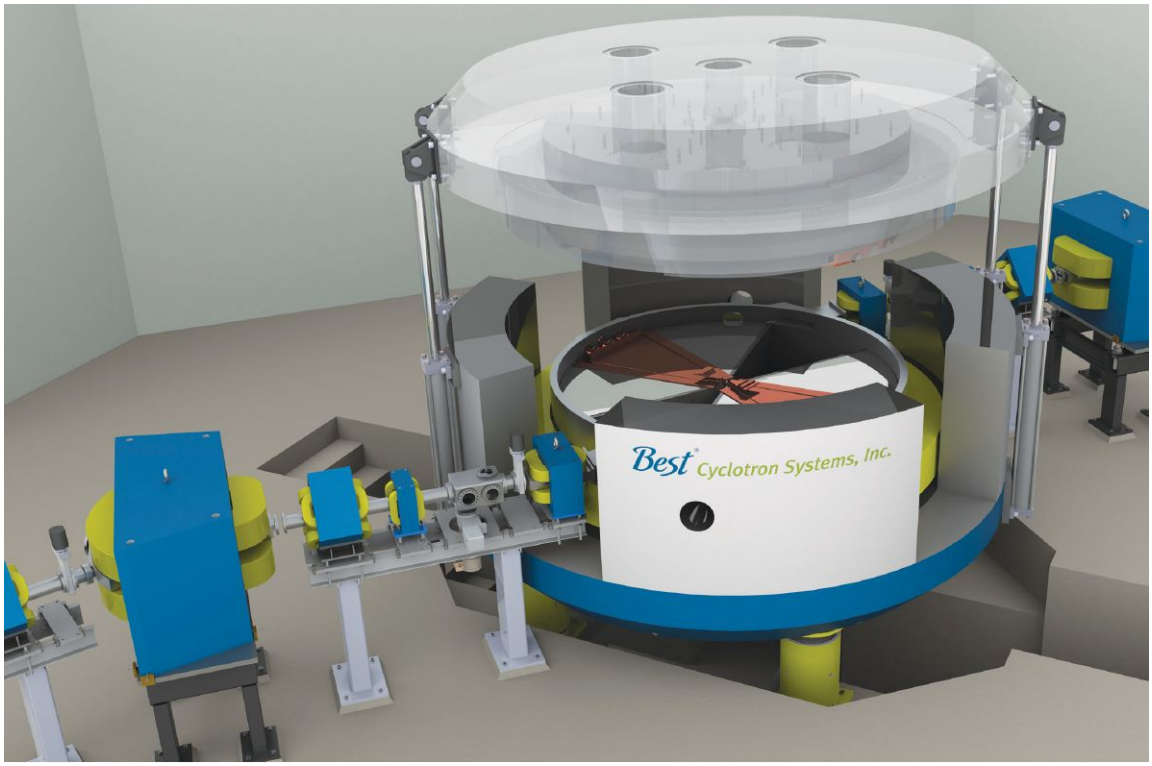

Figure 1.5: Best 70p cyclotron produced by Best cyclotron. [1]

The radioactive isotopes produced inside the SPES target diffuse through the target material and then effuse in the **transfer line** towards the **ion source** where they acquire the 1^+ charge state needed for their extraction. This can be accomplished by the Target and Ion System (TIS) [7] which is constituted by the production target and the ion source, linked together by means of a tubular transfer line maintained at high temperature to avoid loss of radioactive atoms by sticking on its walls. In order to optimize the 10kW heat dissipation, the SPES target consists of multiple thin disks housed in a cylindrical graphite box as shown in Figure 1.6(b).

The SPES TIS is closed inside a water-cooled vacuum chamber (Target Unit), capable to dissipate the amount of power associated to both the target and the ion source, and to guarantee a vacuum level of approximately 10^{-6} $mbar$ (Figure 1.6(a)). In particular the high-vacuum is needed to avoid

the species oxidation and to increase the produced radioactive species mean free path.
The disadvantage of ISOL production is the difficulty to achieve high beam purity due to the many isobars of different elements produced simultaneously form the target. For this reason choosing properly the target material and design is fundamental to optimize the primary beam interaction leading to reach the highest production cross-section with the lowest amount of contaminants and to withstand the highest possible beam currents without damaging.

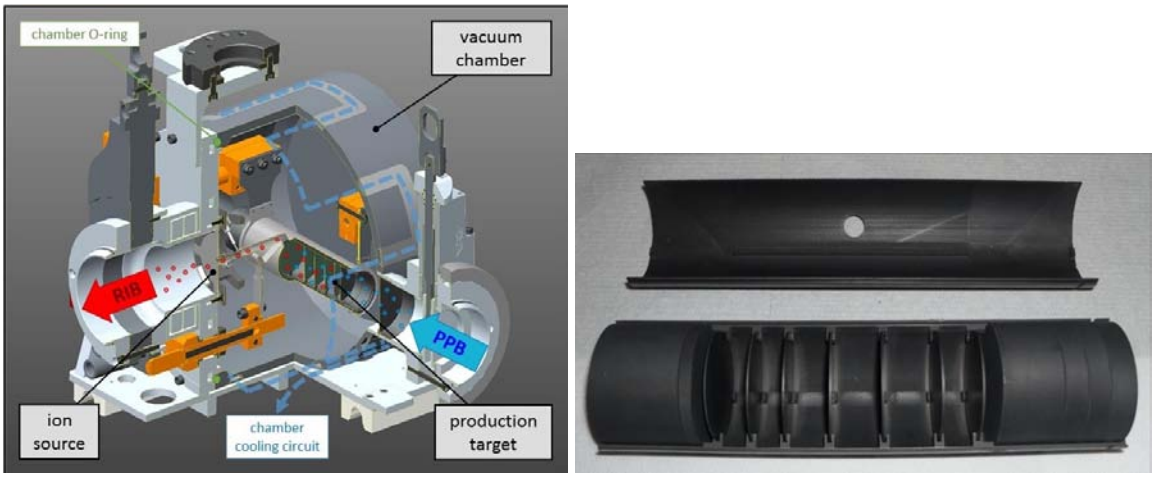

(a) Target and Ion System. (b) The Cylindrical graphite box containing the target.

Figure 1.6: Target unit.

Three kind of ion sources are employed in SPES and for each one it is possible to ionize different elements which are represented in Figure 1.8:

- The Surface Ion Source (SIS) allows the ionization through the impact of the radioactive isotopes coming from the target with the inner surface of the so-called "*hot cavity*" which is a Rhenium (or tantalum) tubular component maintained at high temperature (about 2000 °C) by Joule's effect to increase the yield of the ionization. Indeed if the minimum energy to remove an electron from a surface is larger than the isotope's ionization energy the ionization occurs. In particular this method is limited only to elements of the first and the second group;

- The Resonant Ionization Laser Ion Source (RILIS) [27], which is schematized in Figure 1.7, allows the ionization process by a laser constituted by overlapping of more beams having different wavelengths which is focused inside the source. The ionization process typical consists of two or three steps, everyone characterized by a precise energy level (or wavelength λ) for the laser photons.

  It provides to the isotopes the energy necessary to leave one electron employing the same architecture of SIS, in order to achieve the charge $^{+}1$. With this method is possible to ionize only the wanted species, thus the output beam will be pure. The only possible contamination is due to the surface ionization in contact with the hot sources walls, this happens only for

some elements like Cesium;

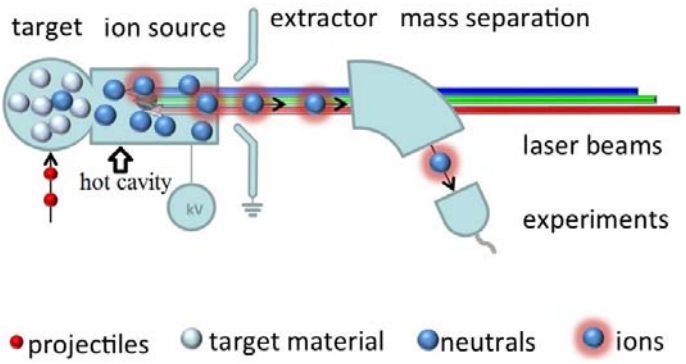

Figure 1.7: Schematic of RILIS.[2]

- The Plasma Ion Source (PIS) through the Forced Electron Beam Induced Arc Discharge (FEBIAD) technique allows the ionization: the isotopes are ionized by the impact with electrons extracted by means of the thermionic effect from a high temperature cathode and accelerated into a low pressure plasma. This technique allows the ionization of a great number of elements, including noble gases, but it is not selective.

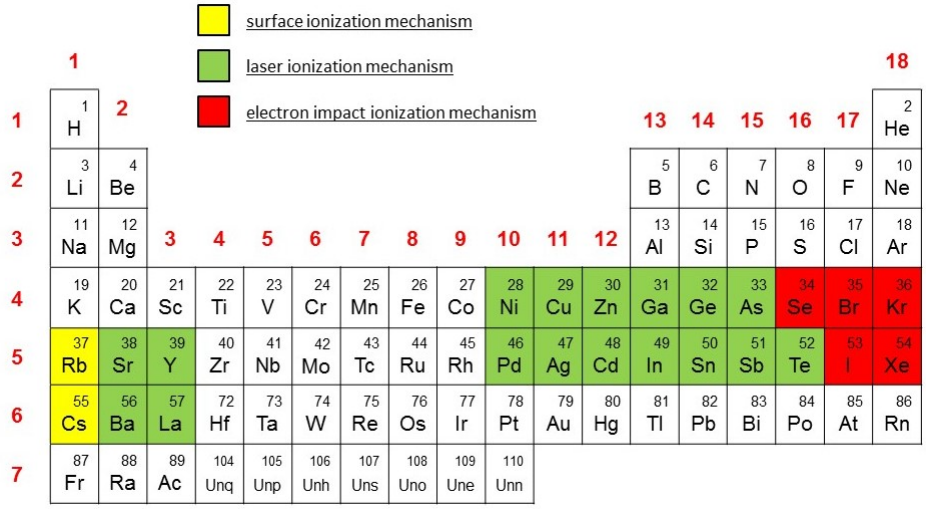

	1	2	3	4	5	6	7	8	9	10	11	12	13	14	15	16	17	18
1	1 H																	2 He
2	3 Li	4 Be											5 B	6 C	7 N	8 O	9 F	10 Ne
3	11 Na	12 Mg											13 Al	14 Si	15 P	16 S	17 Cl	18 Ar
4	19 K	20 Ca	21 Sc	22 Ti	23 V	24 Cr	25 Mn	26 Fe	27 Co	28 Ni	29 Cu	30 Zn	31 Ga	32 Ge	33 As	34 Se	35 Br	36 Kr
5	37 Rb	38 Sr	39 Y	40 Zr	41 Nb	42 Mo	43 Tc	44 Ru	45 Rh	46 Pd	47 Ag	48 Cd	49 In	50 Sn	51 Sb	52 Te	53 I	54 Xe
6	55 Cs	56 Ba	57 La	72 Hf	73 Ta	74 W	75 Re	76 Os	77 Ir	78 Pt	79 Au	80 Hg	81 Tl	82 Pb	83 Bi	84 Po	85 At	86 Rn
7	87 Fr	88 Ra	89 Ac	104 Unq	105 Unp	106 Unh	107 Uns	108 Uno	109 Une	110 Unn								

Figure 1.8: The isotopes that can be extracted with SIS, RILIS and PIS are represented in this figure.

The secondary beam extracted from the ion source is mass separated by an **analyzing magnet** and transported to the focal plan where it can be opportunely focused. An important property that express the quality of the system is the mass resolving power, defined as $R = \frac{M}{\Delta M}$, where ΔM is the FWHM (full width at half maximum) of a beam of ions with mass M in the focal plane of the separator, which has to be maximized in order to better select the desired isotope.

A **"cooler"** is used to improve the optical properties of the ion beam and to bunch it, in order to increase the peak to background ratio of certain applications like laser spectroscopy or to inject the beam into a charge-state breeder. Two kind of devices are used as coolers: "Penning traps" and

"Radio Frequency (RF) coolers". The former is based on the storage of ions using a combination of magnetic and electrical fields, the latter using electrical DC (Direct Current) and RF (Radio Frequency) fields.
In order to have a simpler and more efficient post-acceleration it is useful to produce a multiple charge state ion beam before the injection into the post-accelerator. A **charge-state breeder** transforms a singly charged ion beam into a multiple charged one. Two types of charge-state breeding ion sources are used: the Electron Beam Ion Source (EBIS) and the Electron Cyclotron Resonance (ECR) ion source. Both are based on an intense bombardment of the beam ions with energetic electrons, with electron impact ionization yielding ions in higher charge states. The plasma of ions and electrons is confined through electrical and strong magnetic fields.
Finally the highly charged ion beam from the charge-state breeder or the beam of singly charged ions is then injected into the **post-accelerator**. After the post-acceleration step the beam is sent to the experimental users.
This system provides a secondary beam production which is:

- **Efficient**: the manipulation steps (ionization, mass separation, acceleration and transport to the experimental apparatus) is designed to be efficient as well as possible to nullify nuclei losses due to decay;
- **Fast**: in order to avoid the losses caused by radioactive decay between the moment of production and the arrival at the experimental set-up;
- **Selective**: the final ion beam's purity assumes an vital role for the following applications, thus this can be achieved through the coupling between the ion source and the mass separation process;
- **Highly productive**: this is ensured delivering the highest primary beam intensity thanks to the capability of the target to dissipate the power given by the primary beam action.

1.3 ISOLPHARM

The ISOLPHARM project [18] is aimed to produce pure radionuclides for radiopharmaceuticals employed in nuclear medicine through the RIBs produced at SPES; The possibility to produce radiopharmaceuticals through the ISOL technique is due to its intrinsic ability to deliver extremely pure and selective RIBs. Following the ISOL scheme, after the creation of the desired ion beam, the radioisotopes must be collected in a way depending on the state of matter of the element and they have to be made available for the radiopharmaceutical production; concerning the elements present at the solid state such as Sr, the output beam can be implanted into a solid substrate designed both to have an appropriate mechanical resistance to support the vacuum conditions

inside the front-end (schematized in Figure 1.4) and to be comfortable to realize a sure and effective radiopharmaceutical.

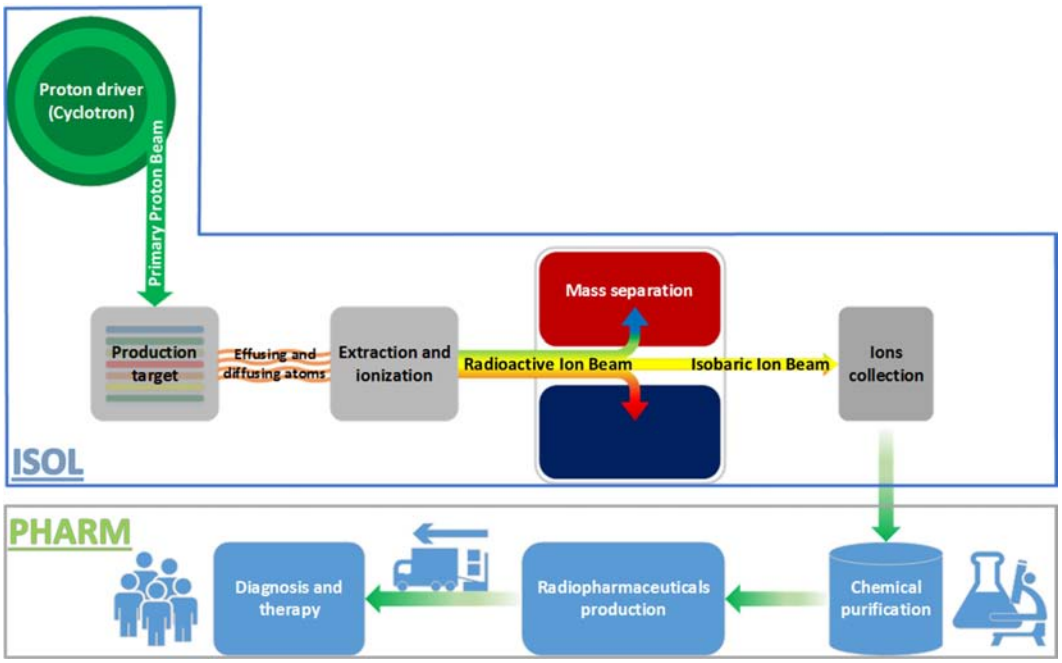

Figure 1.9: ISOLPHARM project phases.

Radiopharmaceuticals are medicines that deliver a predefined amount of radiation to a target tissue for diagnostic or therapeutic procedures depending on the mechanism of decay [63]. In particular they attract a great interest because of their capability to be selectively withheld in specific tissues leading both to focused therapies and better diagnostic techniques. High penetrating radiation, such as γ emission, is mainly used for early diagnosis of tumors and inflammatory diseases, while α and β^- emission, which induce the cell death, are used for anticancer therapy and pathological conditions such as rheumatoid arthritis. Thus the radionuclides have to deliver a cytotoxic level[2] of radiation onto a disease site in order to heal the patient; to reach the target tissue, radionuclides can be administered alone or they can be bonded with organic molecules which allow their transport towards the target cells.

Radiopharmaceuticals are characterized by a "radioactive core" and a "carrier system" that allows the deposition of radiation onto the malignant cell population thus avoiding damage to healthy tissues. When a radioisotope of an element in pure form, without isotopic contaminants, it is defined as "carrier-free" and is characterized by a huge specific activity $[GBq/mg]$ which is the ratio between the radioactivity of the radioisotope and the mass of the element taken into account. Due to such a high specific activity, carrier-free radionuclides allow to achieve a high binding affinities to the receptors, thus leading to the optimization of the radionuclide action when the number of available target cells is low.

[2]Cytotoxicity is the quality of being toxic to cells.

After the target's bombardment explained in Section 1.2, a large number of isotopes are emitted and the chemical methods to extract the desired radionuclide are not able to purify it from isotopic contaminants producing carrier-added radionuclides with a low specific activity. To avoid carrier-added radionuclides production is possible to design a process composed of the mass separation followed by the chemical purification[3]: the former step allows the removal of isotopic impurities, the latter of isobaric contaminants. This is the strong advantage of using ISOL for the production of radionuclides as radiopharmaceutical precursors (ISOLPHARM): the intrinsic presence of mass separation creates isobaric beams which can be collected on substrates, following by chemical separation of elements with techniques already established.
For instance nowadays ^{89}Sr is produced by neutron irradiation and so it is carrier added, with low specific activities values; for this reason it is employed only in the chloride form (Metastron) as bone seeking agents for the palliation of bone metastases . Carrier-free ^{89}Sr produced with the ISOL method at ISOLPHARM can be regarded as a new and innovative nuclide for molecule labeling and active targeting.

1.3.1 Clinical interesting radioisotopes

The main characteristics that a radiopharmaceutical must satisfy are [63]:

- Decay properties: depending on the isotope decay it can be used as a diagnostic or therapy agent, indeed if the radiation has a high penetration power it can pass through the patient body and it can be detected by the instruments .i.e. diagnostic or imaging use (for instance for Positron Emission Therapy - PET and Single-photon emission computed tomography - SPECT). On the contrary, the short range radiations are employed for therapy treatments in order to deliver as much as possible energy inside a definite region (Targeted Alpha Therapy - TAT);

- Half-life ($\tau_{1/2}$ $[s]$): it is the time required for one-half of the atomic nuclei of a radioactive sample to decay; the radioisotope must be stable enough to be administered to a patient and to catch the target, consequently a minimum half-life is needed. Nevertheless the half-life must not be so much high in order to avoid an excessive exposure to radiation of the patient;

- Chemical properties: in order to achieve the proper affinity with the sick tissue is necessary to adjust the chemical properties for example bonding at the radioisotope the right capping agent;

- Productivity:a radiopharmaceuticals must be as easy to produce as possible to satisfy the market demand, thus this can be achieved employing innovative production technologies

[3]The chemical purification depends on the element to purify.

such as the ISOL method.

Looking at the Figure 1.10 it is possible to identify some interesting radioisotopes which can be produced by the SPES facility:

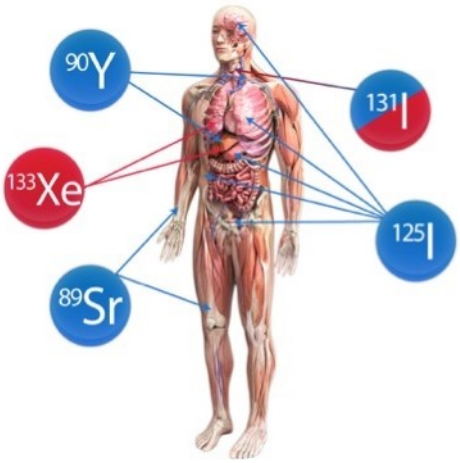

Figure 1.10: The radioisotopes for clinical interest provided by SPES. The blue ones are nuclides employed in therapy, while the red ones are useful for diagnostic.[63]

- ^{90}Y is employed both in the targeted therapy and to heal some forms of arthritis, thus its therapeutic action is due to β^- decay;
- ^{89}Sr is a radioisotope helpful in the palliation of painful bony metastases, as it allows for targeted radiation to metastatic lesions, inducing apoptosis of cells, membrane and protein damage. ^{89}Sr chemical characteristics are the same of ^{90}Sr, the difference concerns the half-life which is about 50 days for the former and almost 29 years for the latter, that is consequently more toxic;
- ^{125}I is a proton-rich radioisotope which emits γ radiation avoiding the cancer proliferation.
- ^{131}I is a neutron-rich radionuclide which emits both β^- and γ radiation and it is characterized by a half-life of about 8 days. It is employed to heal either the hyperthyroidism or thyroid cancer.
- ^{133}Xe is another neutron-rich radioisotope and it emits both β^- and γ radiation. It is actually used in diagnostic due to its properties suitable for SPECT;
- ^{75}Se is a proton-rich nuclide γ emitter produced in a really selective way through SPES, because the other nuclides having mass number 75 present inside the outside beam have a very short half life.

1.3.2 Medical applications

This paragraph explains briefly the most common nuclear medical procedures in practice today, indeed the use of radioisotopes and nuclear techniques have transformed both diagnostic and therapeutic medical procedures.[31]
Through a multi-disciplinary research which involves nuclear physics, engineering, radiochemistry and biology, it has been possible to improve the nuclear medicine techniques aimed to study physiological processes and non-invasive diagnose and treat diseases.

Nuclear imaging

Modern nuclear medical imaging techniques take advantage of the emission of unique decay products from specific nuclei in order to obtain 3D images of tissues thanks to the placement of radioactive species within the tissue. Nuclear imaging provides information regarding the functioning of both normal and diseased tissue.
The two main nuclear imaging techniques which are used are the Positron Emission Tomography (PET) and Single-Photon Emission Computed Tomography (SPECT), the difference between these two practices is the kind of radioactive decay properties of nuclei.
PET scanning employs a nuclear tracer that decays by positron emission: the patient is injected with a solution containing the radioisotope of interest. The emitted positrons annihilate with electrons within the tissue under investigation producing photons, which will be detected by scanners surrounding the patient and are used to reconstruct in detail the structure of the tissue under investigation (See Figure 1.11).

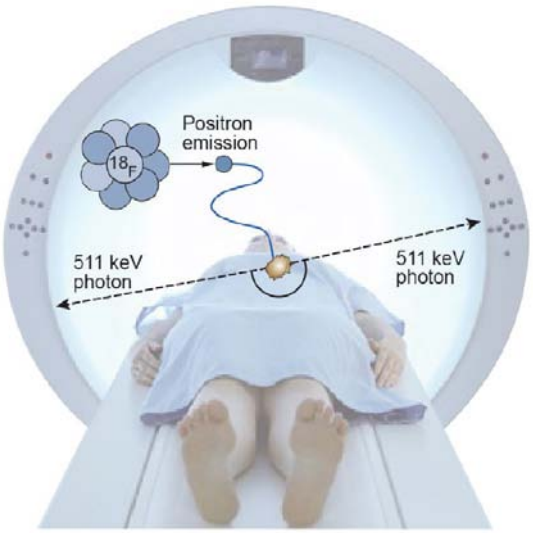

Figure 1.11: Schematic picture of the PET scanning technique.[31]

PET is commonly employed in oncology to diagnose and to reclassify a tumor after an initial treatment. It is also used to detect residual cancer and to monitor changes in tumor volume.

The principle of operation of SPECT is similar to PET, in fact SPECT uses a radiopharmaceutical labeled with a γ-emitting nucleus. It is delivered to the tissue of interest, normally by injection into the blood stream, then the γ rays passing through the patient body will reach the detector which provides the 3D image. The SPECT is widely used to analyze the blood flow and its correlation with diseases in major organs.

Targeted radionuclide therapy

The radionuclide is attached to a molecular carrier, which is opportunely chosen to attack the cancer cells. The radionuclides used in targeted therapy emit short-range charged particles, such as beta electrons, Auger electrons or alpha particles. The three common radionuclides in current use are ^{90}Y, ^{131}I and ^{89}Sr, while other species are under investigation.

This technique permits to destroy the diseased cells delivering a toxic level of radiation to a diseased site by attaching the radionuclide to a molecular carrier that binds to the site or tumor as shown in Figure 1.12.

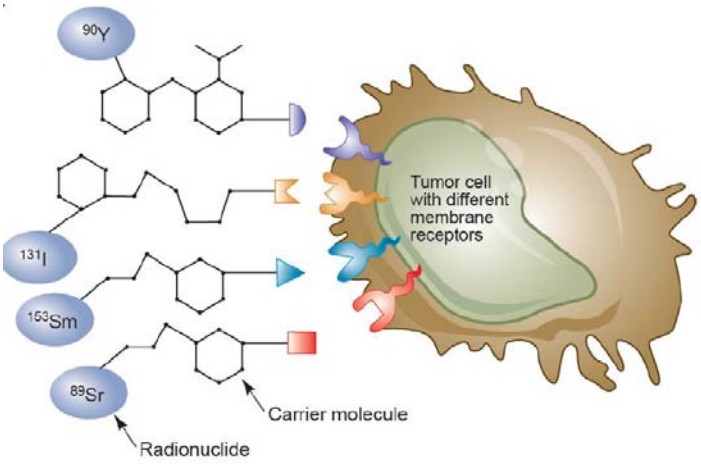

Figure 1.12: The targeted radionuclide therapy: the radionuclide, attached to a molecular carrier, attacks the cancer cell.[31]

1.4 Other applications of Radioactive Ion Beams research

The aforementioned exotic beams find applications in different branches of science such as medicine (Section 1.3), nuclear physics, astrophysics and solid state physics which will be briefly described in the following paragraph.[40]

1.4.1 Nuclear physics

Nowadays the knowledge of the atomic nucleus structure is based on the properties of nuclei placed close to the "valley of stability" or in the proton-rich side of the nuclide chart. Models extracted from them can not be used to describe atom far from the stability region because it leads

to wrong suppositions and expectations. The models based on them to describe the regions far from stability are very puzzling and lead inevitably to wrong assumptions and expectations. Thus it is important to revisit and eventually modify some basic concepts to have a better understanding of nuclear physics field.

(i) **Standard model improvement and verification**

Nuclear physics is actually based on the standard model which takes into account three of the four fundamental interaction, i.e. the strong nuclear interaction, electromagnetism and the weak nuclear interaction. This model describes the function and the properties of all the matter's particles, but it was built through some assumptions that are not yet verified, indeed leaves some phenomena unexplained: it does not fully explain baryon asymmetry, incorporate the full theory of gravitation as described by general relativity, or account for the accelerating expansion of the Universe as possibly described by dark energy. The model does not contain any viable dark matter particle that possesses all of the required properties deduced from observational cosmology. It also does not incorporate neutrino oscillations and their non-zero masses.

Thanks to RIBs produced by facilities like SPES, it is possible to measure precisely the decay properties of some isotopes in order to verify and to confirm the aforementioned assumptions;

(ii) **Studies concerning complex nuclei structure**

The subatomic particles, denoted as *quarks*, compose protons and neutrons (nucleons), but their physics interaction overlaps the nucleons in which they are confined. It was observed that the interaction occurs in a different way between free nucleons and nucleons appertaining at the same atom, indeed it is influenced by the neutron and proton density characteristic of the nucleus. Actually a general equation that rules the nuclear interactions does not exist for all atoms, in fact quantum-mechanic calculations can be done only for light nuclei.

Therefore in order to clarify and quantify the intensities of these particular interaction between exotic nuclear particles placed far from the valley of stability of the nuclide chart, it may be helpful employing pure RIBs produced by the SPES facility studied by dedicated apparatus;

(iii) **Nucleus radius measurement: halo nuclei**

The nucleus size depends on the total number of nucleons forming it through the following simply relation:

$$R = R_0 \cdot A^{\frac{1}{3}} \tag{1.4.1}$$

- R is the nuclear radius;
- $R_0 = 1,2\ fermi$[4] is a constant;

[4] $1\ fermi = 10^{-15}\ m$

- A is the mass number.

However in particular conditions far from the valley of stability, the Equation (1.4.1) does not work so well; in fact in that region the interactions occurring between nucleons become extremely weak leading to form *halo nuclei* instead of the nucleus as an aggregate. The halo nuclei are characterized by a different neutrons collocation, indeed they are weakly bonded with the nucleus thus they orbit around it (valence neutrons).[6]
For example the halo nucleus ^{11}Li has an average nucleus size similar to ^{48}Ca, but the two valence neutrons orbit extend its dimension until to achieve about the same size of ^{208}Pb which is much more massive as show in Figure 1.13.
Actually is possible to determine the distribution of the protons thanks to atomic spectroscopy apparatus, employing radioactive beams at low energy and lasers. High energy beams such as the SPES facility ones can be used to discover the overall nucleons distribution;

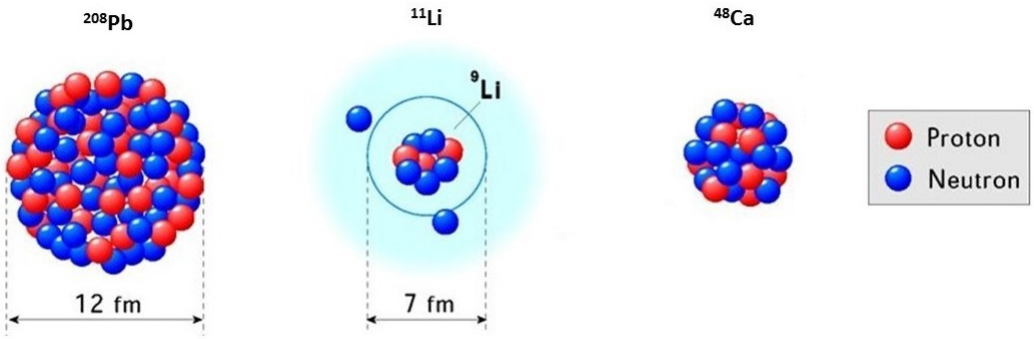

Figure 1.13: Nucleus sizes comparison between ^{11}Li and other more massive nuclei.

(iv) **Superheavy elements production**

Natural elements are about 90: from Hydrogen to Uranium. Thanks to nuclear fission during last years it was possible to synthesize high mass number elements extending the periodic table until the element 118. These elements, known as *superheavy*, form around the *island of stability*, indeed a configuration composed of 114 protons and 184 neutrons seems to stabilize the nucleus. Coupling together the RIBs neutron rich produced with the new technologies and a target neutron rich as well, it is possible to generate the suitable conditions to study more accurately the superheavy elements

1.4.2 Nuclear astrophysics

Nuclear astrophysics aims to understand the universe structure and composition. Nowadays, the main challenges of experimental nuclear astrophysics are related to the stellar cycles description

and characterization. The energy production inside stars is allowed by nuclear reactions between both stable and unstable nuclei: these processes can either be stable for billions of years or be explosive involving a timescale of seconds. For example one of the most important burning cycle involving unstable nuclei is the so-called Carbon-Nitrogen-Oxygen (CNO) cycle , that is composed of a set of fusion reactions by which stars convert hydrogen to helium.
To represent as well as possible these processes by a model, it is necessary to collect experimental information concerning the developed exotic nuclei which may be produced inside the RIBs and they can be studied by dedicated instruments.

1.4.3 Solid state physics

(i) **Radio Tracer Diffusion (RTD)**

The RTD is a technique born in 1920 that consists in implanting inside a solid system some radioactive nuclei in order to study their decay detecting the emitted particles or radiation. This system can detect signals even if are present very few atoms, indeed it represents one of the common way to study atomic diffusion processes.
The solid system can be doped with "probe" radioisotopes by diffusion, through nuclear reaction or ionic implanting. The RTD method provides information concerning:

- The interaction between the probe atom and the crystal lattice that round it;
- The electromagnetic field inside the crystal;
- The diffusion process and the interactions between the probe atoms;
- The crystal lattice defects.

(ii) **Doped semiconductor**

The development of small sized semiconductors having optimal both electric and optical properties requests an overall control of defects (intrinsic or extrinsic) which influence the aforementioned properties. The radioactive isotopes influence the optical and electrical behavior of the semiconductor, such as stable isotopes, depending on their chemical properties and the positioning inside the crystal lattice: in particular small sized semiconductors properties may be considerably changed by a defect presents in a concentration less than $10^{12}\ atoms/cm^2$; therefore to control as well as possible the semiconductor performances, experimental techniques that couple a large chemical sensitivity with a high defects concentration detection sensitivity.

Radioactive ion beams can be used as a powerful diagnostic tool to provide detailed information on the environment in which they are implanted. An important application is represented by the Emission Channeling technique, used to study the structure and properties of impurity-defect complexes in solids, particularly in semiconductors whose functioning is

deeply influenced by defects. The technique is schematized in Figure 1.14 and it relies on the emission and movement of charged particles through a single crystal subsequent to the decay of the radioactive ions previously implanted into the crystal. The particles are revealed by 2-dimensional position sensitive detectors. The working principle of this analytical method is based on the angle dependence of the intensity of the emitted radiation as a function of the orientation of the host crystal (different crystal axes and planes): from the measured anisotropic intensity distributions the position occupied by the radioactive ions inside the lattice structure of the implanted solid can be determined with a great accuracy.

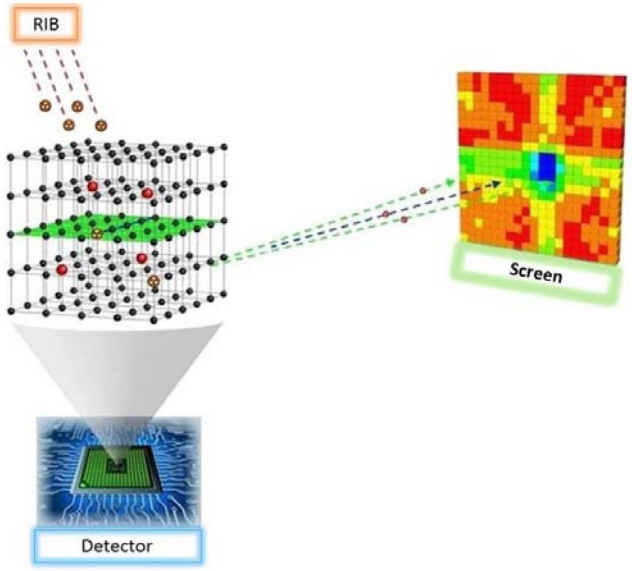

Figure 1.14: Schematic of the emission channeling technique.

CHAPTER 2

The ideal SPES target

The target is the core of an ISOL facility because its atoms interact with the primary beam providing the desired radioactive species.. The key points to efficiently produce and give RIBs to experimental users are the target material and design, thus the production method, the characterization and a more specific analysis of all mechanisms in which the target is involved, assume a fundamental role for the whole project.
In this chapter a general overview concerning the isotopes production and release from the target will be given; the diffusion and effusion mechanisms and the material selection and design criteria adopted for the SPES target will also be described.

2.1 Isotopes production and release in an ISOL target

The two RIB generation phases, production and release, that involve the target will be discussed in detail in the following paragraphs.

2.1.1 Production

Nuclear reaction caused by the interaction between the primary beam interaction with the target atoms provide a particular set of isotopes; it is clear that the amount of the produced species depends on some basic features of both the beam and the target nuclei.
To determine the intensity $I_{production}\ [A]$ of the reaction products generated in the target, the following Equation (2.1.1) can be used [26]:

$$I_{production} = \phi\, \sigma\, N_{target} \tag{2.1.1}$$

- $\phi\ [A]$ is the primary beam intensity;
- $\sigma\ [cm^2]$ is the cross section aforementioned in Section 1.2;
- $N_{target}\ \left[atoms/cm^2\right]$ is the number of target atoms per unit area.

Considering N_{target}, it can be calculated as:

$$N_{target} = \frac{N_A \, l \, \rho}{PM} \tag{2.1.2}$$

- $N_A = 6,022 \cdot 10^{23} \; atoms/mol$ is the Avogadro number;
- $l \; [cm]$ is the target thickness;
- $\rho \; [g/cm^3]$ is the target density;
- $PM \; [g/mol]$ is the target's material molecular weight.

The main nuclear reactions occurring during the interaction between the primary beam and the target are:

- **Fission**: the interaction between the incident primary beam particle (neutrons, electrons or heavy ions) and the heavy target nucleus (fissionable nucleus), forms a compound nucleus that is excited to such a high energy level that the nucleus splits into two large fission fragments as shown in Figure 2.1. A huge energy is released in the form of radiation and kinetic energy of the fragments. Moreover, the fission process may produce 2, 3 or more free neutrons which can cause further fission leading to a chain reaction;

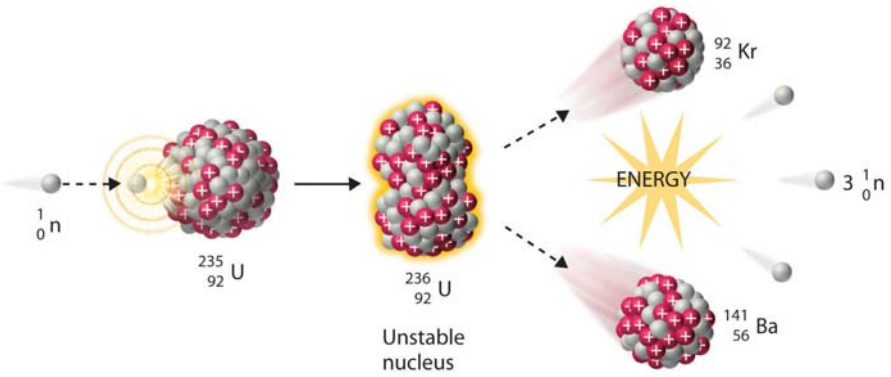

Figure 2.1: The incoming neutron, interacting with ^{238}U nucleus, causes a fission reaction which leads to split the starting atom into smaller parts (lighter nuclei). [4]

- **Spallation**: This nuclear reaction is a process in which a light particle (proton, neutron, or light nucleus) interacts with a heavy nucleus and causes the emission of a large number of protons, neutrons and α particles that are ablated from the target nucleus, resulting in the formation of a new nucleus with similar mass with respect to the original one.
  Spallation has two stages: intra-nuclear cascade and deexcitation: the former one occurs when the interacting particle shares its kinetic energy with target nucleons by elastic collisions and a cascade of nucleon-nucleon collisions proceeds. Then the latter one takes place and the energy is equally distributed throughout the nucleus which is in a highly excited state; finally the nucleus loses its energy by evaporation of neutrons or light charged fragments;

- **Fragmentation**: Both projectile fragmentation and target fragmentation are used for an ISOL system. The former occurs when a high-energy heavy-ion beam (projectile) bombards the target causing the abrasion-ablation process which is shown in Figure 2.2. The abrasion process is described as the geometrical picture of fireball model, then a spectator piece of projectile (prefragment) leaves. Through the ablation process the prefragment emits light particles and γ rays to become a *fragment* observed in experiments.[48]
  The latter is similar to the previous one, the difference is that the target interacts with a high energy proton beam.
  These reactions produce again a wide variety of isotopes, close to the initial target or projectile nucleus as well as very light nuclei.

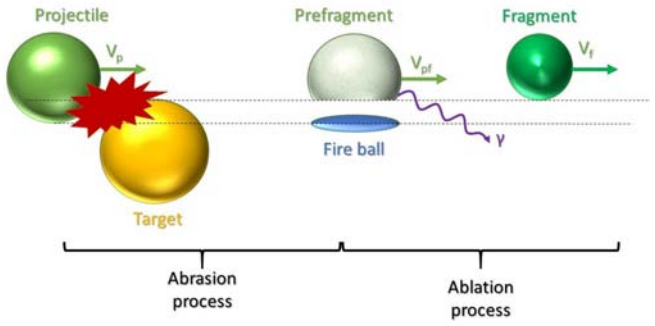

Figure 2.2: Schematic view of the projectile fragmentation.

- **Light- and heavy-ion Fusion Evaporation Reactions or Direct Reactions**: with light-ion induced fusion reactions nuclei, close to the line of stability on the proton-rich side are produced. Heavy-ion fusion evaporation reactions have typically a much lower cross section than the light-ion ones but produce neutron-deficient nuclei very far from the line of stability. Usually this kind of reactions doesn't involve any fissile material, and so the number of produced isotopes for each kind of target material is very limited with respect to the three aforementioned reactions.

2.1.2 Release

After the production of radioactive isotopes, the emitted species move through the target by diffusion with a rate depending on both temperature and material microstructure. Moreover the unstable nuclides decay each one with the proper half life $\tau_{1/2}$.
Once some radioisotopes get to the surface, they move by effusion process inside the surrounding volume colliding with each other, the target and the container, until they reach the ion source. The collisions (especially with the target and the container) are characterized by a *sticking time* which is the elapsed time between the nuclide adsorption on the hit surface and its desorption [9];

furthermore there are other mechanisms that involve the emitted species as the chemical reaction with surfaces atoms and the re-diffusion inside the target which is less probable if the target's surface temperature is maintained high.
All the process occurring from the isotopes generation to their effective use are characterized by a certain loss of efficiency, thus target release optimization, as well as an accurate design of the target-ion source geometry are necessary to avoid the loss of a big fraction of isotopes which decay before reaching the experimental areas.
The secondary beam intensity $I\ [A]$ depends on the produced radioactive isotopes intensity I_{prod} and the efficiency of every single step of isotopes production and manipulation ϵ:

$$I = I_{production}\,\epsilon = \phi\,\sigma\,N_{target}\,\epsilon = \phi\,\sigma\,\left(\frac{N_A\,l\,\rho}{PM}\right)\,\epsilon \tag{2.1.3}$$

In particular ϵ can be expressed as:

$$\epsilon = \epsilon_{d+e}\,\epsilon_i\,\epsilon_t \tag{2.1.4}$$

- ϵ_{d+e} is the release efficiency.
- ϵ_i is the ionization efficiency;
- ϵ_t is the transport efficiency;

The release efficiency depends on diffusion and effusion mechanisms which characterize the produced nuclides movement towards the ion source; they represent the slowest among all the steps, thus they can be defined as the rate determining step of the whole ISOL process. The Equation (2.1.5) determines the release efficiency in function of time t:

$$\epsilon_{d+e} = \int_0^\infty p(t)\,e^{\lambda t}\mathrm{d}t \tag{2.1.5}$$

- $p(t)$ is the delay function which represents the release probability of an atom generated at $t = 0$ under defined production conditions;
- $e^{-\lambda t}$ defines the released atoms decay.

More precisely the decay constant $\lambda\ [s^{-1}]$ is a characteristic of each specific isotope and it depends on the half-life $\tau_{1/2}$:

$$\tau_{1/2} = \frac{ln\,2}{\lambda} \tag{2.1.6}$$

Decay depends exponentially on time, indeed the number of nuclides $N(t)\ [atoms]$ present at the time t is:

$$N(t) = N_0\,e^{-\lambda t} \tag{2.1.7}$$

- $N_0\ [atoms]$ is the isotopes number at $t = 0$.

Observing the Equation (2.1.5) is easy to note that the release yield increases when the half-life increases as well; this is reasonable because the nuclide will have more available time to leave the target box without decay.
Once defined the decay function as $e^{-\lambda t}$, is possible to calculate the delay function $p(t)$ following the next steps.[65, 36, 53]
The production rate of a specific isotope $\mathrm{d}N(t)/\mathrm{d}t$ inside the target is defined by Equation (2.1.8):

$$\frac{\mathrm{d}N(t)}{\mathrm{d}t} = J(t)\ P - F(t) - \lambda\ N(t) + \sum_n \lambda_n\ N_n \tag{2.1.8}$$

- $J(t)\ [atoms/s]$ is the flow of primary particles hitting the target;
- P is the probability of yielding the particular isotope considered per incident proton;
- $F(t)\ [atoms/s]$ is the atoms release flux;
- $\lambda\ N(t)\ [atoms/s]$ is the negative isotope decay contribute;
- $\sum_n \lambda_n\ N_n\ [atoms/s]$ is the positive decay contribute due to the sum of different atoms (*parent nuclides*) that decay to the isotope of interest (*daughter nuclides*).

Release efficiency ϵ_{d+e} can be obtained as ratio between the total number of isotopes released from the target and the number of produced isotopes inside the target N_0:

$$\epsilon_{d+e} = \frac{\int_0^\infty F(t)\mathrm{d}t}{N_0} \tag{2.1.9}$$

Coupling the Equations (2.1.5) and (2.1.9) the relay function $p(t)$ can be obtained:

$$p(t) = \frac{F(t)}{N_0\ e^{-\lambda t}} \tag{2.1.10}$$

Considering that the release flux $F(t)$ will follow closely the number of isotopes inside the target $N(t)$:

$$F(t) = g(t)\ N(t) \tag{2.1.11}$$

- $g(t)$ is a function that characterize the deviation of the function $F(t)$ away from $N(t)$, and it is constant in steady state conditions.

Substituting Equation (2.1.11) into (2.1.8), assuming that the target is hit by a very short pulse of primary particles, and imposing the boundary condition $N(0) = N_0$, the number of isotopes inside the target $N(t)$ is:

$$N(t) = e^{-\left(\lambda t + \int_0^t g(\tau)\mathrm{d}\tau\right)} \left(N_0 + \lambda_n \int_0^t N_n\, e^{\lambda t + \int_0^t g(\tau)} \mathrm{d}\tau\right) \tag{2.1.12}$$

By combining (2.1.8), (2.1.11) and (2.1.12), the delay function becomes:

$$p(t) = g(t)\, e^{-\int_0^t g(\tau)\mathrm{d}\tau} \left(1 + \frac{\lambda_n}{N_0} \int_0^t N_n\, e^{\lambda t + \int_0^t g(\tau)} \mathrm{d}\tau\right) \tag{2.1.13}$$

Equation (2.1.13) can be simplified assuming $\lambda_n = 0$, which means that the radioactive decay properties of the isotopes moving through the target towards the ion source is not directly related to their release function, thus they don't affect their release times. Then considering the steady-state conditions, i.e. $g(t) = constant$:

$$p(t) = g\, e^{-gt} \tag{2.1.14}$$

Therefore under these simplifications, $p(t)$ depends only on the diffusion and effusion processes having both their delay functions $p_D(t)$ and $p_E(t)$ respectively. Supposing that effusion occurs always after diffusion, which means that re-diffusion does not happen, $p(t)$ can be expressed as:

$$p(t) = \int_0^t p_D(\tau)\; p_E(t-\tau)\mathrm{d}\tau \tag{2.1.15}$$

In Equation (2.1.15) is supposed that the radioactive nuclide diffuses inside the target material in a time interval $[0, \tau]$ and effuse inside the surrounding volume between τ and t.

2.2 Diffusion and effusion mechanisms

The previous section defines the delay function as one of the key points to increase the target release efficiency, more in detail it depends only on diffusion and effusion mechanisms after some reasonable assumptions. Next paragraphs describe the factors that affects both diffusion and effusion in order to design properly the target geometry and its material.

2.2.1 Diffusion mechanism

The movement of a chemical species from a region to another due to concentration gradient is known as diffusion. The solid state diffusion is controlled by Fick's laws: the Fick's first low, which is given by Equation (2.2.1), considers the particle flow in steady-state conditions[1], thus the movement of species occurs from a region of high concentration to region of low concentration

$$\bar{J} = -D\nabla c \tag{2.2.1}$$

- $\bar{J}$ $[mol/m^2 s]$ is the particle flux;
- ∇c $[mol/m^2]$ is the concentration gradient;

[1] Steady-state conditions in this case means that the concentration gradient does not change in time.

- $D\ [m^2/s]$ is the diffusion coefficient (or diffusivity) which can be expressed by an Arrhenius-like expression:

$$D = D_0\, e^{-\frac{E_D}{k_b\, T}} \tag{2.2.2}$$

  In which $E_D\ [J]$ is the activation energy for the particle diffusion inside a matrix, ${k_b}^2$ is the Boltzmann constant and $T\ [K]$ is the system temperature.

The Fick's first law is not sufficient to describe phenomena in which the concentration depends on both space and time, such in the case of an ISOL target. Thanks to the Fick's second law shown in Equation (2.2.3) it is possible to determine the concentration variation in time $\mathrm{d}c/\mathrm{d}t$:

$$\frac{\mathrm{d}c}{\mathrm{d}t} = D\nabla^2 c \tag{2.2.3}$$

The Fick's second law is a partial differential equation of the second order with respect to space and of the first order with respect to concentration. It can be solved defining properly the boundary conditions of the ISOL target

The SPES targets are generally realized by powder sintering leading to a porous structure; thus the diffusion process occurs in both the bulk solid grains and in the pores. The diffusivity of a solid is much lower than the one of a gas, so the solid state diffusion can be considered the slowest mechanism. Moreover, in order to have a better particle migration, the porous phase must be optimized.

Ceramic materials are usually considered to be made of spherical grains, furthermore considering them of the same size, the delay function related to diffusion process can be calculated [21]:

$$p_D(t) = \frac{6\mu}{\pi^2} \sum_{n=1}^{\infty} e^{-n^2\mu t} \tag{2.2.4}$$

$\mu\ [m^{-1}]$, which is known as diffusion parameter, is expressed by:

$$\mu = \pi^2 \frac{D}{r^2} \tag{2.2.5}$$

Where $r\ [m]$ is the spherical grain radius.

The Equation (2.2.4) proves that when the grain size decreases, the diffusion increases. Indeed the number of grain boundaries[3] increases, thus the species diffuse easily.

Integrating from time t to infinite Equation (2.1.5) it is possible to determine the diffusion contribution to the release efficiency:

$$\epsilon_D(\lambda) = \frac{6\mu}{\pi^2} \sum_{n=1}^{\infty} \frac{e^{-\left(\lambda + n^2\mu\right)}}{\lambda + n^2\mu} \tag{2.2.6}$$

In real cases, the assumption of spherical grains with the same grain size is not valid. Nevertheless ϵ_D can be determined experimentally to obtain a mean value μ for a specific target kept at a certain temperature.

[2] $k_b = 1,38 \cdot 10^{-23}\ J/K$.

[3] Grain boundaries are regions in which the atom density is lower than the grain core, therefore the diffusivity is larger at the grain boundary respect to the bulk material.

2.2.2 Effusion mechanism

Once the radioisotopes reach the target external surface, they move by effusion inside the vacuum chamber in a molecular flow regime: it means that the particles travel without a pressure gradient, thus atoms don't tend to move with a privileged direction of motion. This fact implies that the probability of a particle-particle collision is much lower than the one of a particle-wall collision. Such a condition can be modeled as the evacuation of a gas volume through an orifice.[43]
Therefore is possible to establish the parameters that control the effusion process [19]:

- The average number of collision ω with the target material surface and container walls;
- The average sticking time per collision τ_s, which depends on the temperature and adsorption enthalpy of the system particle-surface;
- The average flight time between collisions τ_f, which depends on the mass, temperature and target geometry.

The effusion delay function is expressed as [36]:

$$p_E(t) = \nu\, e^{-\nu t} \tag{2.2.7}$$

In which ν $[s^-1]$ is the time constant of the effusion process and it depends on the average effusion time τ_E $[s]$ that can be calculated as:

$$\tau_E = \frac{1}{\nu} = \omega(\tau_s + \tau_f) \tag{2.2.8}$$

The average sticking time τ_s is determined by the following equation[25, 10]:

$$\tau_s = \tau_0\, e^{\frac{H_a}{KT}} \tag{2.2.9}$$

- τ_0 $[s]$ is the lattice vibrational period;
- H_a $[J]$ is the adsorption enthalpy;
- T $[K]$ is the temperature.

Integrating the Equation (2.1.5), as done previously, it is possible to find the effusion contribution to the release efficiency:

$$\epsilon_E(\lambda) = \frac{\nu}{\nu + \lambda} \tag{2.2.10}$$

2.2.3 The general delay function $p(t)$

The general delay function (2.1.15) reported below has been discussed before as the equation that takes into account of both diffusion and diffusion mechanism.

$$p(t) = \int_0^t p_D(\tau)\; p_E(t-\tau)\mathrm{d}\tau$$

To solve it, it is necessary to suppose that the effusion occurs always after diffusion (i.e. re-diffusion does not happen) and replacing $p_D(t)$ and $p_E(t)$ respectively with (2.2.4) and (2.2.7) [53]:

$$p(t) = \frac{6\nu\mu}{\pi^2} \sum_{n-1}^{\infty} \frac{e^{-\nu t} - e^{-n^2\mu t}}{n^2\mu + \nu} \tag{2.2.11}$$

Trough the integration of Equation 2.1.5 it is possible to determine the final release efficiency:

$$\epsilon_{d+e}(\lambda) = \frac{3\nu}{\nu + \lambda} \left(\frac{W \coth(W) - 1}{W^2} \right) \tag{2.2.12}$$

$$W = \pi \left(\frac{\lambda}{\mu} \right)^{\frac{1}{2}} \tag{2.2.13}$$

Considering short-lived isotopes, for which $\lambda > \mu$, the Equation (2.2.12) becomes:

$$\epsilon(\lambda) = \frac{3\nu}{\pi(\nu + \lambda)} \left(\frac{\mu}{\lambda} \right)^{\frac{1}{2}} = \frac{3\nu}{r(\nu + \lambda)} \left(\frac{D}{\lambda} \right)^{\frac{1}{2}} \tag{2.2.14}$$

When the effusion is faster than decay, i.e. $\nu >> \lambda > \mu$, the Equation (2.2.14) can be transformed in:

$$\epsilon(\lambda) = \frac{3}{r} \left(\frac{D}{\lambda} \right)^{\frac{1}{2}} \tag{2.2.15}$$

In which the release efficiency only depends on the competition between the diffusion process and the radioactive decay.
The described theoretical concepts suggests which are the target key requirements and conditions in order to increase its release yield:

- Increase the working temperature as much as possible;
- Decrease the material grain size;
- Decrease the material adsorption enthalpy relative to the particle-surface interaction;
- Increase the target nuclei density;
- Decrease the number of collisions employing a proper geometry of the system;
- Increase the target nuclei cross section with the primary beam;
- Decrease the impurities inside the target material.

2.3 The SPES Target material properties

Once defined the controlling factors that increase the release efficiency, it is possible to describe the ideal material properties for an ISOL facility such as SPES.

2.3.1 The limiting temperature

To maximize the release yield it is necessary to increase the working temperature as much as possible, in particular the ideal target material *limiting temperature*, defined as the maximum working temperature [68].This parameter is not correspondent to the melting point, but it is correlated to the vapor pressure of the material: indeed if the vapor pressure is elevated, the ionization efficiency will be detrimentally affected[68]. The optimal ion source working pressure is indeed less than 10^{-4}-10^{-5} $mbar$; a pressure above these values will suddenly decrease the ionization efficiency.
Therefore a better definition of limiting temperature is the temperature to which the vapor pressure starts to reduce the ion source efficiency because of the presence of unwanted gas-phase molecules that contaminate the beam. Following these consideration, the materials having a vapor pressure below 10^{-4}-10^{-5} $mbar$ at 2000 °C are the best candidates for the target.
The vapor pressure P^{sat} $[bar]$ can be related to the vapor pressure curve by the Clausius–Clapeyron relation, which is valid in thermodynamic equilibrium between the two phases A and B [60]:

$$\frac{\mathrm{d}P^{sat}}{\mathrm{d}T} = \frac{\lambda_c}{T(v_A - v_B)} \tag{2.3.1}$$

- λ_c $[J/Kg]$ is the latent heat;
- v_A $[m^3/Kg]$ is the specific volume of the A phase;
- v_B $[m^3/Kg]$ is the specific volume of the B phase;
- T $[K]$ is the system temperature.

The Clapeyron equation is an exact thermodynamic relation, providing a vital connection between properties of different phases. When applied to the calculation of latent heats of vaporization, its use presupposes the knowledge of the vapor pressure-vs.-temperature relation. Because thermodynamics imposes no model of material behavior, either in general or for particular species, such relations are empirical.
The Antoine equation has the form [60]:

$$ln\ P^{sat} = A - \frac{B}{T + C} \tag{2.3.2}$$

A principal advantage of this equation is that values of constants A, B and C are readily available of a large number of species. Each set of values is valid for a specified temperature range, and should not be used much outside of that range.
The maximum service temperature may be influenced by reactions occurring during heating which change the material properties. These usually are thermal decomposition reactions that produce other unwanted volatile species, or phase transformations that change the material microstructure.

2.3.2 Thermal properties

Thermal conductivity and thermal emissivity are important properties that represent the capability of a material to dissipate the adsorbed energy.
The rate at which heat is conducted through a solid at steady state (meaning that the temperature profile does not change with time) is measured by the *thermal conductivity* λ $[W/mK]$, which is thus the ability of the target to dissipate the thermal power. Furthermore, the knowledge of the coefficient of thermal conductivity, the coefficient of thermal expansion α $[°C^{-1}]$ and the elastic modulus E $[GPa]$, allows to calculate the thermal stresses σ $[N]$ using the following Equation:

$$\sigma = |q|\ \Delta X\ \frac{E\ \alpha}{\lambda} \tag{2.3.3}$$

Where q $[W/m^2]$ is the heat flux and ΔX is the target thickness.
The *emissivity* is the capability of the material to return the absorbed heat by means of irradiation. The main heat transmission mechanism at the working conditions of the ISOL target is irradiation, which can be described by the Stefan-Boltzaman law:

$$q = \epsilon\ \sigma_{SF}\ T^4 \tag{2.3.4}$$

- q $[W/m^2]$ is the heat flux;
- ϵ is the emissivity;
- σ_{SF} is the Stefan-Boltzman constant.

After these considerations it is possible to establish the ideal thermal properties for the SPES target:

- High thermal conductivity both to dissipate the heat and to decrease the thermal stresses;
- Low thermal expansion coefficient to decrease the thermal stresses and distortions;
- High emissivity in order to dissipate the adsorbed energy as well as possible.

2.3.3 Chemical properties

The target material composition influences the isotopes production, indeed the occurring nuclear reactions are different for each material. Therefore the material chemistry is fundamental to get the desired isotopes. Moreover is important to choose a material having chemical properties very different from the produced isotopes in order to avoid the interaction between each other due to collisions.
In order to maximize the secondary beam intensity it is necessary to choose a material having a high superficial atoms density N_{target} and a high cross section σ as demonstrated in Equation (2.1.3). Looking at Equation (2.2.10),the term ν shall be increased rising up the adsorption enthalpy H_a, so

the final release efficiency will be enhanced. Furthermore the nuclides diffusivity inside the target must be elevated to minimize the overall delay time[4].

The material purity is significant: the impurities constituted by atoms with similar or higher masses with respect to the target nuclei will decrease the release efficiency because they can have a high stopping power[5] without contributing to the desired isotopes production; moreover, for the same reason, they increment the target temperature causing serious problems to thermal dissipation.

2.3.4 The material microstructure

A high limiting temperature of the material is not enough to ensure that the targets are characterized by a quick and efficient release of the produced species. Another important factor to consider is the material microstructure which has to be optimized to minimize the radioisotope release time maintaining both mechanical and thermal properties as high as possible. The aim is to get the smallest grain size without reducing too much porosity[6], to favor diffusion and increase the release yield.

The ceramic materials treated in this work are usually produced creating a "*green*" pellet by pressing powders and then heating it at high temperature under vacuum in order to let the chemical reactions and sintering (reaction sintering). Sintering of crystalline materials occurs by several mechanisms: vapor transport (evaporation and condensation), surface diffusion, lattice (volume) diffusion, grain boundary diffusion and dislocation motion (plastic flow) (Figure 2.3).

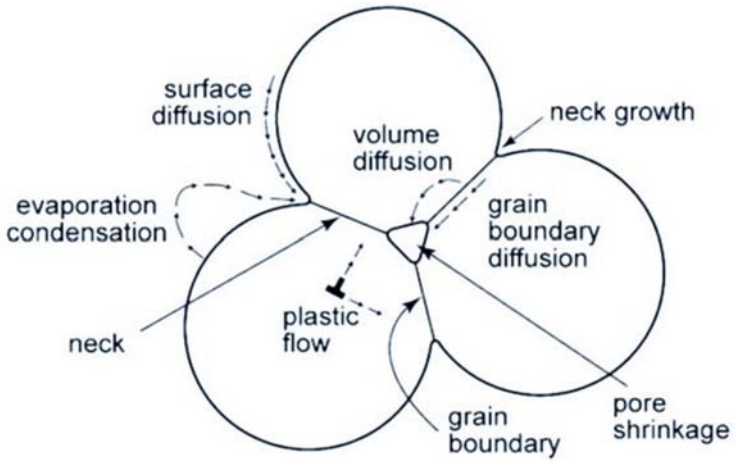

Figure 2.3: Schematic view of sintering mechanisms.[17]

It is empirically observed that when the sintering process occurs, the particles join together leading to grain growth and removal of pores: it is accepted that the reduction in free energy of a sintering compact due to the elimination of internal surface area associated with the pores, provides

[4]The delay time is defined as the elapsed time between the isotopes production an their effective use.

[5]Stopping power means the particle energy loss on traversing a unit distance in the medium due to particle-matter interaction.

[6]Porosity is a measure of the void fraction in a material.

the driving force for sintering. This can happen by reduction of the total surface area by an increase in the average grain size of particles, which lead to coarsening as schematized in Figure 2.4(b), and/or the elimination of solid/vapor interfaces and the creation of grain boundary area, followed by grain growth, which leads to densification as shown in Figure 2.4(a). If the atomic processes that lead to densification dominate, the pores get smaller and disappear with time and the compact shrinks. But if the atomic processes that lead to coarsening are faster, both the pores and grains get larger with time.

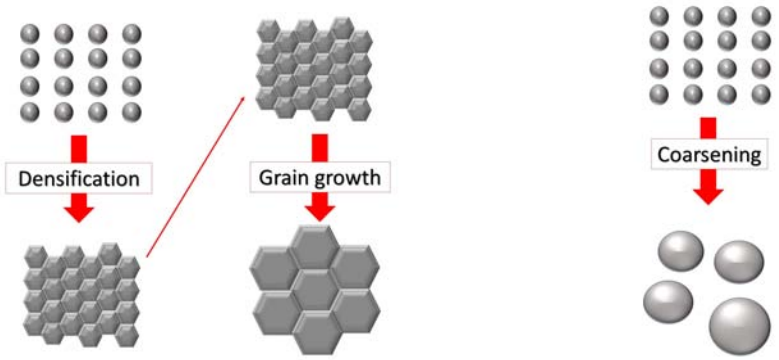

(a) Densification followed by grain growth.

(b) Coarsening where the large grains grow at the expense of the smaller ones.

Figure 2.4: Schematic of two possible paths by which a collection of particles can lower its energy.

Densification occurs if the grain boundary energy γ_{GB} is less than twice the solid/vapor surface energy γ_{SV}. This implies that the equilibrium dihedral angle ϕ shown in Figure 2.5 has to be less than 180°. In particular it is defined as:

$$\gamma_{GB} = 2\gamma_{SV} \cos\frac{\phi}{2} \tag{2.3.5}$$

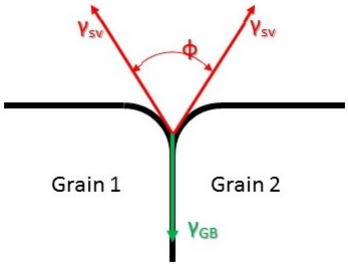

Figure 2.5: Equilibrium dihedral angle between grain boundary and solid/vapor interfaces.

Therefore, in general, the sintering rate depends on the initial particle size, self diffusion coefficient, temperature and indirectly on vapor pressure. In particular the first quantity is important: smaller starting powder sizes, R accelerate densification following the general dependence of

densification rate on $1/R^3$.

The porosity reduction increases the release time because the effusion rate in vacuum is always larger than the solid state diffusion. Consequently the granulometry of the starting powders will not be sub-micrometric because they favor the grains coalescence.

The porosity evaluation has to take into account several factors such as the porosity fraction, the pore size distribution and their morphology.

Concerning the total porosity fraction, it can be calculated by the following equation:

$$P = \left(1 - \frac{\rho_s}{\rho_{th}}\right) \tag{2.3.6}$$

Where P is the total porosity, ρ_s $[g/cm^3]$ is the measured sample density and ρ_{th} $[g/cm^3]$ is the theoretical bulk density.

The pores size is important because the released radioactive species travels easily inside larger pores giving a lower release time. Porous materials are classified into several categories by their pores size. The recommendations of a panel convened by the International Union of Pure and Applied Chemistry (IUPAC) are:

- **Microporous** materials have pore diameters of less than 2 nm;
- **Mesoporous** materials have pore diameters between 2 nm and 50 nm;
- **Macroporous** materials have pore diameters of greater than 50 nm.

The pore morphology influences the release efficiency, so it is necessary to distinguish between open pores, closed pores and interconnected pores, which are represented in Figure 2.8: the open pores are single voids present on the sample surface, closed pores are voids surrounded by the bulk material and interconnected (or permeable) pores are voids that connect the two material surfaces.

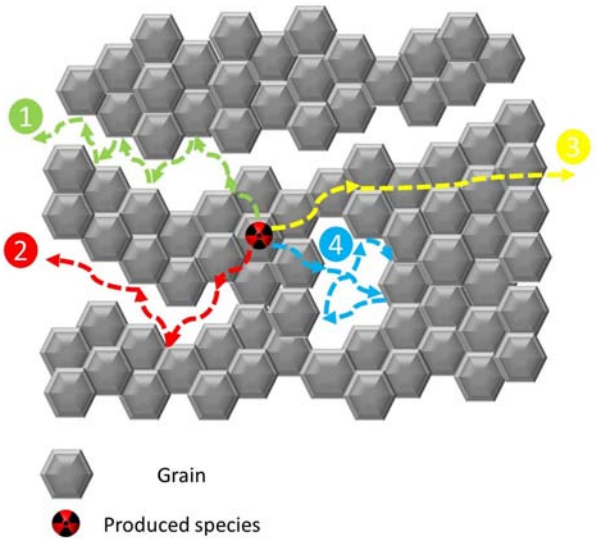

Figure 2.6: Equilibrium dihedral angle between grain boundary and solid/vapor interfaces.

The possible paths of the produced species are shown in Figure 2.8 and they are described as follow:

1. The isotope travels inside the interconnected pore, and after several bounces it reaches the target's surface. This kind of pores is the most efficient concerning the release efficiency, moreover they ensure less particle-particle and particle-target collision reducing the extraction time;

2. The produced species arrives in correspondence to the open pore which is directly connected to the external surface. Its depth is very small with respect to the target thickness, thus the isotope has to cross a lot of bulk material before reaching the surface; that is probably the reason why they are less efficient than interconnected pores ;

3. The particle diffuses inside the bulk material until it reaches a closed pore, where after several bounces it re-diffuses inside the matrix;

4. The radioisotope diffuses inside the bulk material, preferably through the grain boundaries, directly towards the outer surface.

The ideal microstructure is a compromise between the solid phase and the porosity: a large porosity will provide a huge release efficiency, but at the same time it decreases both the thermal conductivity and mechanical properties. Furthermore a minimum amount of solid phase is necessary to provide enough radioisotopes and ideally it must be characterized by a small grain size to enhance the release yield.

2.3.5 The system geometry.

The system geometry must be optimized in order to get a properly working ISOL target. The ideal target dimension can be determined from the Fick's law, which is opportunely rewritten in Equation (2.3.7) highlighting the the contribution of generation and decay of the isotopes to their concentration [68]:

$$\frac{\partial c(t)}{\partial t} = D\nabla c(t) + S(t) - E(t) \tag{2.3.7}$$

- t $[s]$ is the time;
- $c(t)$ $[mol/m^3]$ is the concentration;
- D $m^2/s]$ is the diffusivity, which is considered independent from the concentration;
- $S(t)$ $[mol/m^3 s]$ is the isotope production contribution;
- $E(t)$ $[mol/m^3 s]$ is the isotope decay contribution.

Equation (2.3.7) was solved in function of the target's geometry, the isotope half life and the diffusion coefficient [68]:

- $x[cm] = \pi \left(D\, T_{1/2}\right)^{\frac{1}{2}}$ for a plate of thickness x;
- $d_r[cm] = 4.8 \left(D\, T_{1/2}\right)^{\frac{1}{2}}$ for a rod of diameter d_r;
- $d_s[cm] = 2\pi \left(D\, T_{1/2}\right)^{\frac{1}{2}}$ for a sphere of diameter d_s;

2.4 The SPES Target's design

The first designed production target is composed of 7 co-axial discs made of uranium carbide having an external diameter and a thickness equal to 40 and $1,3$ mm, respectively; they are are spaced each other in order to to dissipate by thermal radiation the heat absorbed by the primary proton beam (see Figure 2.7)[46]. Two graphite circular windows of $0,2$ mm thickness are placed at the proton beam entrance to avoid the undesired emission of the nuclear fragments, while four circular graphite dumpers, with thickness ranging from $0,8$ mm up to 10 mm, stop the proton beam at the rear side of the target. All discs, windows, and dumpers are located inside a tubular hollow box made of graphite havin a diameter which measures 49 mm and a length of 200 mm.

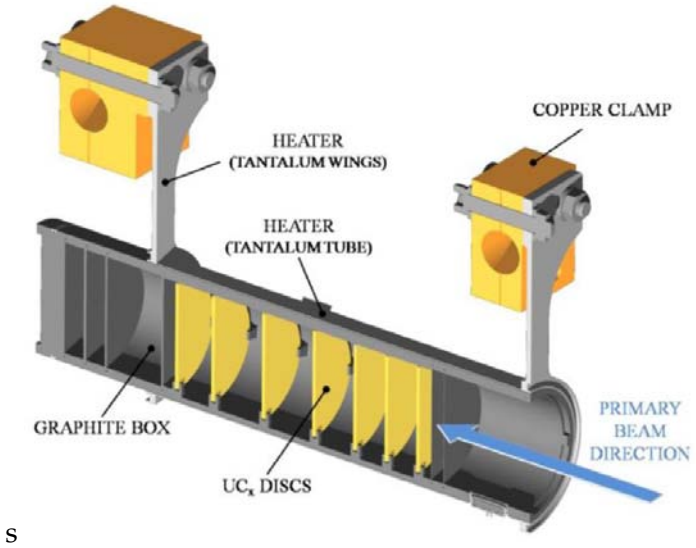

s

Figure 2.7: SPES production target.

The box is positioned inside the target heating system, which is composed of a tantalum tube with an average length of 200 mm, an external diameter of 50 mm and a thickness $0,35$ mm. It is welded at its edges to two tantalum segmented wings[7] which are directly connected to copper clamps, through which an electric current delivered by a 1 kW power supply (maximum current $i_{max} = 1000$ A and maximum potential $\Delta V_{max} = 10$ V) heats by Joule effect the Ta tube. Tantalum

[7]The thermal stresses, induced by the high system temperature, cause the deformation of the less stiffer element. If the wings would be stiff, the weakest element would be the tantalum tube which would be bended compromising the target. Thanks to the wings segmentation in more thinner plates, they becomes the less stiffer element of the structure maintaining the tantalum tube undeformed.

was chosen to build the heating system because it is an highly corrosion resistant transition metal with very good thermal and electrical conductivity (thermal conductivity and electrical resistivity at room temperature equal to 57 W/mK and $1,34 \cdot 10^{-7}\ \Omega \cdot m$, respectively, both increasing with temperature increase) and capable of operating at very high temperatures: considering a working pressure of $10^{-4}\ Pa$, Ta starts to sublimate at approximately 2200 °C. Moreover thanks to its low emissivity (0, 15 at 1000 °C and 0, 26 at 2000 °C), tantalum is able to screen efficiently the target box, limiting the cooling effect by thermal radiation. Another important component of the target block is the transfer line, through which the radioactive atoms are transported from the production target to the ion source by effusion. The transfer line itself is kept at high temperature to increase the mobility of the atoms, but in some cases it can be water cooled to improve the selectivity of the system. When the transfer line works at high temperature it is heated by Joule effect making use of the same electrical circuit adopted to heat the ion source. [46]

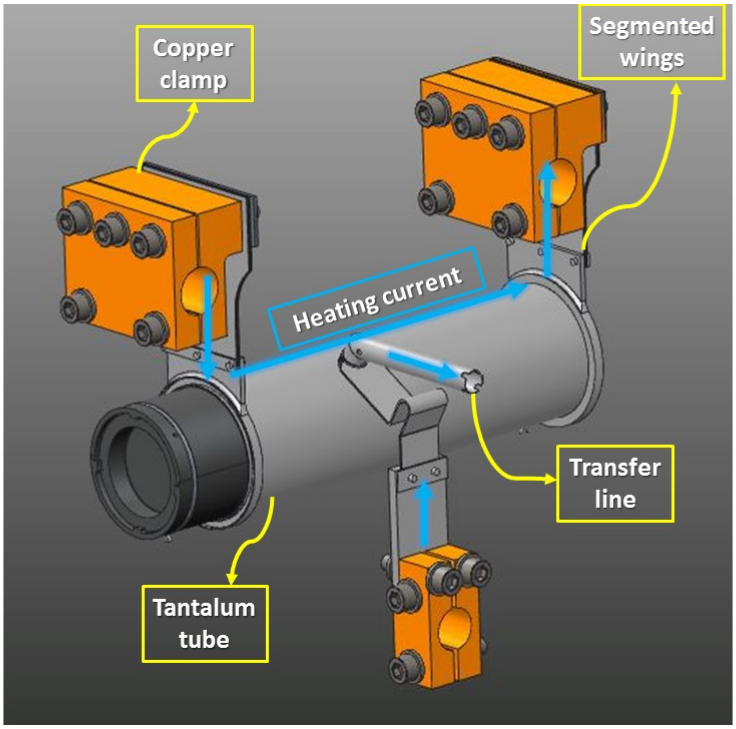

Figure 2.8: Target heating system and transfer line.

2.5 Conclusions

In this chapter the radioisotopes production and release from the target has been clarified: through theoretical equations it has been possible to understand which are the process-controlling parameters.

The reaction products intensity $I_{production}$ depends on the primary beam intensity, the cross section and the target atoms superficial density, while the secondary beam intensity I depends on $I_{production}$ and the overall process efficiency, i.e. the release efficiency, the ionization efficiency and the transport efficiency.

In particular, the release efficiency is characterized by two contributions: the diffusion through the solid phase and effusion towards the vacuum chamber. The former increases with the system temperature and the grain size reduction, while the latter increases reducing the material adsorption enthalpy H_a because it influences the sticking time of particles.

These considerations permit to define the ideal material properties to increase as much as possible the release efficiency: its limiting temperature (defined by the vapor pressure) must be high, as well as the thermal conductivity and emissivity. The thermal expansion coefficient has to be low in order to avoid thermal thermal stresses and thus distortions. The chemical properties of the produced isotopes and the production target should be ideally very different, in order to limit the particle-surface interaction and adsorption during the release process.

From the microstructural point of view, the porosity helps the isotopes' effusion, but at the same time it limits the mechanical properties, thus is necessary to achieve a compromise between the solid phase and the porous phase. Moreover the preferred pore morphology is the interconnected (or permeable) one.

The system geometry is fundamental to reach an high release efficiency, indeed thanks to relations derived from the Fick's law it is possible to define the ideal target dimensions: they depend on the target geometry and on the isotopes diffusivity and on isotopes half-life.

Finally the system design that has to take into account of the overall process issues has been described.

The next chapter will provide information concerning the materials that can be really employed to build the target. Obviously they have to satisfy all the aforementioned conditions.

CHAPTER 3

Materials for SPES target and their properties

The importance of the material choice has been pointed out previously, thus this chapter will describe the materials which can be used. In particular more detailed information will be given concerning the materials treated in this thesis work: titanium carbide, zirconium carbide and zirconium germanide.

3.1 Introduction

The material choice for the ISOL target is related to the type of nuclear reactions which occur when it interacts with the primary beam.
The neutron-rich isotopes can be produced by a single target material, indeed it can provide the whole desired spectra of isotopes if it is fissile[1] and if its interaction with the primary beam offers a large enough cross section. Regarding the proton-rich isotopes, usually a single target material is able to produce only a limited spectrum of species by means of direct reactions.
The material classes tested as ISOL targets can be classified as follows [24]:

- **Oxides**

  Oxides are generally produced by powders sintering, but they may be constituted by fibers or deposited over permeable substrates. The main problem of this kind of material is their reactivity with other target components which are usually made of graphite or tantalum: the occurring of an undesired target-heating system interaction may lead to a lower material limiting temperature. Therefore, in order to avoid any possible reaction, the tantalum components can be coated with a tungsten or rhenium thin layer. Furthermore metal oxides can not be put in contact with graphite at high temperature, otherwise their reduction occurs eliminating a huge amount of gaseous CO.

[1] A nuclide that is capable of undergoing fission after capturing low-energy thermal (slow) neutrons or charged particles.

Oxides are characterized by a high limiting temperature (more then 1800 °C), moreover they can be produced with a great purity with respect to carbides. However their release is slower than carbides, furthermore a long-term operation of oxides is limited by their sintering at the operating temperature penalizing the short-lived isotopes release.

The oxides commonly used as ISOL targets are ZrO_2, CeO_2 and HfO_2 [62, 54], which are characterized by a limiting temperature of 2200, 1800 and 2200 °C, respectively. As shown in Figure 3.1 they can be simulated as target materials by FLUKA software in order to estimate the produced isotopes amounts.

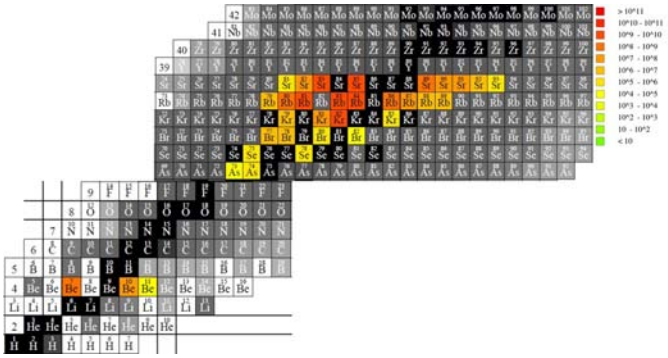

(a) Isotopes produced by ZrO_2 target.

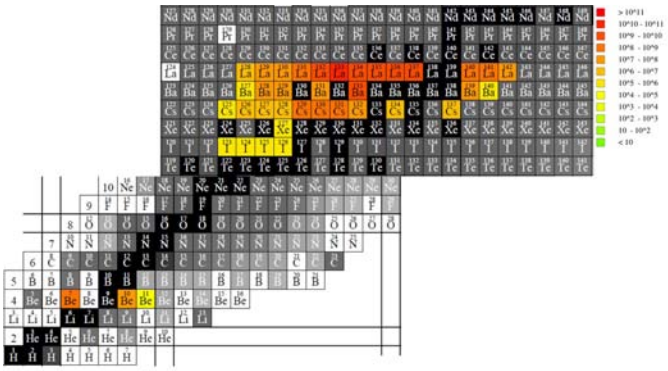

(b) Isotopes produced by CeO_2 target.

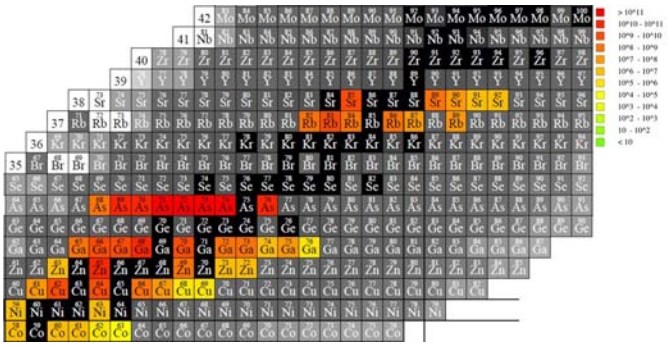

(c) Isotopes produced by HfO_2 target.

Figure 3.1: FLUKA isotopes production simulation starting from oxide targets. The simulation was done assuming a primary proton beam intensity of 40 MeV , a current of 5 μA and the target heated at its limiting (working) temperature.

- **Sulfides**

  Only few sulfides have a limiting temperature high enough to satisfy the ISOL technique requirements. One of them is the CeS, which has a working temperature of about 2000 °C and it is used to produce the isotopes in Figure 3.2. Its limiting temperature falls when it is put in contact with tantalum or graphite as well as for oxides.

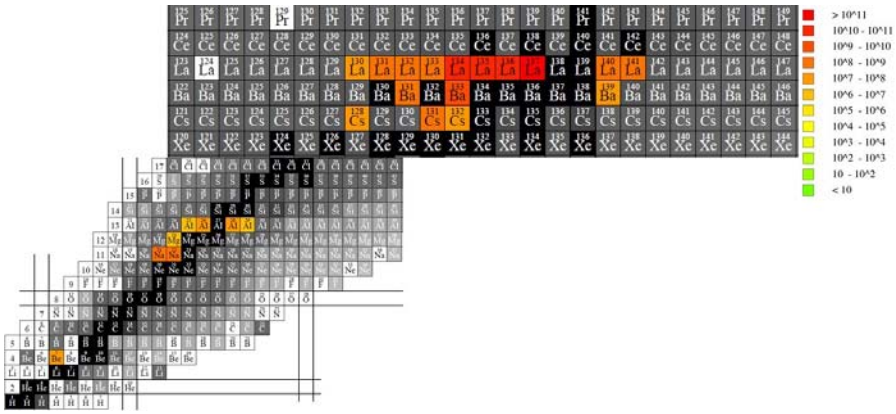

Figure 3.2: FLUKA isotopes production simulation of a target made of CeS. The parameters that are used to run the simulation are: primary proton beam intensity of 40 MeV , a current of 100 μA and a working temperature of 2000 °C.

- **Pure metals**

  Pure metals can be used as ISOL targets in form of both sintered powders and thin foils, especially for spallation based production. Metals which belong to groups 4 and 5 of the periodic table are the most appreciated because of their high limiting temperature and their fast isotope release. For example the RIST target, which was developed and tested at ISOLDE[2], is made of 3600 discs of 25 μm thick tantalum each with a hole in the middle of their surface. It was demonstrated that it ensure a good release efficiency for short-lived isotopes.

  Also liquid metal targets were tested at HRIBF[3] [62].This kind of target are characterized by a huge diffusion rate, moreover convection currents enhance the nuclei release bringing them close to the liquid surface. The main problems are the complex target design and the reactivity with the support materials, since they tend to be very corrosive.

  Using liquid germanium as target is possible to produce arsenic and gallium isotopes, while liquid nickel provides copper isotopes.

- **Carbides**

  Carbides are the most interesting materials for the ISOL target production due to their capability of efficiently releasing short-lived isotopes. Furthermore, in order to improve their release rate, it is possible to disperse inside the matrix of the desired carbide some graphite

[2]ISOLDE is an ISOL facility which is located at the Proton-Synchrotron Booster (PSB) at CERN.

[3]HRIBF was an ISOL facility which was located at Oak Ridge National Laboratory.

(excess of carbon). [54]

However, a more detailed analysis on carbides will be done in the next section.

3.2 Carbides

Carbon forms compounds with most elements but, by convention, the term carbide is used only for those compounds formed by carbon and other elements of lower or about equal electronegativity. The carbides can be classified in four categories [52]:

- **Interstitial carbides** formed formed by transition metals of groups IV, V and VI. The difference in electronegativity between the two elements is large, moreover the carbon atom is much smaller than the metal one, thus it occupies the octahedral interstices of the close-packed metal lattice . Because of their bonding which is partly covalent and ionic, they assume a metallic-like behavior: the electronic band structure and other properties of the pure metal are not influenced by the presence of the carbon atoms which further stabilize the lattice. They are characterized by high thermal and electrical conductivity, hardness, melting point and they are chemically inert. If the metal atomic radius is large enough, monocarbides (ZrC, TaC, HfC) are formed;

- **Covalent carbides** formed by Si (silicon carbide, SiC) and B (Boron carbide, B_4C). The difference in electronegativity between the two elements is small as well as the difference between the atoms size. Only silicon carbide and boron carbide fulfill the refractory criteria;

- **Intermediate carbides** formed by transition metals of groups VII and VIII. The atomic radius is too small to accommodate the carbon atom in interstitial positions without distortion of the lattice. As consequence, the carbon atoms are close enough to each other resulting in carbon-carbon bonds. These carbides are not chemically stable, indeed they can be hydrolyzed by water, while in contact with dilute acids they tend to form hydrocarbons and hydrogen. Chromium carbide (Cr_3C_2) is an exception, in fact it is considered as a refractory border-line case;

- **Salt-like carbides** formed by the elements of groups I, II and III. They are called salt-like because the high electronegativity difference leads to an atomic bond which is at least 50% ionic. They have a fixed composition, they are generally transparent to optical radiation and are good electrical insulator. Some of them have a high melting point, such as beryllium carbide, but they are easily decomposed by water or dilute acids at ordinary temperatures. Alkaline, alkaline-earth and lanthanide carbide contains the C_2^{2-} are called acetylides, indeed in contact with water they release acetylene according to the following chemical reaction:

$$CaC_2 + 3\,H_2O \longrightarrow Ca(OH)_2 + HCCH$$

However lanthanide carbides and some actinide carbides such as UC_2, present a C−C bond length larger than CaC_2, moreover the metal in their structures is basically trivalent: three electrons are shared in the metal-carbon bond, consequently it results in a higher electrical conductivity.

The term *refractory* means a material with melting point over above 1800 °C (for convention), and a high degree of chemical stability. Only the interstitial and covalent carbides satisfy these two conditions, thus the other two classes can not be considered as refractory.[52]
The carbides synthesis can be done by using different methods which were widely studied and improved during last years. The main issue of the whole processes is the oxygen contamination, which hugely influences the material properties even at very low concentrations. The oxygen dissolution in the material can occur quickly if the carbon lattice is not saturated by carbon atoms, while if the process foresees the gradual removal of carbon atoms from the lattice, oxygen dissolves more slowly.
To avoid the oxygen presence in the carbon lattice it is necessary to perform the thermal treatment (temperature up to 2000 °C) in high vacuum (pressure of about 10^{-6} *mbar*).
The carbides most common synthesis methods can be resumed as follows [52]:

- **Carbothermal reduction**: the process occurs in an inert atmosphere starting from an homogeneous mixture of oxide powders and carbon. Usually the reaction is carried out under high vacuum conditions to avoid the oxygen dissolution inside the material, furthermore furnace is heated at high temperature (up to 2000 °C) to ensure both chemical reactions and sintering. The following paragraphs will give more details regarding this kind of reaction because the SPES targets realized for this work were prepared employing this method;

- **Direct reaction**: reacting carbon and the pure metal at high temperature (2000 °C) together leads to the formation of carbides of different stoichiometries. The main issue of this process is related to the high reactivity of the metal powders with air which allows the the metal oxide formation and finally the oxygen contamination;

- **Gaseous reaction**: the pure metal reaction with gaseous hydrocarbons provides the final carbide. This method is generally used to form thin films; it requires a lower temperature with respect to direct reaction, but the employed gas must be highly pure raising up the cost. Moreover, the metal powder granulometry must be really small in order to increase the surface available for the gas-solid reaction, consequently the oxygen contamination can easily occur;

- **Sol-gel process**: a liquid precursor aimed to provide the metallic element for the reaction is mixed with a well-defined solvent to obtain a colloidal suspension. Then it is transformed into a gel[4] through hydrolysis and condensation reactions. Finally the gel is dried to obtain a solid metal precursor-carbon precursor mixture which is pyrolized to form the carbide. The required temperature is lower than the other production processes.

3.2.1 Uranium carbide UC_x

Uranium carbide is the most common ISOL target material [24] because of its short delay times for a variety of fission produced isotopes. In particular, when graphite is dispersed in excess inside the uranium carbide matrix, the material is commonly referred to as UC_x .
As shown in Figure 3.3 three compounds exist in the uranium-carbon system: uranium monocarbide (UC), uranium sesquicarbide (U_2C_3), and hypostoichiometric uranium dicarbide (UC_{2-x}).[33]

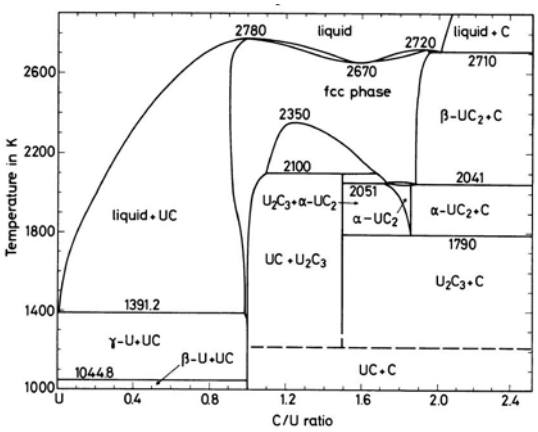

Figure 3.3: Phase diagram of the uranium-carbon system.[33]

UC is characterized by a face-centered cubic (fcc) NaCl-type structure as reported in Figure 3.4(a), and it is the most stable phase from room temperature up to 2700 K. When the temperature overlaps 1500 K it can exist in both hypostoichiometric (with vacancies in the carbon sublattice) and hyperstoichiometric (with C_2 groups instead of carbon atoms) forms, which are usually indicated as $UC_{1\pm x}$.
UC_2 is stable above 1750 K and melts at about 2700 K, moreover it shows two polymorphisms: indeed the transformation from the low temperature tetragonal form α-UC_2 to the high temperature cubic form β-UC_2 (see Figure 3.4(b)) occurs at 2050 K. Both forms are characterized by a range of hypostoichiometry (α-UC_{2-x} and β-UC_{2-x}), the limits of which are determined by their equilibrium with U_2C_3.[33]

[4]Gel is defined as a 3D interconnected solid skeleton enclosing a continuous liquid phase.

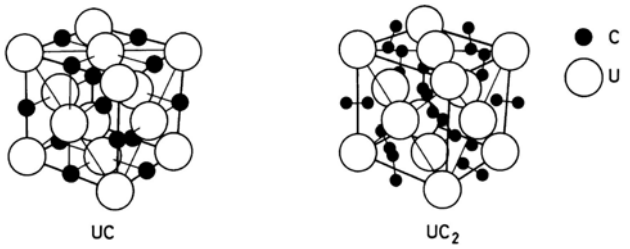

(a) Uranium monocarbide structure.

(b) β-uranium dicarbide structure.

Figure 3.4: Difference between β-UC_2 and UC structures.[33]

U_2C_3 has a body-centered cubic structure as shown in Figure 3.5, furthermore it is stable from 1200 k to 2100 K. Below these temperatures it exists as a metastable phase since UC+C are the stable phases. U_2C_3 decomposes with a peritectoidal reaction into UC_{1+x} and β-UC_{2-x}[33].

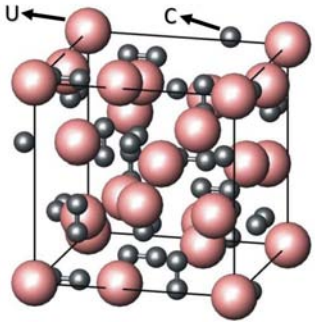

Figure 3.5: Uranium sesquicarbide structure: the dicarbide anions occupy the voids in bisphenoids of the metal substructure.[64]

Uranium carbide was studied a long in the '50s because its properties are similar to uranium dioxide which was used as a fuel for nuclear reactors, whereby the following Table 3.1 resumes some of their properties.

Table 3.1: Comparison between UC and UO_2 properties.[24]

Property	UC	UO_2
Theoretical density $[g/cm^3]$	13,63	10,97
Uranium density $[g/cm^3]$	12,97	9,67
$T_{melting}$ [°C]	2390	2800
Thermal conductivity between 200 and 1000 °C $[W/m \cdot K]$	23	3,6
Thermal expansion coefficient [$°C^{-1}$]	$1,1 \cdot 10^{-5}$	$1,0 \cdot 10^{-5}$

Table 3.2 compares the properties of the three different aforementioned compounds, they are useful to understand the composition that satisfy better the ISOL target requirements.

Table 3.2: Properties comparison between UC, UC_2 and U_2C_3.[24]

Material	UC	U_2C_3	UC_2
Theoretical density $[g/cm^3]$	13,63	12,7	11,28
Uranium density $[g/cm^3]$	12,97	11,81	10,25
T melting [°C]	2390	1820	2427
Crystal structure	NaCl type - FCC	BCC	α: CaC2 type - tetragonal β: NaCl type - FCC
Thermal conductivity $[W/mK]$	$20 \div 25$ (1000 ÷ 2000 °C)	$13 \div 20$ (600 ÷ 2060 °C)	$11 \div 16$ (790 ÷ 1790 °C)

The influence of the type of uranium carbide used as a target was recently analyzed, in particular the research showed that UC_2-based targets possess generally better release than UC-based targets, especially when their production results in a higher porosity with respect to monocarbide targets [34]. Therefore the final form of uranium carbide which will be used as SPES target will be the UC_2 + xC one[13]. The uranium vapor pressure for a ratio $C/U = 2$ is about 10^{-5} *mbar* at 2000 °C [61], thus it can satisfy the ion sources requirements of working in a clean environment.

The common synthesis method to carry out the carbothermal reduction of uranium oxide with carbon which can be schematized as follows :

$$U_xO_y + (z + y + n)C \longrightarrow U_xC_z + nC + yCO$$

The reaction occurs at high temperature under vacuum to avoid oxygen contamination, furthermore working in high vacuum allows permits to obtain the desired reaction at lower temperatures with respect to the inert atmosphere and finally the developed gaseous CO during the reaction enhance the formation of pores resulting in a better isotopes release.

Different kind of uranium oxides as precursors were tested [13], in particular UO_2, U_3O_8 and UO_3: thanks to mass spectroscopy it was possible to notice that the precursor oxides U_3O_8 and UO_3 decomposed to UO_2 mainly with CO_2 emission before the carbothermal reaction took place. Carbothermal reduction starts at $T > 1000$ °C, and it completes at about 1600 °C.

The morphology does not present significant variations in terms of grain size and porosity changing the starting oxide.[13]

Also different kind of carbon precursors were tested : the use of carbon nanutubes for lanthanum carbide production leads to a final material with a controlled amount of porosity, with the pores dimensions raging from few nanometers to some microns [22, 12, 14]. Lanthanum dicarbide (LaC_2)

was suggested as a substitute of uranium compounds for preliminary bench tests on the production and characterization of highly porous carbides because it has very similar properties to UC2 and it is not radioactive.

Thanks to the FLUKA simulation represented in Figure 3.6 the spectrum of the isotopes that can be released and collected from the UC_x target at SPES was obtained. It can be divided in two zones: a low mass (zone a, from Ni to Y) and a high mass (zone b, from Ag to La) regions when the target is heated at about 2000 °C.

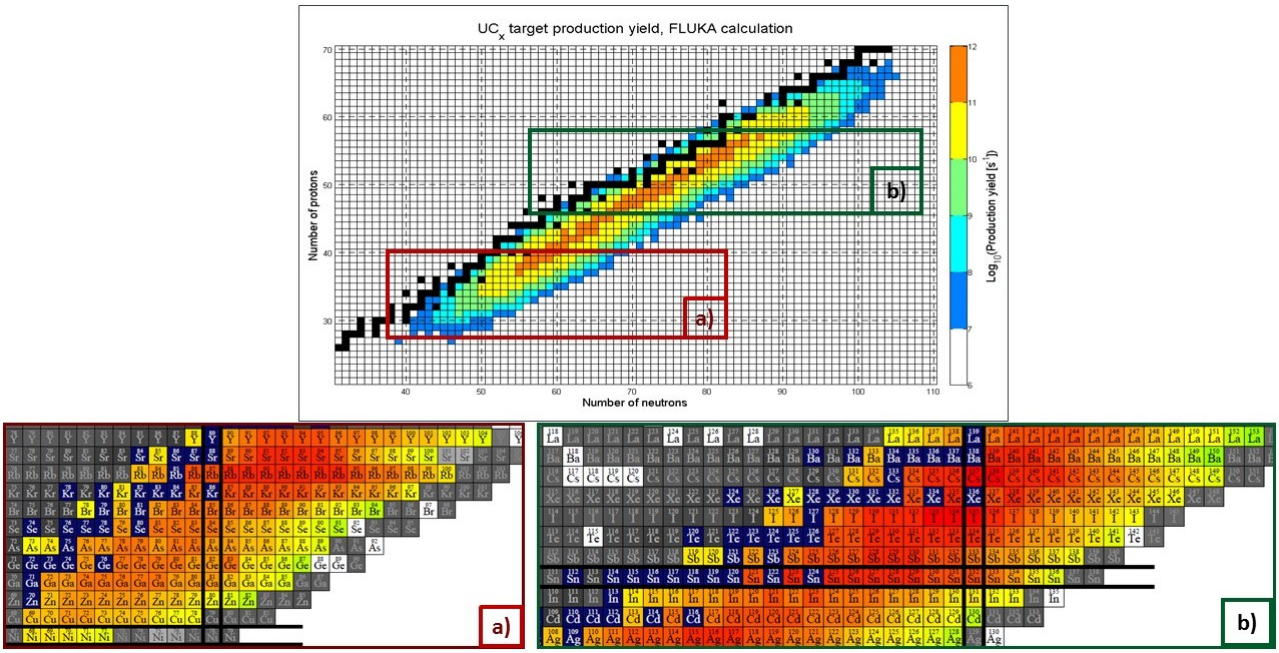

Figure 3.6: Isotopes production from UC_x target provided by the FLUKA simulation. Primary proton beam energy= 40 MeV, current= 200 μA, working temperature=2000 °C.

The temperature of 2000 °C is achievable in all the seven discs combining the heat provided by both the proton beam bombardment and the heating system already described in Section 2.4. The power and temperature distribution inside the target and the average temperature reached in each disc were simulated by the ANSYS software and the results are respectively shown in Figure 3.7 and 3.8.

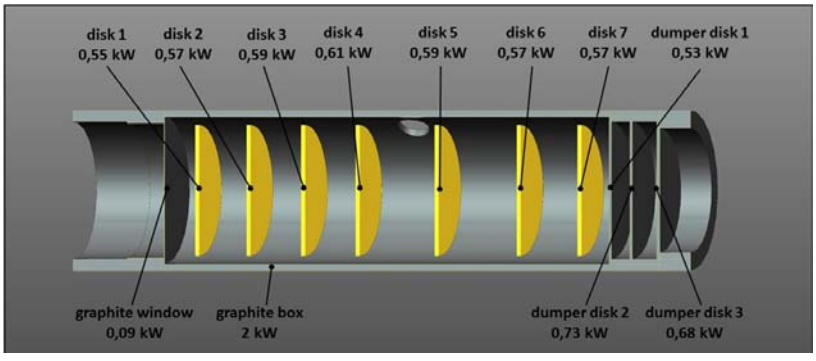

Figure 3.7: Power distribution for each target disc.

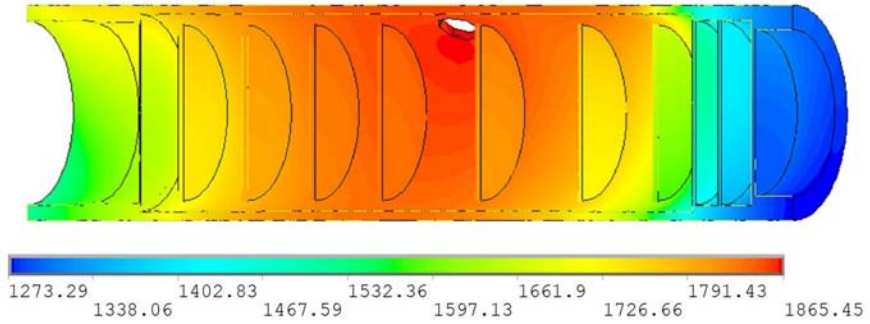

(a) Target heating due to Joule effect .

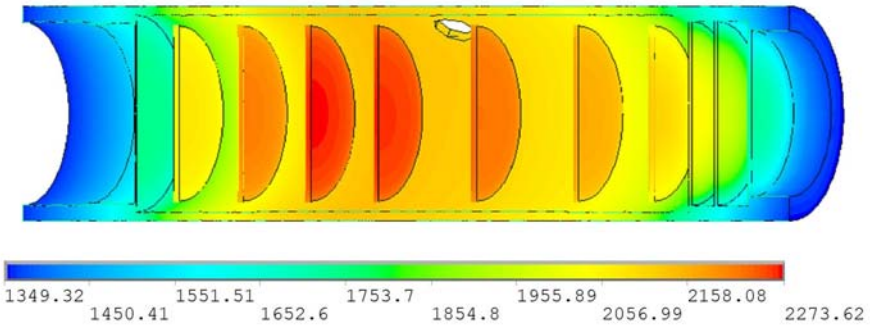

(b) Target heating due to interaction with the primary beam.

Figure 3.8: Target temperature distribution.

After the SPES uranium carbide target prototype realization, characterization and simulation, it was finally tested at HRIBF using a 40 MeV proton beam with intensity of approximately 50 nA [24]. The secondary beam intensities of 21 elements and about 77 isotopes were measured: their yields expressed $[ions/\mu A \cdot s]$ are collected in Figure 3.9, moreover they accord with the simulated spectrum already exposed in Figure 3.6.

This On-Line test was the first evidence that a target with this innovative geometry is capable of producing and quickly releasing fission products.[57]

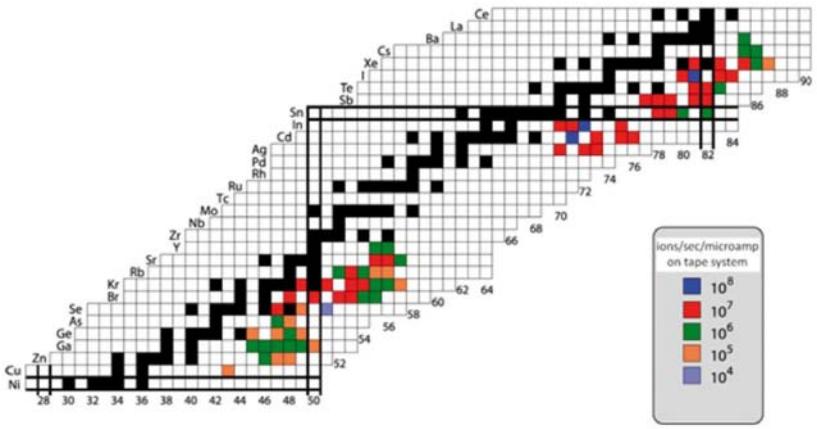

Figure 3.9: Radioactive isotopes experimentally observed with a "Standard" UC_x target at 2000 °C.[57]

3.2.2 Titanium carbide TiC

Titanium carbide (TiC) is an interstitial carbide of group IV characterized by a high hardness, strength, stiffness and wear resistance. Due to this characteristics it is industrially used as:

- a secondary carbide in cemented tungsten carbide cutting and grinding tools;
- coating for cutting tools, stamping, feedscrews for the chemical industry and for other mechanical component subjected to wear;
- coating on graphite for limiters and neutral beam armor in nuclear fusion applications.

Concerning the SPES project, the target made of TiC ensures the production of isotopes of Figure 3.10 after the interaction with the primary beam. In particular the produced isotopes ^{43}Sc, ^{44}Sc and ^{45}Sc are the most important and innovative for ISOLPHARM, since they can be employed both for therapy and diagnosis.

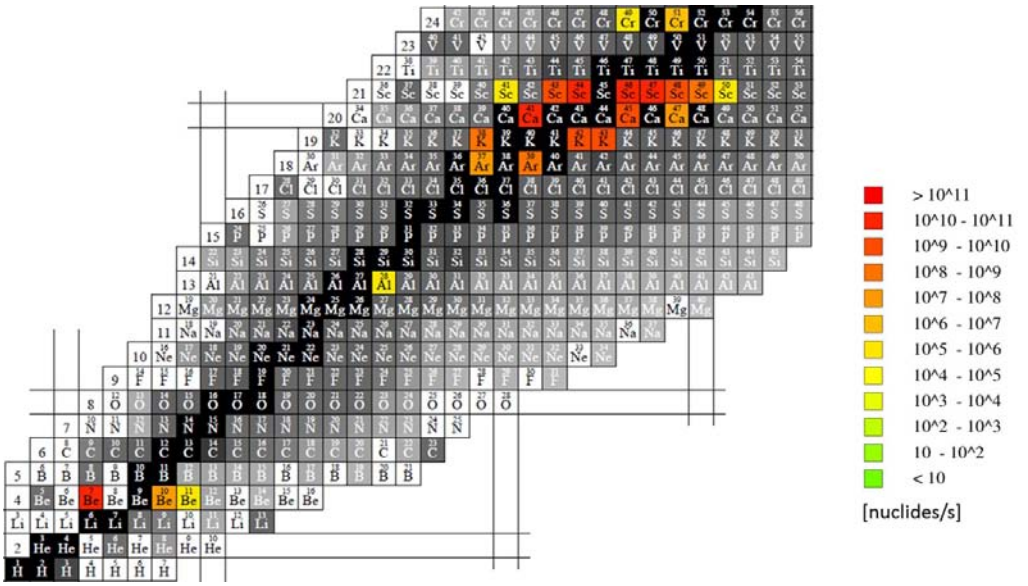

Figure 3.10: Isotopes production from TiC target provided by the FLUKA simulation. Primary proton beam energy= 40 MeV, current= 200 μA, working temperature=2200 °C.

Analyzing the C-Ti phase diagram in Figure 3.11, the only stable composition is the monocarbide which is characterized by cubic closed packed (CCP) structure in which Ti atoms are disposed in a face-centered cubic structure and C atoms occupy the octrahedal voids at stoichiometry[5]. Furthermore it is important to observe the extremely high melting temperature which satisfy the refractoriness requested by the SPES target.

The thermal conductivity k of interstitial carbides is different from that of most other refractory materials, in fact k increases with increasing temperature as shown in Figure 3.12(a).

The thermal conductivity can be considered as the sum of two contributes as in Figure 3.12(b):

[5]FCC B1, NaCl type structure.

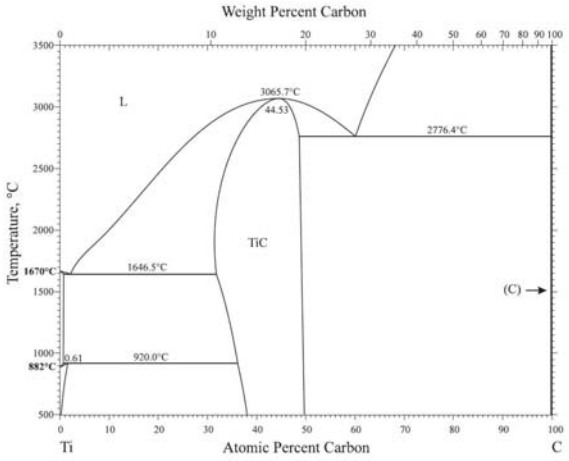

Figure 3.11: Ti-C system phase diagram.[50]

the electron thermal conductivity k_e, and phonon (lattice) conductivity k_p. The increase in thermal conductivity with temperature is believed to be the result of strong scattering of electrons and phonons by carbon vacancies in addition to the scattering of electrons by polar optical phonons and the scattering of phonons by the conduction electrons.[52]

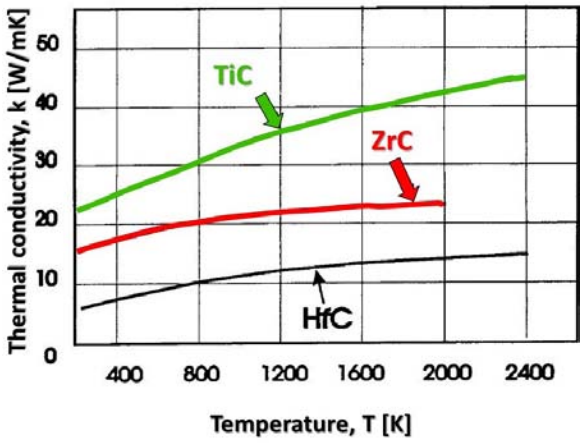

(a) Thermal conductivities of Group IV carbides as a function of temperature.

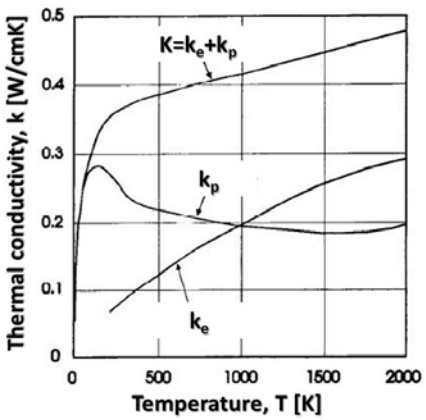

(b) Electron and phonon conductivity (k_e and k_p, respectively) of TiC as a function of temperature.

Figure 3.12: [52]

Generally, interstitial carbides are characterized by a huge strength even at high temperature. Nevertheless, like most ceramics, they are intrinsically brittle: this behavior of carbides is due to their strong hybrid ionic-covalent bonds wich means a relatively weak metal-to-metal bond but a strong metal-to-carbon bond. The latter prevent the plastic deformation as occurs in ductile metals. If the plastic deformation does not occur, the fracture will be brittle since applied stresses tend to concentrate at the sites of flaws as voids or chemical impurities at grain interfaces.
The interstitial carbides can be deformed plastically above a given temperature, defined as ductile-

to-brittle transition temperature. This temperature depends on several factors such as grain size, composition and impurity contents.

The hardness is a complex property which depends on the fabrication property, composition and the presence of impurities. In Figure 3.13(a) the hardness variation with composition of different carbides can be observed: it increases gradually until the stoichiometry is reached. Moreover when the temperature increases, the hardness decreases as shown in Figure 3.13(b); the exception is WC which remains hard until about 800 °C.

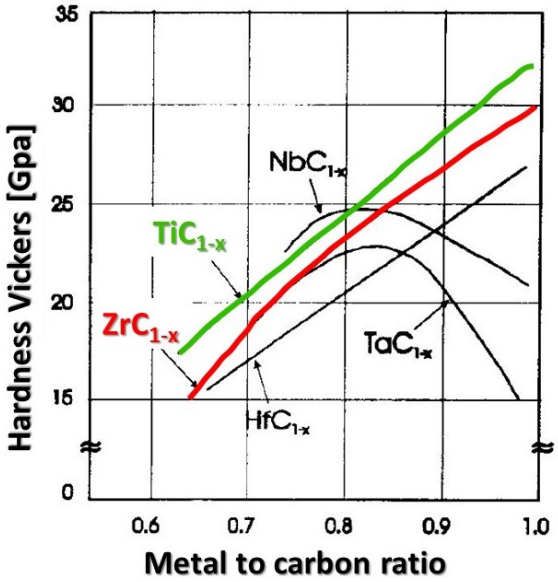

(a) Hardness of refractory carbides as a function of metal-to-carbon ratio.

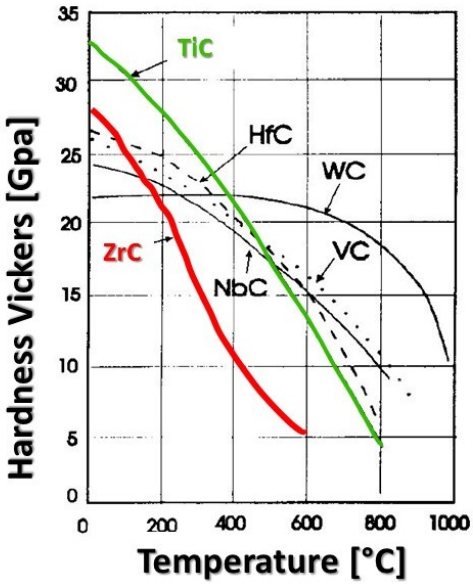

(b) Hardness of refractory carbides as a function of temperature.

Figure 3.13: [52]

Regarding the TiC oxidation resistance, it oxidizes slowly in air at 800 °C; therefore the production process which will be described in the following chapter, must be conducted under vacuum conditions to obtain a pure carbide. However it is chemically inert to most acids, it is attacked by HNO_3, HF and the halogens.
The following Table 3.3 gives the TiC bulk properties which can be influenced by the following factors [52]:

- Stoichiometry;
- Impurities, in particular oxygen and nitrogen;
- Grain size and morphology;
- Grain orientation;
- Structural defects;
- Presence of different undesired phases.

Table 3.3: TiC bulk properties. [52]

Property	Value
Theoretical density $[g/cm^3]$	4,91
Melting temperature [°C]	3067
Thermal conductivity $[W/mk]$ at 20 °C	21
Coefficient of thermal expansion $[C^{-1}]$ at 20 °C	$7,4 \cdot 10^{-6}$
Electrical resistivity $[\mu\Omega \cdot cm]$ at 20 °C	50 ± 10
Hardness Vickers $[GPa]$	28-35
Young's modulus $[GPa]$	410-510
Transverse ropture strength $[MPa]$	240-390

3.2.3 Zirconium carbide ZrC

Zirconium carbide (ZrC) is a highly refractory compound but, unlike titanium carbide, it has found only limited industrial importance except for nuclear-fission power plants, indeed Zirconium-carbide CVD coatings are used extensively on atomic-fuel particles such as thoria and Urania. Its high cost and difficulty in obtaining it without impurities limit its use for industries. Regarding the SPES project, a ZrC ISOL target releases the interesting isotopes in Figure 3.14 when it interacts with the primary beam, moreover ZrC has a reported vapor pressure of Zr at 2300 °C of $6 \cdot 10^{-6}$ *mbar* [30], so it can be considered suitable for this application.

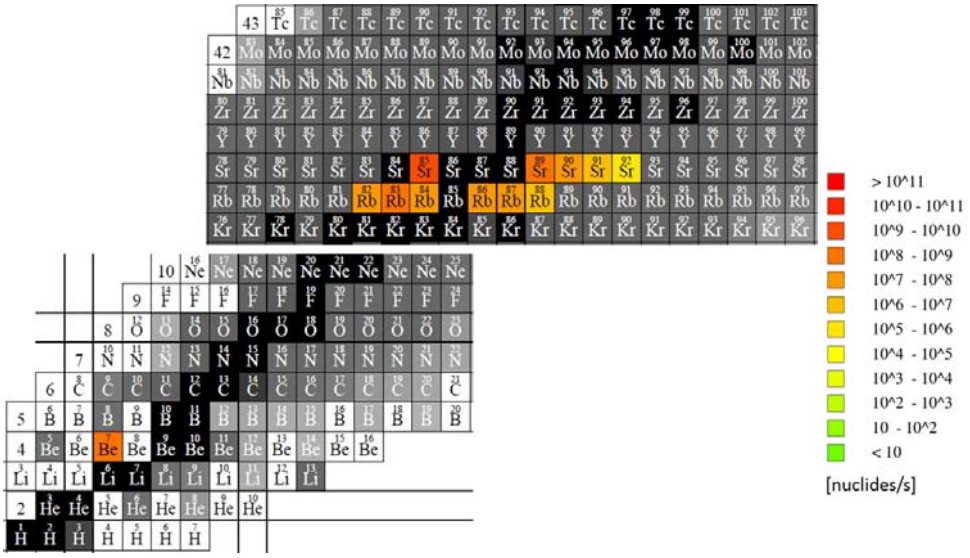

Figure 3.14: Isotopes production from ZrC target provided by the FLUKA simulation. Primary proton beam energy= 40 MeV, current= 200 μA, working temperature=2200 °C.

The phase diagram of Zr-C systems in Figure 3.15 shows that the monocarbide is the only stable phase and it is face centered cubic (FCC), rock salt structure (NaCl-like) whereby the carbon atoms occupy the interstitial octahedral sites. The carbide can accommodate non-metal vacancies andis generally indicated with the non-stoichiometric formula ZrC_{1-x}.

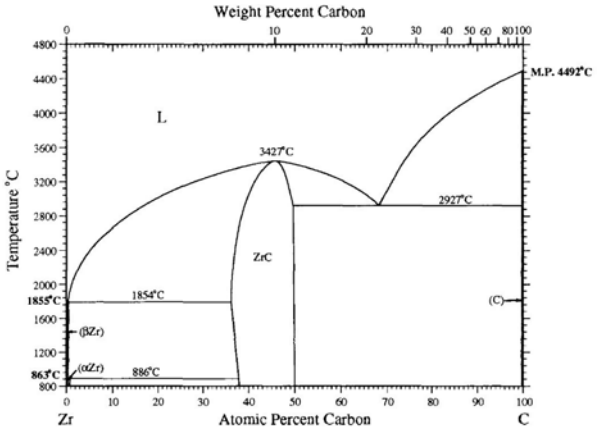

Figure 3.15: Zr-C system phase diagram.[49]

ZrC properties behavior is similar to the TiC ones as seen in the previous paragraph in Figure 3.12 and Figure 3.13: this is due to the fact that the materials are characterized by the same type of atomic bonding and structure. Some of ZrC properties are collected in Table 3.4.
ZrC is not chemically resistant as TiC, it oxidizes at about 800 °C and it is dissolved by cold HNO_3 and by a cold mixture of H_2SO_4 and H_3PO_4, furthermore it reacts easily with halogens.

Table 3.4: ZrC bulk properties. [52]

Property	Value
Theoretical density $[g/cm^3]$	6,59
Melting temperature [°C]	3420
Thermal conductivity $[W/mk]$ at 20 °C	20,5
Coefficient of thermal expansion [$°C^{-1}$] at 20 °C	$6,7 \cdot 10^{-6}$
Electrical resistivity $[\mu\Omega \cdot cm]$ at 20 °C	45±10
Hardness Vickers $[GPa]$	25,5
Young's modulus $[GPa]$	350-440
Transverse ropture strength $[MPa]$ [20]	550

The synthesis method used in this thesis work to produce ZrC is the aforementioned carbothermal reduction which can be described by the following equation[55]:

$$\mathrm{Oxide\,(s)} + \mathrm{Carbon\,(s)} \longrightarrow \mathrm{Carbide\,(s)} + \mathrm{CO\,(g)} \tag{3.2.1}$$

In such carbothermal reduction process, from two solid materials (oxide and carbon) one solid and one gaseous (carbide and CO, respectively) reaction products are formed. Therefore the formation possibilities of the new solid are two:

1. The new solid phase derives from a precursor that is one of the two starting solids;

2. The new solid phase is formed from two intermediate gas products.

The mass transport mechanisms play a fundamental role in these reactions and they can occur in one of the following ways to allow the reaction products formation [11]:

- Oxide reduction by CO with regeneration of CO from the resulting CO_2 and solid carbon.

$$2\,\mathrm{CO} \longleftrightarrow \mathrm{C} + \mathrm{CO_2} \tag{3.2.2}$$

  The mass transport of carbon to oxide particle occurs thanks to the CO/CO_2 gas couple. In this case, the oxide acts as precursor for the carbide particle.

- The formation of gaseous oxide intermediates (the carbon particle is the precursor for the carbide particle in this case), or the formation of the solid reaction product in the gas phase by reaction with CO;
- The oxide reacts with carbon by solid state reaction causing the CO formation which appears as a gaseous reaction product without any mass transfer function.

It was experimentally observed that the carbothermal reduction of ZrO_2, which is shown in the Equation 3.2.3, occurs in three steps. [11]

$$ZrO_2 + 3\,C \longrightarrow ZrC + 2\,CO \tag{3.2.3}$$

1. The reaction begins with CO formation from the solid state reactions of oxide and carbon particles. It acts as reducing agent leading to ZrO_{2-x} formation, so there is no incorporation of carbon into the oxide particles yet, and CO is regenerated by the aforementioned reaction 3.2.2;
2. The ZrO_{2-x} transforms in superstoichiometric cubic ZrC_xO_y phase, since CO continues its action as reducing agent and disproportionate at the surface, which is rich in lattice defects and it accommodates the incorporation of carbon into the crystal lattice. The reaction rates of oxygen loss (ν_a) and carbon incorporation (ν_b) are not equal, consequently, the intermediate oxycarbide is superstoichiometric;
3. Thanks to the same mass transfer mechanisms realized in the previous step, the oxygen is substituted by carbon in ZrC_xO_y.

Another mechanism was proposed after transmission electron microscope (TEM) studies on powders [30]. The reaction begins with the destabilization of carbon and zirconia, with oxidation of carbon leading to gaseous CO formation and the removal of oxygen from zirconia giving a ZrO_{2-x} phase. The destabilization of zirconia continues until a layer of Zr exist on a underlying Zr-O phase, which can then exist as gaseous Zr and ZrO. Nucleation and growth of the oxycarbide occur inside the carbon agglomerates, which may arise from condensation of ZrO and CO followed by solid state diffusion to ZrC_xO_y. Finally the oxycarbide is further reduced by CO forming the carbide. The mechanisms is represented in Figure 3.16.

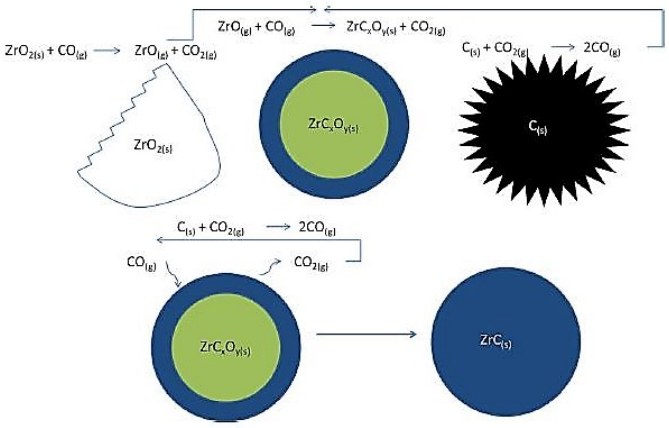

Figure 3.16: Schematic representation of the second purposed method of ZrC production by carbothermal reduction of ZrO_2.[30]

3.3 ZrGe as a new non-fissile material

Molten germanium targets were tested at ISOLDE, but a solid refractory germanium-containing target has never been developed, apart from very preliminary investigations using Hf_5Ge_3 and Zr_5Ge_3[32]. The properties of germanium intermetallic compounds indicate that they are favorable for use in on-line mass-separators, so they were considered as potential targets in this work.
The phase diagram of Zr-Ge system (see Figure 3.17) contains five intermetallic compounds (Zr_3Ge, Zr_5Ge_3,Zr_5Ge_4, ZrGe and Zr_2Ge [58]. The phases characterized by the highest melting point are Zr_5Ge_4 and ZrGe which melt at about 2500 K (the other phases at less than 2000 K present liquid), thus they can sustain the high-temperature requirement of an ISOL target.

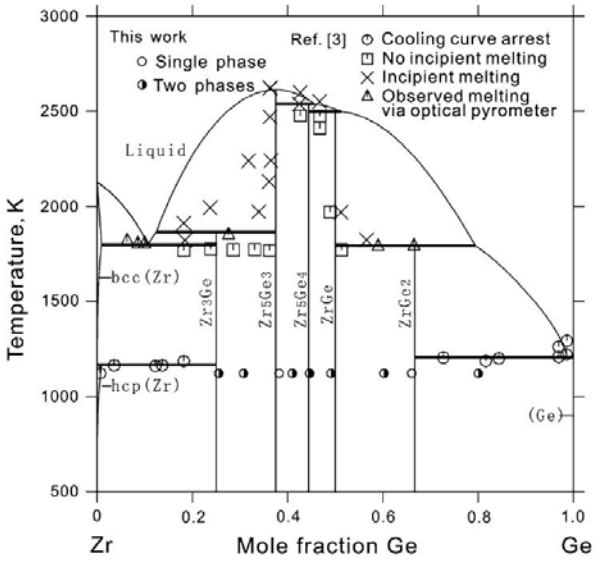

Figure 3.17: Zr-Ge system phase diagram.[58]

ZrGe has a Primitive orthorhombic FeB-type (Pearson symbol: oP8) structure which is shown in Figure 3.18, while Zr_5Ge_4 has a primitive tetragonal[58].

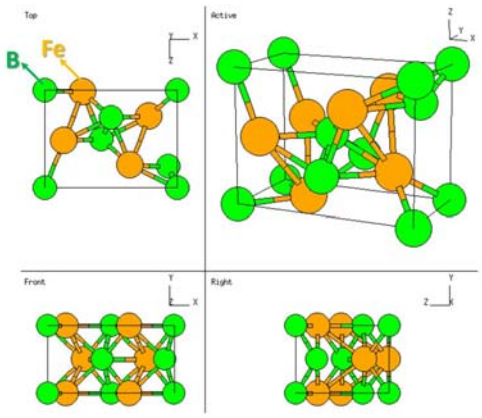

Figure 3.18: ZrGe structure, FeB-type (Pearson symbol: oP8).[42]

In particular ZrGe find applications in electronics, for instance as Schottky source/drain (S/D) contacts fabricated on n-Ge substrates by using direct sputter deposition of Zr or for fabricating heterojunction bipolar transistor [66]. If used as a SPES target, it would be able to produce and release isotopes reported in Figure 3.19.

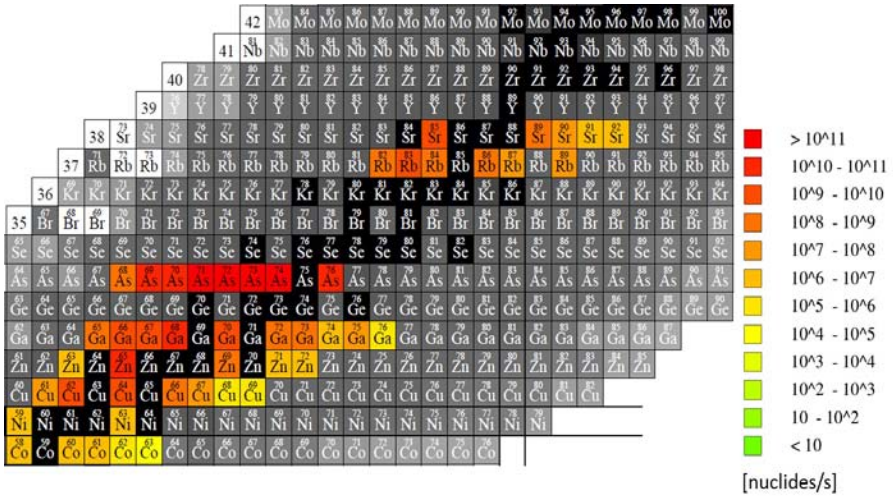

Figure 3.19: Isotopes production from ZrGe target provided by the FLUKA simulation. Primary proton beam energy= 40 MeV, current= 200 μA, working temperature=1800 °C.

The zirconium germanides chemical resistance is not comparable with the carbides presented in the previous section: they are dissolved by solfuric acid, hydrochloric, nitric acid (Zr_3Ge is an exception, indeed it remains practically unchanged), and acqua regia, but in organic (acetic, oxalic, and citric) acids and in water, they are stable. [56]
In literature three different methods to synthesize the zirconium germanide were briefly described [51, 15]:

1. **Synthesis from simple substances.** This is one of the basic methods of producing germanides. It consists either in sintering a mixture of germanium and metal powders in argon or vacuum at comparatively low temperatures or in melting such a mixture in an electric arc or induction furnace provided with an inert gas (argon or helium) atmosphere. The overall reaction is:

$$\mathrm{mMe} + \mathrm{nGe} \longrightarrow \mathrm{Me}_m\mathrm{Ge}_n \tag{3.3.1}$$

2. **The germanothermic reduction.** It consists in the vacuum-thermic reduction of transition metal oxides by germanium, which yields germanide phases of comparatively high purity;

3. **The Zirconium hydride method.** The specimens can be prepared heating under vacuum powders of zirconium hydride and germanium.

3.4 Conclusions

In this chapter the different materials that can satisfy the target requirements were analyzed. In particular uranium carbide, indicated as UC_x to indicate the graphite excess which improves the release properties, was the first material successfully tested as a target at HRIBF giving important experimental results fulfilling expectations: it provided with an acceptable release yield a large number of isotopes that can be used for applications discussed in Chapter 1.
The main problem of UC_x is that it is a fissile material: its handling and production need several safety measures due to radiations that it naturally produces. Therefore the development of new non-fissile materials, i.e. they generate isotopes by other reactions, will simplify the operations at the SPES facility.
This thesis work is focused on the production and characterization of new target concepts made of titanium carbide, zirconium carbide and zirconium germanide. The titanium and zirconium carbide have similar properties and production routes as explained in Paragraphs 3.2.3 and 3.2.2: in literature a lot of information concerning these two materials can be found because of their industrial relevance for extreme applications.
Zirconium germanide is considered as a potential target material for the production of ^{64}Cu and ^{67}Cu which are isotopes of medical interest hard to produce with other materials. It does not find many industrial applications such as carbides, consequently the literature is really poor of information. However three ZrGe synthesis methods and properties related to the Zr-Ge phase diagram, structure, and chemical resistance were reported.

CHAPTER 4

Zirconium Carbide

The importance of zirconium carbide as a non-fissile target was discussed in the previous chapter (paragraph 3.2.3). Its synthesis through the carbothermal reduction method is already well established [23], therefore in this chapter the procedure to get a ZrC target with carbon excess (ZrC_x) aimed to improve the isotopes release will be described.
The aim is to produce 13 *mm* targets adjusting both the chemical composition and the heat treatment parameters; the information obtained from the 13 *mm* target production can be used to produce a 30 *mm* target. However, the production phases are common for both the target sizes and they are resumed in Figure 4.1.

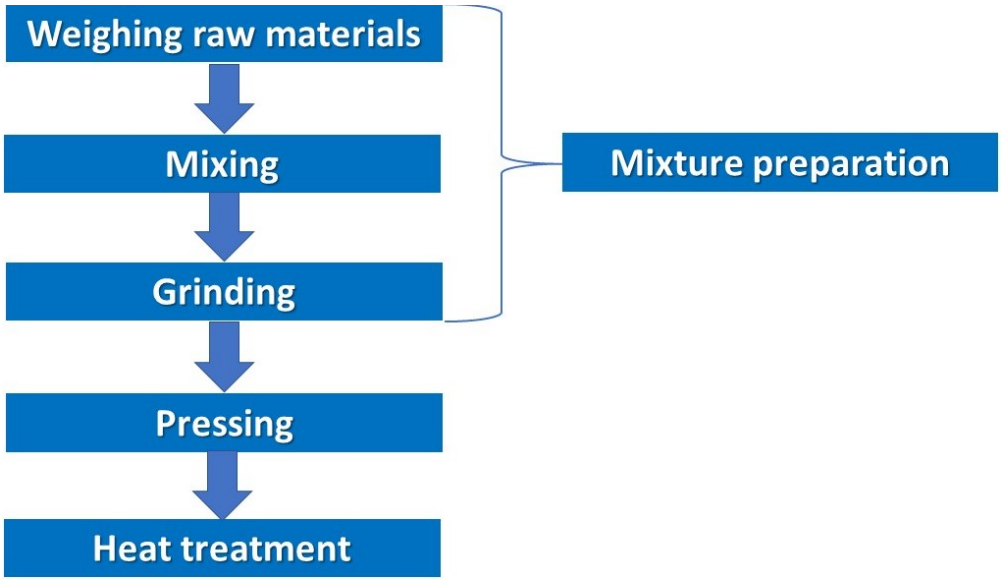

Figure 4.1: Samples production phases.

After samples production, the microstructural analysis, X-Ray Diffraction (XRD) and physisorption will be performed in order to characterize as well as possible the created material. Moreover, thanks to mass and volume measurements before and after the heat treatment, it will be possible to estimate the ZrC target porosity.

4.1 13 *mm* ZrC_x target

4.1.1 Mixture preparation and pressing

The first production step is the mixture preparation which had to be adjusted in order to obtain mechanically stable and safely manageable green pellets. They were indeed characterized by a low mechanical resistance that caused their rupture when extracted from the mold. Therefore it was necessary to add a binder to the powder mixture, such as phenolic resin: thanks to the cross-linking action of phenolic resin, the mechanical resistance of samples improved. Thus the following chemicals are manually minced and mixed together by means of the mortar in Figure 4.2(d):

- Zirconium(IV) oxide: Sigma-Aldrich (99% trace metals basis) particle size 5 μm;
- Graphite : Sigma-Aldrich (99,9%) , powder mean grainsize < 45 μ;
- Phenolic resin: in the form of a 10 wt.% solution in acetone.

Different mixture compositions reported in Table 4.1 were prepared to find the one that provides, after pressing, the highest mechanical resistance of the green pellet for its handling with the minimum amount of phenolic resin. Indeed if the quantity of phenolic resin increased, gas developed during the heat treatment due to phenolic resin decomposition increased as well, leading to bubbles formation inside the specimen.
The mass of powders necessary to produce a 13 *mm* target, about 1 *mm* thick is 400 *mg*. Obviously ZrO_2 and C quantities to realize the carbothermal reduction were calculated taking into account even the carbon excess:

$$ZrO_2 + 5\,C \longrightarrow ZrC + 2\,C + 2\,CO \tag{4.1.1}$$

After the powders preparation, they were placed in a 13 mm diameter mold (see Figure 4.2(a) and 4.2(b)) and subsequently cold pressed in a uniaxial hydraulic manual press (see Figure 4.2(c)) at 750 MPa (maximum allowed pressure) for 1 hour.

Table 4.1: Different mixture compositions used to produce 13 *mm* targets.

Sample	wt.% ZrO_2	wt.% C	wt.% Phenolic resin
1	66	32	2
2	64,7	31,4	3,9
3	64,7	31,4	3,9
4	64,1	31,1	4,8

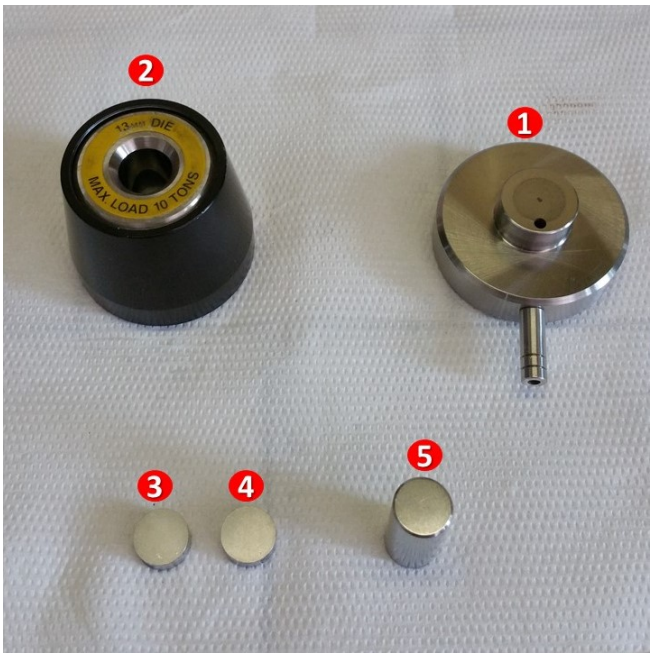

(a) Mold parts mounting order: 2 placed over 1; 3, powders, 4 respectively inserted inside 2; 5 over 4 to transmit the pressure.

(b) Mounted mold.

(c) Manual hydraulic press.

(d) Mortar used to grind and mix the raw materials.

Figure 4.2: Samples preparation apparatus.

Samples 1,2,3 were broken during the extraction from the die, while sample 4 containing about the5 wt.% of phenolic resin in Figure 4.3 survived both to extraction and to measurements (mass $= 408\ mg$, diameter$= 13,1\ mm$, thickness $= 1,15\ mm$). However, several other specimens were realized with the same composition of sample 4 and none of them broke, thus it was chosen to realize the ZrC_x targets with a minimum amount of phenolic resin of 5 wt.%.

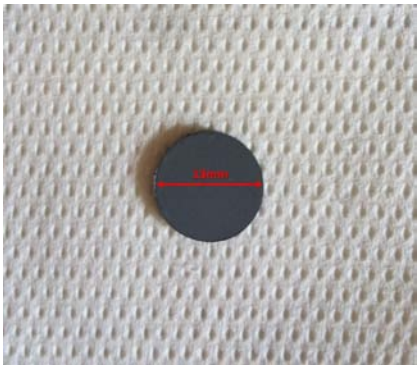

Figure 4.3: Sample 4 contains about 5 wt.% of phenolic resin.

4.1.2 Heating system

The thermal treatment of the produced pellets was performed under high vacuum ($10^{-5} \div 10^{-6}\ mBar$) in a furnace entirely designed and developed at LNL, which is shown in Figure 4.4 [23, 24].

Figure 4.4: Furnace used to proceed the heat treatments and its main components.

It consisted of a water cooled stainless steel chamber evacuated by means of a rotary and a turbomolecular pump placed in series (see Figure 4.5): the latter pump activated when the pressure inside the chamber reached 10^{-2} $mBar$ thanks to the rotary pump. The process was typically monitored by means of a penning trap which measured pressure inside the chamber (in the $10^{-3} \div 10^{-7}$ $mBar$ range) and by a Quadrupole Mass Spectrometer that gave information about gas formed during the thermal treatment.

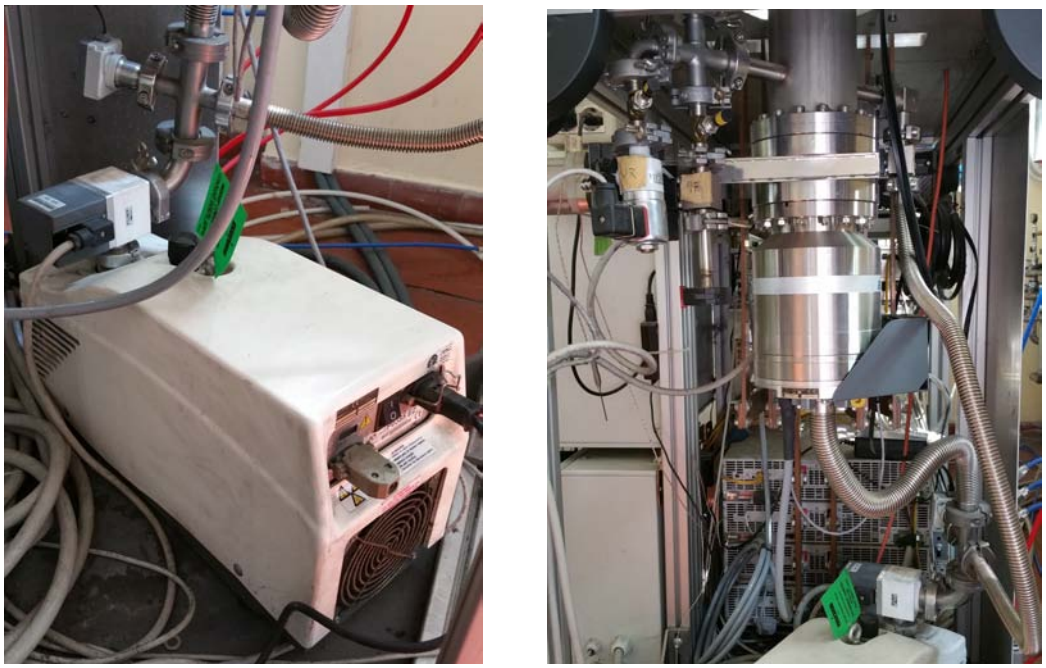

(a) rotary pump. (b) Turbomolecular pump.

Figure 4.5: Rotary and turbomolecular pumps connected in series.

A tantalum cylindrical hollow heater placed inside the chamber was heated by Joule effect by means of a power supply system connected to copper clamps capable of providing currents up to 1300 A, with a maximum potential difference of 10 V. The internal part of the heater is covered by a graphite jacket (shaped as a cylindrical hollow tube) in which a graphite plate that needed to sustain samples to treat both the heater sides were then closed by means of two graphite bulk disks which acted as heat shields and allowed a good temperature homogeneity inside the heater. One of the graphite caps has a 5 mm diameter hole through which the temperature of the first thermal treated sample can be measured by means of a pyrometer, that can be pointed towards the sample thanks to a Kodial glass window that shielded the heat coming from the furnace.
The tantalum heater is itself shielded by means of a complex system made of curved tantalum foils, in order to reach temperatures up to 2000 °C inside the reaction box.
The labVIEW software controlled directly the power supply adjusting the current and voltage as desired by the user which can decide the heating rate, the dwell time and the cooling rate; in particular, the empirical relation between the supplied current and the temperature inside the

chamber was determined fitting data given by the labVIEW interface which allowed to read online the furnished power, the pressure inside the chamber, and the temperature measured by the pyrometer. Finally the obtained data from the heat treatment provided by both the spectrometer and the penning trap were collected by a SD card.
This furnace was used to perform all the heat treatments executed in this work, unfortunately the mass spectrometer useful to measure the composition of the developed gas during the heating cycle was not in function.

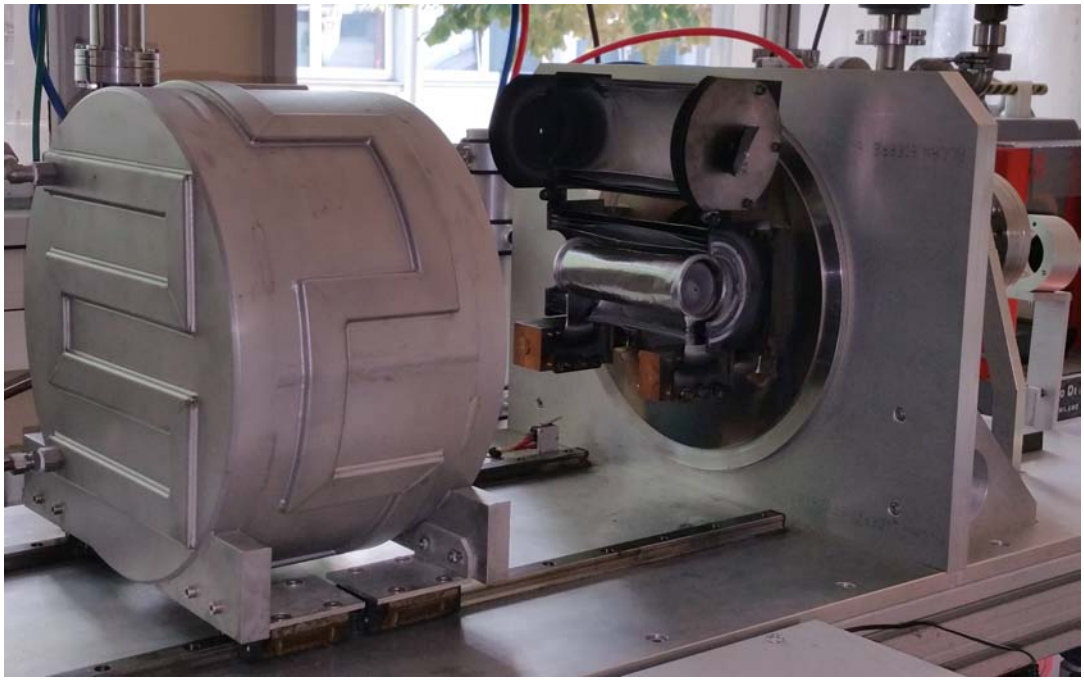

(a) The vacuum chamber contains the tantalum heater.

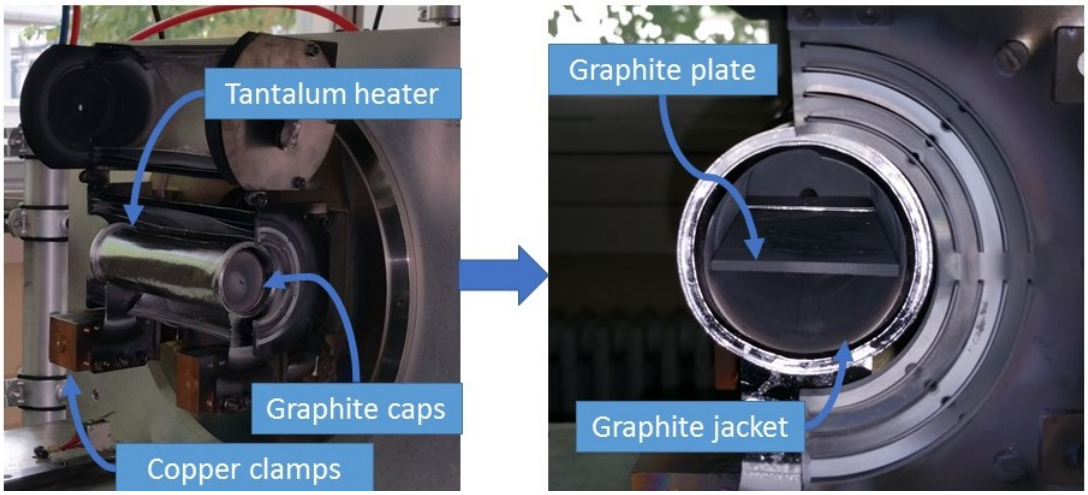

(b) The tantalum heater and its components.

Figure 4.6: Heating system overview.

4.1.3 Heat treatment 1

The thermal treatment was carefully designed in order to make the reaction (4.1.1) occur by removing CO from the reaction chamber, without reaching pressure values that could compromise the functioning of the pumping system, and at the same time favor the consolidation of the green pellets by sintering. Thus the first heat treatment developed for ZrC_x targets consisted of three phases as shown graphically in Figure 4.7:

1. Slow heating (100 °C/h) up to 1500 °C, dwell time of 4 hours at 1500 °C, to promote and possibly complete the carbothermal reaction (4.1.1) ;

2. Heating (100 °C/h) up to 1800 °C, dwell time of 8 hours at 1800 °C, to sinter the carburized powders.

3. Cooling to room temperature (100 °C/h).

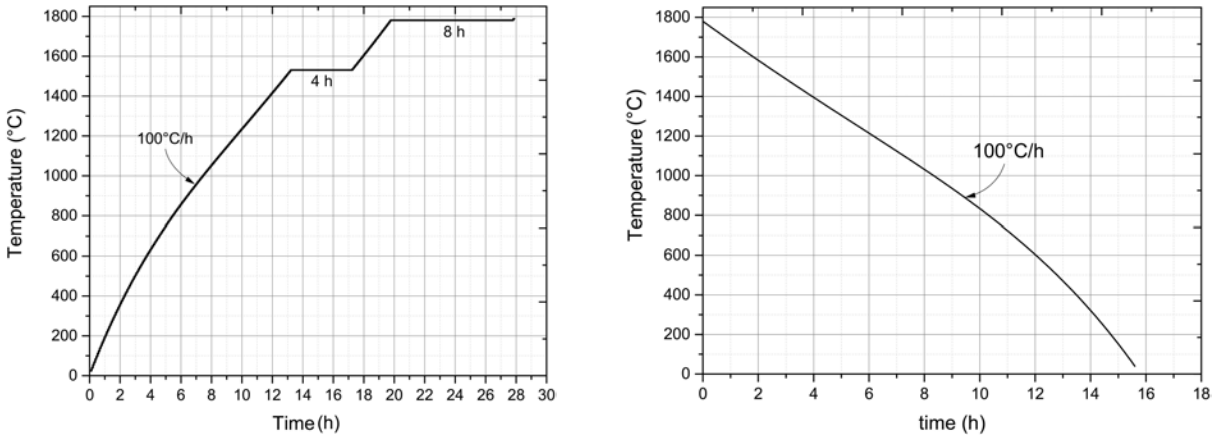

(a) Carburization ramp.

(b) Cooling ramp.

Figure 4.7: First heat treatment for 13 *mm* samples.

Figure 4.8 reports the measured pressure inside the chamber during the heat treatment [57]. A clear gas evolution was found to occur at low temperature, and it can be attributable mainly to water release, as found by mass spectrometry. Water was probably generated inside the chamber either by desorption from the precursors powders or during the cross-linking of the phenolic resin. Furthermore, a certain amount of the produced gas at low temperature can be attributed to the phenolic resin decomposition, which occurs at temperatures between 350 °C and 800 °C, as obtained by thermal gravimetric analysis [13].
For T > 1000 °C, two main peaks can be observed and they can be both attributed to the carbothermal reduction reaction , liberating CO as indicated by (4.1.1) [23]. Their position in terms of temperature corresponded to the plateaus of the heating ramp, moreover, the presence of two peaks at different

temperatures can be due to temperature gradient within the treated samples, since they were placed in contact with the graphite plate only with their bottom surfaces.

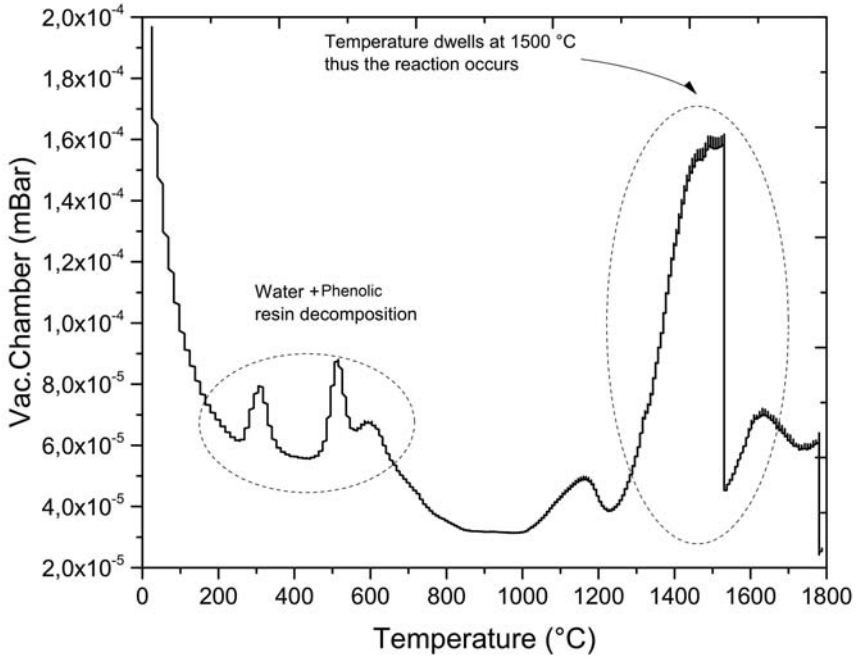

Figure 4.8: Pressure inside the reaction chamber upon carburization and sintering of ZrC_x pellets.

The treated samples are shown in Figure 4.9, they correspond to compositions of Table 4.1. Moreover, the average mass loss during the treatment reported in Table 4.2, was really close to the theoretical value. They retained their shape with respect to the initial one, in particular sample 4 was subjected to diameter reduction (from $13,1\ mm$ to $11,85\ mm$) and thickness increase (from $1,15\ mm$ to $1,29\ mm$).

Table 4.2: Samples mass lost compared with the theoretical one, which is calculated from the reaction (4.1.1)

Sample	m before treatment $[mg]$	m after treatment $[mg]$	Mass loss %	Theoretical mass loss $[mg]$
1	140	96	31,6	33,0
2	194	130	33,0	33,1
3	404	274	32,2	33,1
4	408	280	31,4	33,8

The geometrical data and the mass can be used to calculate the real density $\rho_{sample}\ [g/cm^3]$ of the sample 4:

$$\rho_{sample} = \frac{m}{V} = m \cdot \frac{4}{\pi\ d^2\ t} = 1,969\ g/cm^3 \tag{4.1.2}$$

Where $d\ [cm]$ and $t\ [cm]$ are diameter and mass of the sample, respectively; $m\ [g]$ is the final mass .

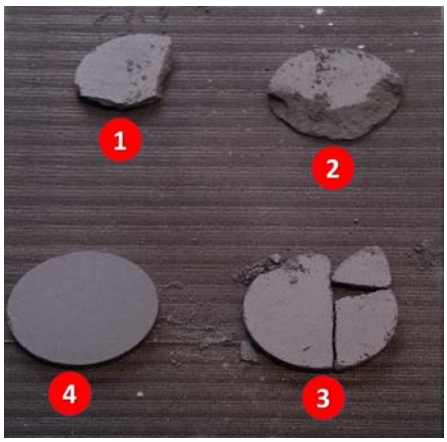

Figure 4.9: ZrC_x samples after heat treatment. The numeration is related to compositions of Table 4.1.

The theoretical density of ZrC_x, ρ_{th} $[g/cm^3]$, is calculated as follow:

$$\rho_{th} = V_{f,ZrC} \cdot \rho_{ZrC} + V_{f,C} \cdot \rho_C = 4,55\ g/cm^3 \tag{4.1.3}$$

- $V_{f,ZrC}$ and $V_{f,C}$ are the volume fraction of ZrC and C, respectively. They are calculated from the reaction (4.1.1) stoichiometry;
- $\rho_{ZrC} = 6,73\ g/cm^3$ is the ZrC density;
- $\rho_C = 1,9\ g/cm^3$ is the carbon density as obtained by the supplier datasheet.

Finally it is possible to estimate the porosity P with the following equation:

$$P = \left(1 - \frac{\rho_{sample}}{\rho_{th}}\right) \cdot 100 = 57\% \tag{4.1.4}$$

This porosity value was found even for other samples realized such as sample 4.

Samples 3 and 4 were conserved in argon, while samples 1 and 2 in air, indeed in this way, thanks to a micrograph analysis, it was possible to establish if the air exposition causes oxidation. The microstructural analysis was performed with scanning electron microscope (SEM) Tescan Vega 3xmh in Figure 4.10 which is equipped with a Secondary electron (SE) detector and a EDS system.

Secondary electrons (SEs) are low energy electrons emitted from a localized area at the uppermost layers of samples surface (within a range of a few nm depths); therefore, they provide high-resolution imaging suitable for detailed topographical characterization of samples. SEs are produced when primary electrons from the beam interact inelastically with the specimen.

The EDS (Energy Dispersive Spectroscopy) system includes a sensi-

Figure 4.10: Tescan Vega 3xmh.

tive x-ray detector, a liquid nitrogen dewar[1] for cooling, and software to collect and analyze energy spectra. An EDS detector contains a crystal that absorbs the energy of incoming x-rays by ionization, yielding free electrons in the crystal that become conductive and produce an electrical charge polarization. The x-ray absorption thus converts the energy of individual x-rays into electrical voltages of proportional size; the electrical pulses correspond to the characteristic x-rays of the element that can be identified thanks to the aforementioned software.

As shown in the following SEM images, the surface microstructures of samples maintained in argon and exposed to air were comparable: it seems there is no difference between the microstructures, which means that air exposure did not oxidize the sample surface. Nevertheless, the white regions that can be observed at MAG 3200 x in Figure 4.15 may be caused by oxide presence, indeed oxides are non-conductive, so when the specimen was directly illuminated with an electron beam, its electrons with a negative charge collected locally (specimen charge-up), thus preventing normal emission of secondary electrons; this charge-up causes some unusual phenomena such as abnormal contrast and image deformation and shift.

The oxide presence may be due to incomplete precursor (ZrO_2) transformation because of too low temperature. Obviously the EDS analysis, which will be presented later, will provide white regions composition, confirming the presence of oxide.

However, the residual graphite represented by “black foils” clearly shown in Figure 4.14, was well randomly distributed onto the sample surface as observed in Figure 4.11 (black spots). Furthermore the microstructure was characterized by the presence of numerous voids which favors the isotopes release.

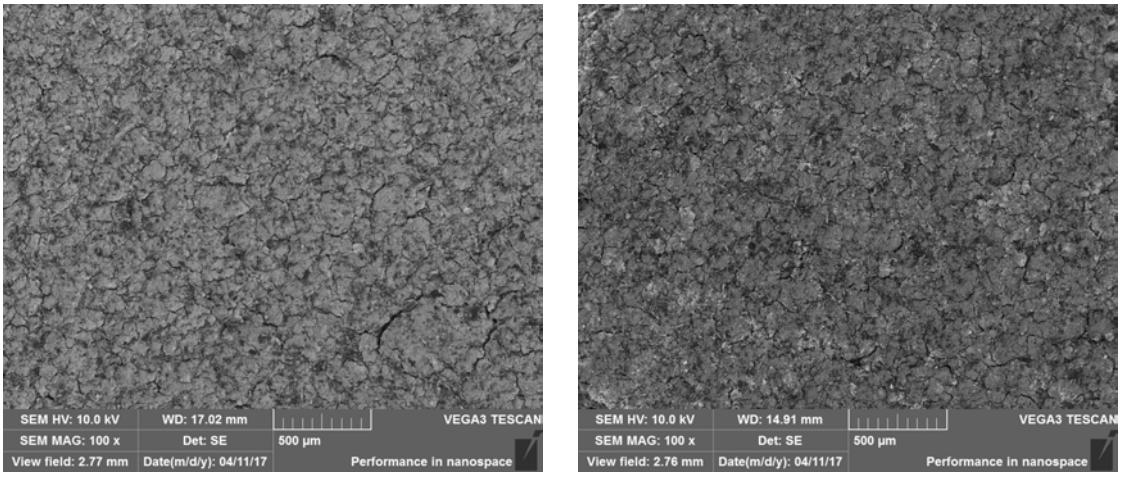

(a) Air exposure, MAG: 100 x. (b) Argon conservation, MAG: 100 x.

Figure 4.11: MAG 100 x comparison air-argon.

[1] A double-walled flask of metal or silvered glass with a vacuum between the walls, used to hold liquids at well below ambient temperature.

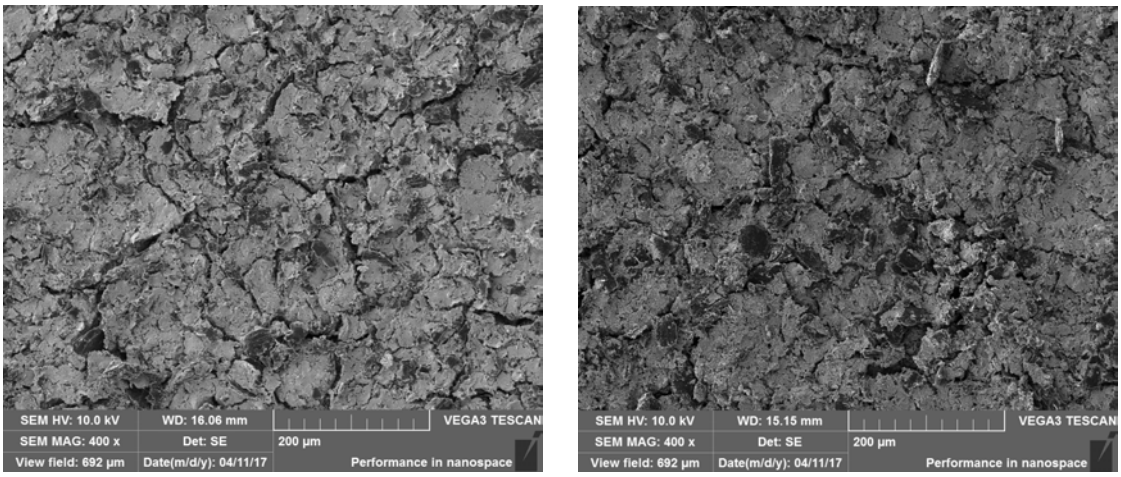

(a) Air exposure, MAG: 400 x. (b) Argon conservation, MAG: 400 x.

Figure 4.12: MAG 400 x comparison air-argon.

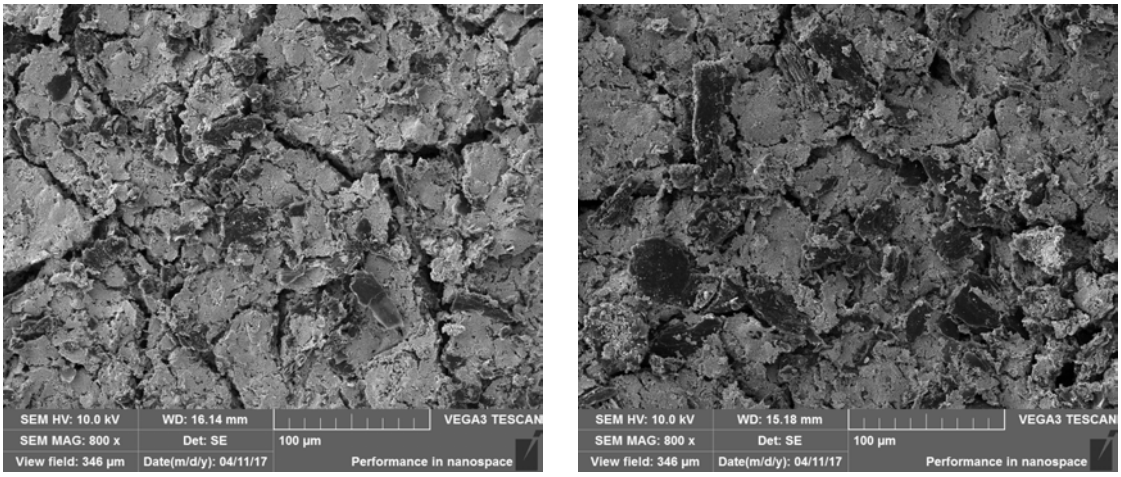

(a) Air exposure, MAG: 800 x. (b) Argon conservation, MAG: 800 x.

Figure 4.13: MAG 800 x comparison air-argon.

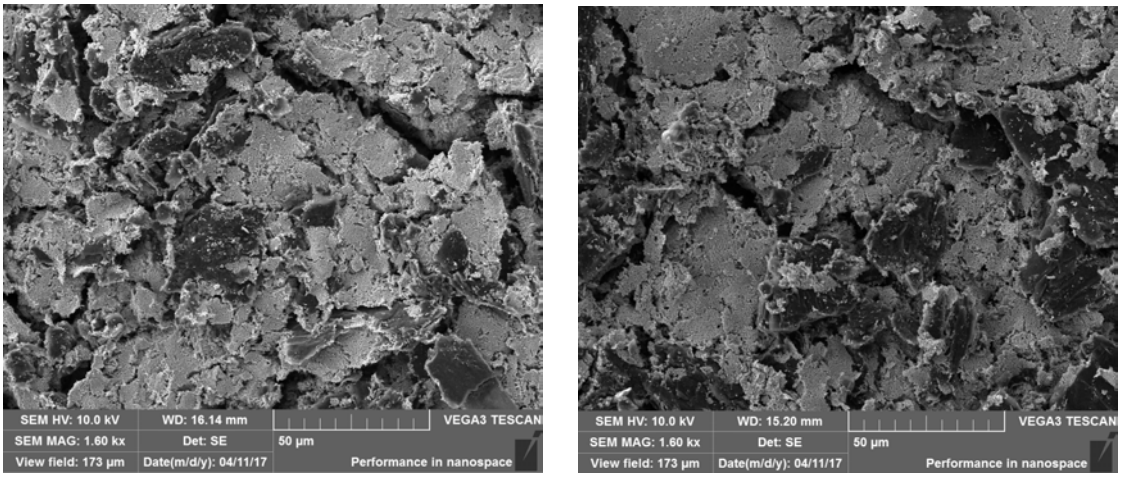

(a) Air exposure, MAG: 1600 x. (b) Argon conservation, MAG: 1600 x.

Figure 4.14: MAG 1600 x comparison air-argon.

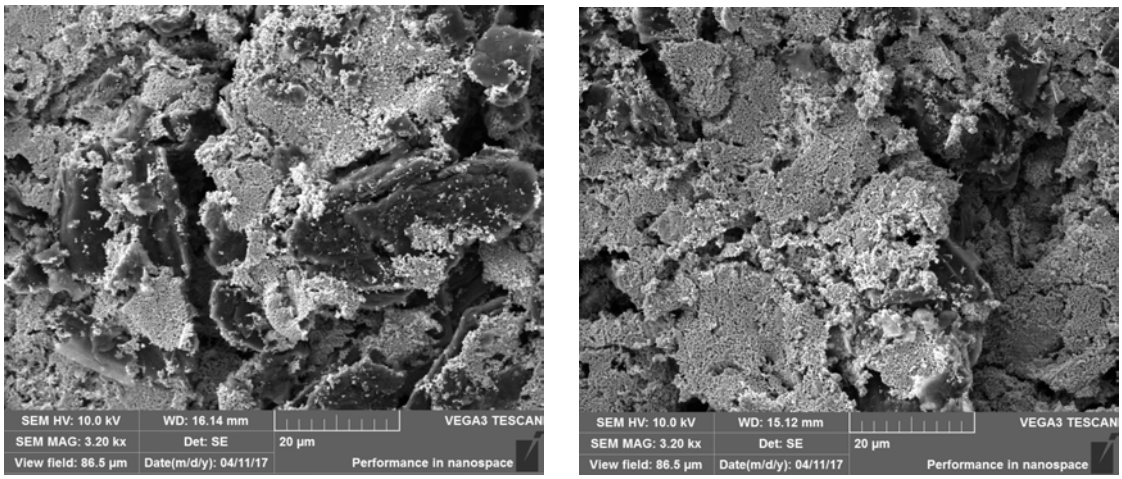

(a) Air exposure, MAG: 3200 x. (b) Argon conservation, MAG: 3200 x.

Figure 4.15: MAG 3200 x comparison air-argon.

The internal SEM micrographs (fracture section) shown in Figure 4.16 and Figure 4.17. The microstructure analysis confirmed presence of much porosity inside the sample, indeed grains complete densification clearly did not occur. However a slight sintering took place because the mechanical resistance was surely increased after the heat treatment. Moreover the microstructure was uniform through the thickness, which means that the heating and cooling rate were well designed for such a specimen thickness.

As well as the sample surface, even in this case white grains were found all over the section, so an EDS analysis was necessary to clarify the composition of these regions. In Figure 4.17 the EDS analysis revealed that the black foils were the desired residual graphite as expected, while the gray grains were characterized by the presence of both carbon and zirconium; finally the white grains were evidently affected by oxygen presence, which means that they were oxides, as presumed.

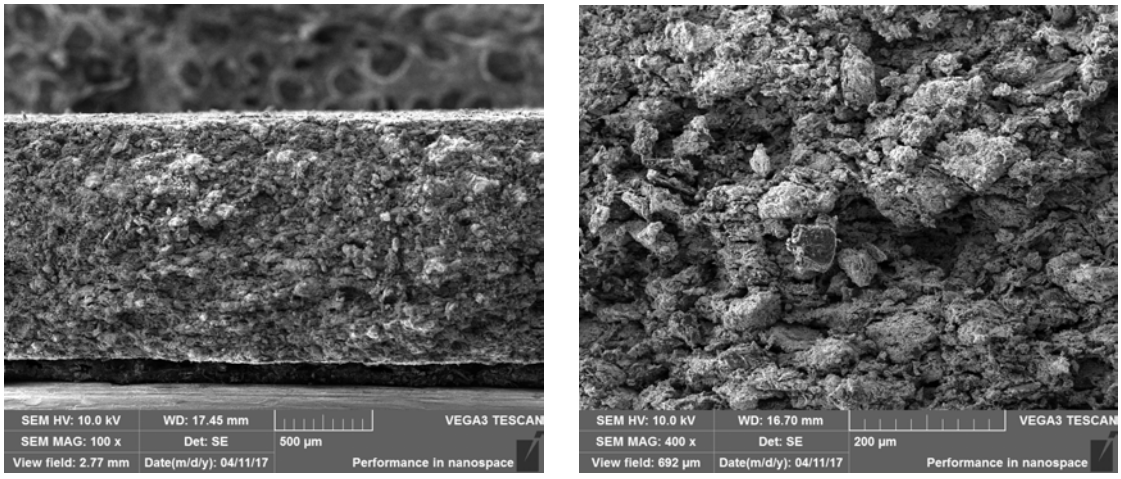

(a) ZrC internal section, MAG: 100 x. (b) ZrC internal section, MAG: 400 x.

Figure 4.16: SEM micrograph of ZrC internal section.

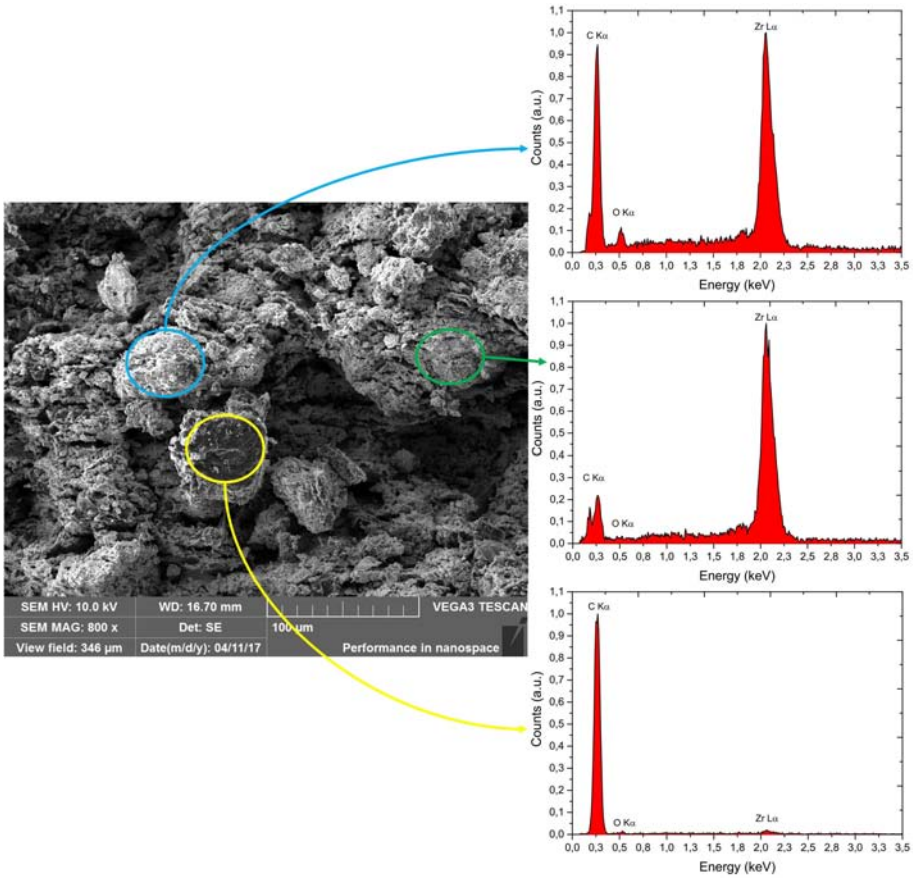

Figure 4.17: EDS reveals the composition of the white grains (blue), gray grains (green) and black foils (yellow) of the sample treated at 1800 °C. The SEM micrograph was taken at 800 x .

Therefore, the heating and cooling rates were well designed, while the maximum achieved temperature was not enough to transform all the ZrO_2 which remained as "residual" inside the material.

4.1.4 Heat treatment 2

The second heat treatment maximum is graphically represented in Figure 4.18:

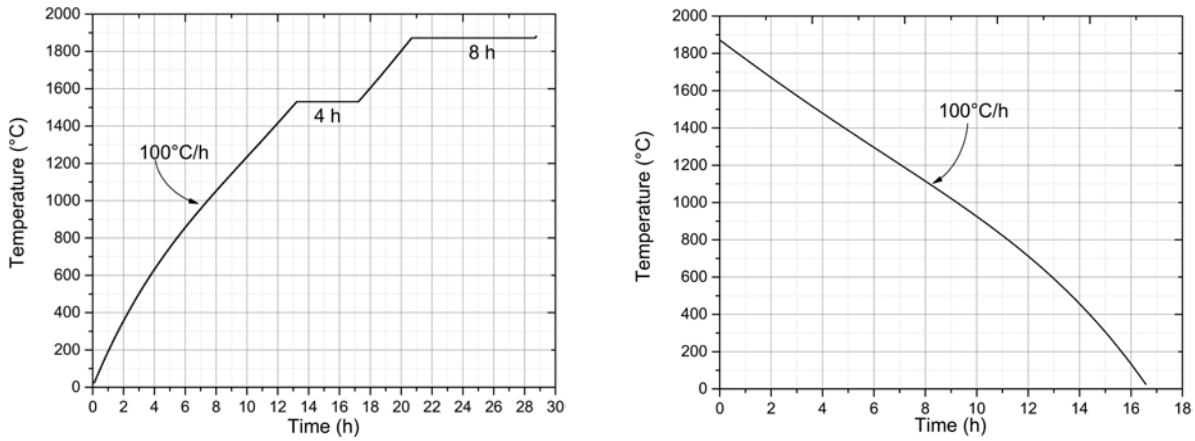

(a) Carburization ramp.

(b) Cooling ramp.

Figure 4.18: Second heat treatment for 13 *mm* samples.

The only difference with respect to heat treatment 1 is the maximum achieved temperature, which is 1900 °C. The measured pressure inside the chamber during the heat treatment in Figure 4.19 was characterized by the same peaks observed in for heat treatment 1 in Figure 4.8. However, when T>1800 °C the pressure increased because of gas release from the sample and in part from the materials that constituted the furnace internal components, thus it may be that the carbotermal reduction was completed over 1800 °C.

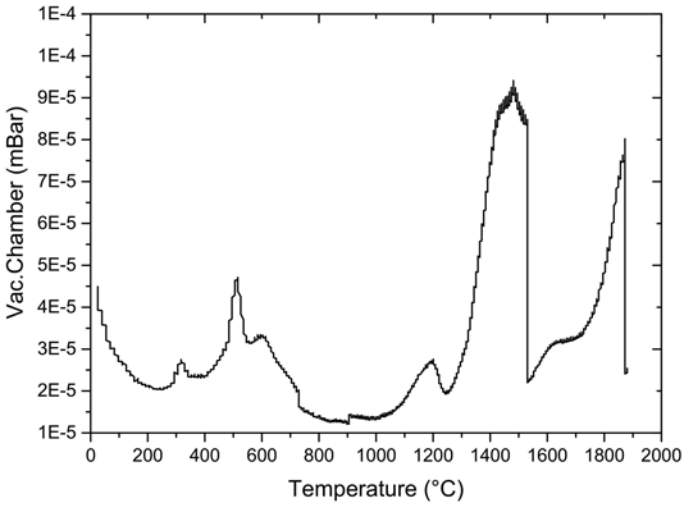

Figure 4.19: With respect to the first heat treatment, when the temperature overlaps 1800 °C the pressure inside the reaction chamber increases.

The microstructure after the heat treatment 2 did not subject significant changes from the heat treatment 1 for both surface and internal part of the sample, nevertheless a reduction of white regions occurred.; indeed, only increasing the magnifications some white grains appeared, therefore an EDS analysis remained still necessary.

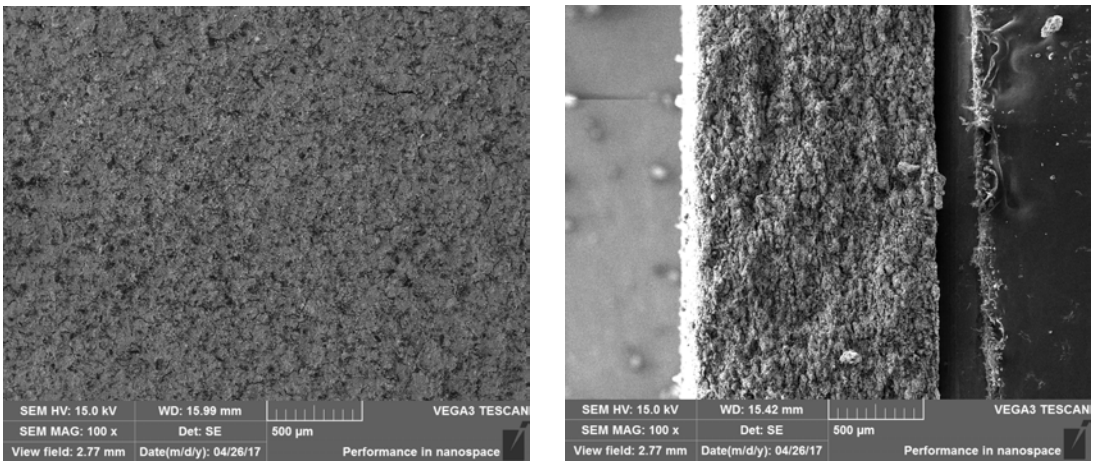

(a) Sample surface, MAG: 100 x. (b) Sample internal section, MAG: 100 x.

Figure 4.20: Internal and superficial microstructure after heat treatment 2. MAG: 100 x.

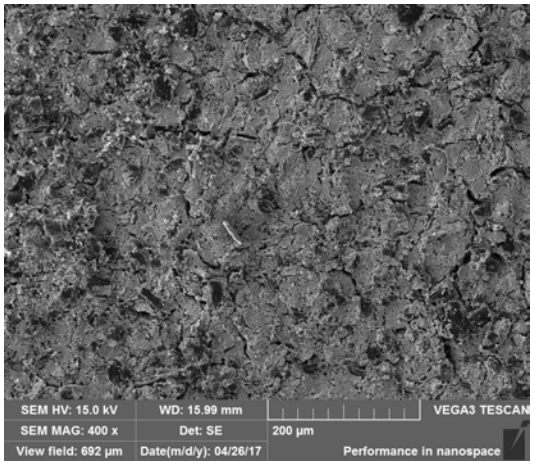

(a) Sample surface, MAG: 400 x.

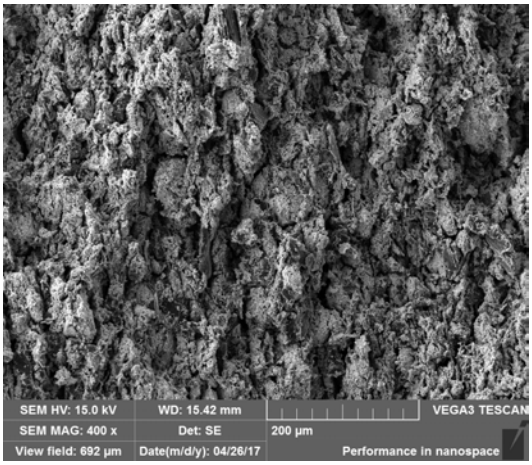

(b) Sample internal section, MAG: 400 x.

Figure 4.21: Internal and superficial microstructure after heat treatment 2. MAG: 400 x.

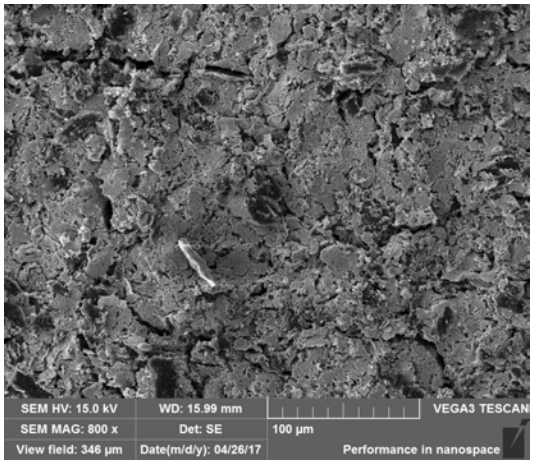

(a) Sample surface, MAG: 800 x.

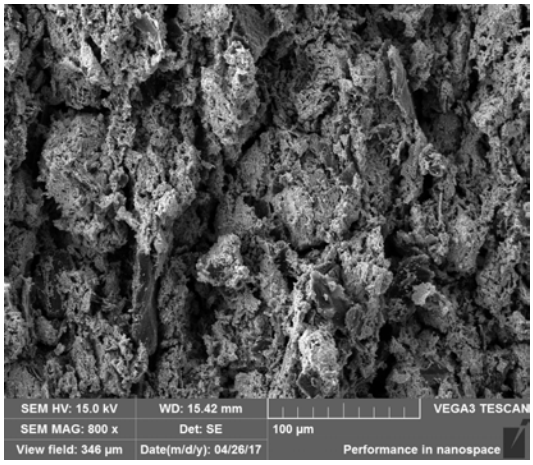

(b) Sample internal section, MAG: 800 x.

Figure 4.22: Internal and superficial microstructure after heat treatment 2. MAG: 800 x.

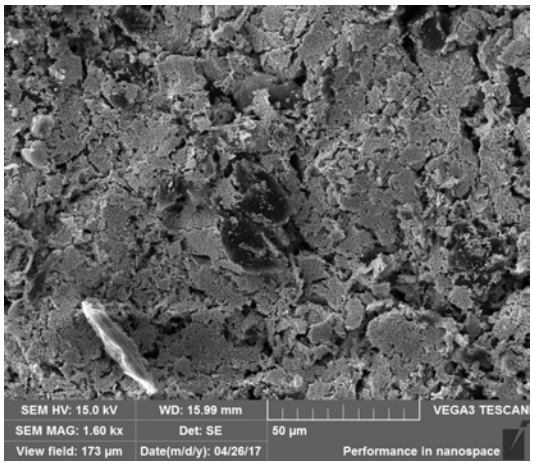

(a) Sample surface, MAG: 1600 x.

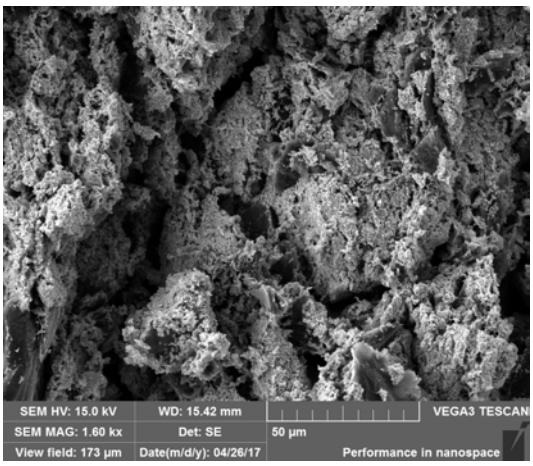

(b) Sample internal section, MAG: 1600 x.

Figure 4.23: Internal and superficial microstructure after heat treatment 2. MAG: 1600 x.

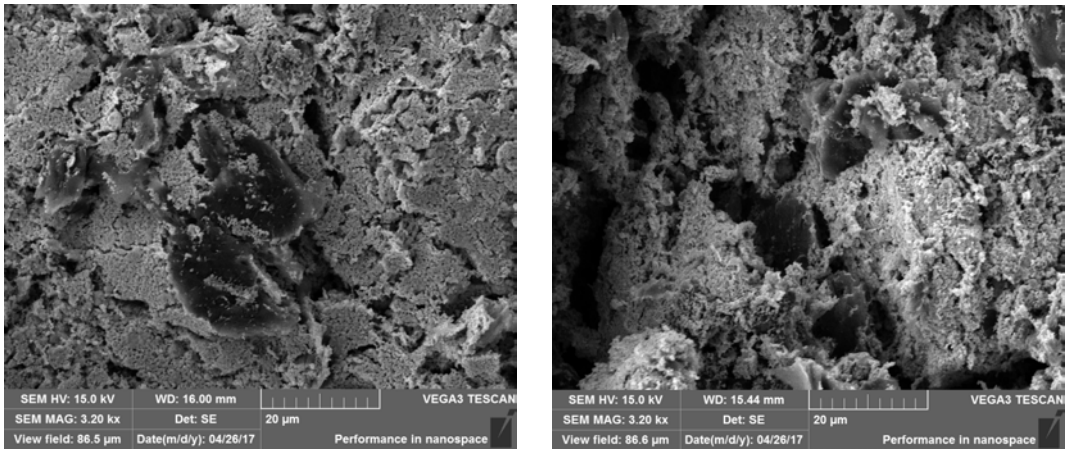

(a) Sample surface, MAG: 3200 x. (b) Sample internal section, MAG: 3200 x.

Figure 4.24: Internal and superficial microstructure after heat treatment 2. MAG: 3200 x.

EDS analysis in Figure 4.25 revealed that oxygen was not present in the white grains, which were composed by carbon and zirconium; both gray and black foils compositions were the same showed in Figure 4.17.

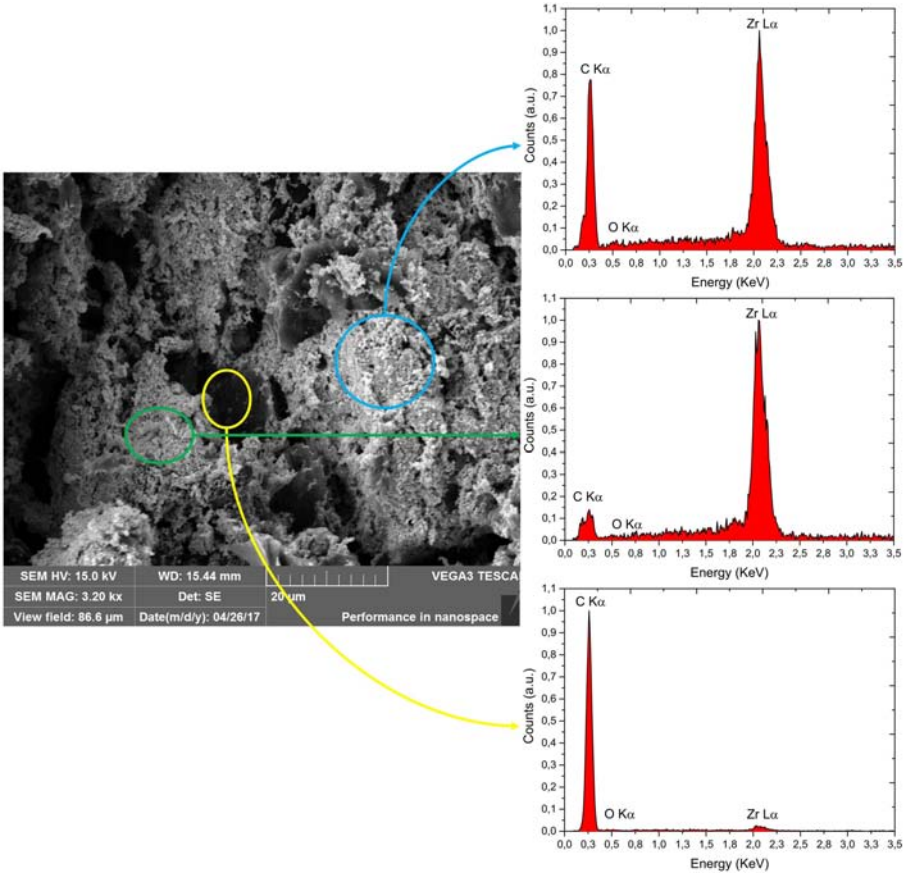

Figure 4.25: EDS reveals the composition of the white grains (blue), gray grains (green) and black foils (yellow) of the sample treated at 1800 °C. The SEM micrograph was taken at 3200 x .

4.2 30 mm ZrC_x target

The information concerning mixture composition and heat treatment parameters obtained from preparation of a 13 mm ZrC_x targets allowed the preparation of a 30 mm discs. However some changes regarding mixture preparation, mold and heat treatment were necessary to produce the new bigger target, thus they will be explained in the following paragraphs.

4.2.1 Mixture preparation and pressing

The composition used to prepare the new pellets was the one that provided the best results for the 13 mm target:

- ZrO_2= 64, 1 wt.%
- C= 31, 1 wt.%
- Phenolic resin= 4, 8 wt.%

The mass of precursors (ZrO_2 and graphite) necessary to an obtain a target of 30 mm diameter and about 1, 3 mm thick was about 2 g, consequently precursors were mixed thanks to the planetary ball mill showed in Figure 4.26 which ensured a very good homogenization.

Grinding jar components.

Grinding jar closed.

Planetary ball mill.

Figure 4.26: Planetary ball mill apparatus.

Powder was inserted with mixing balls inside the grinding jar[2], which was fixed into the planetary ball mill (Retsch, PM100) that provide the highest degree of fineness in short grinding times; the grinding jar rotated within the planetary ball mill for 40 minutes (20 minutes counterclockwise, 20 minutes clockwise) at 450 rpm, then the mixed powder was extracted and weighted.
In order to get a disc 30 mm wide and about $1,3$ mm thick, it was necessary to weight 2 g of mixed reagents and put them inside the mold in Figure 4.27(a) where they were pressed at 700 MPa (maximum mold capability charge) thanks to an automatic hydraulic press in Figure 4.27(c); furthermore, some calcium stearate was distributed onto the mold walls in order to decrease its friction with the pellet to avoid cracks into the specimen.

(a) 30 mm mold.

(b) Mold components.

(c) Automatic hydraulic press.

Figure 4.27: Pressing apparatus for 30 mm pellets realization.

[2]The number of balls to insert inside the grinding jar was obtained by the following relation: $m_{balls} = 6 \cdot m_{powder}$.

Even for 30 *mm* pellets, such a powder composition allowed the formation of a compact disc which can be handled and measured after pressing as shown in Figure 4.28.

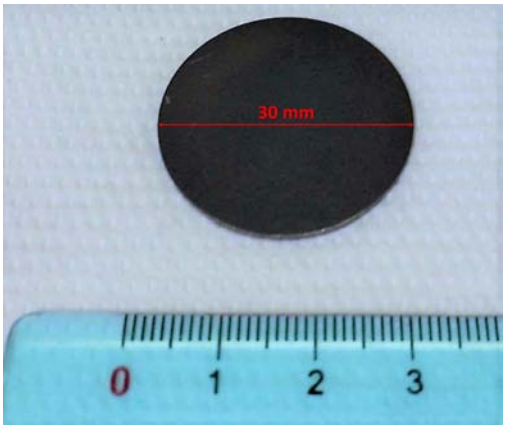

Figure 4.28: 30 *mm* pellet containing about 5 wt.% phenolic resin.

4.2.2 Heat treatment 3

The first heat treatment performed on 30 *mm* pellet is the same described in Paragraph 4.1.4 and graphically represented by Figure 4.18:

1. Slow heating (100 °C/h) up to 1500 °C, dwell time of 4 hours at 1500 °C, to promote and possibly complete the carbothermal reaction (4.1.1) ;

2. Heating (100 °C/min) up to 1900 °C, dwell time of 8 hours at 1900 °C, to sinter the carburized powders.

3. Cooling to room temperature (100 °C/h).

After heat treatment, specimens presented some bubbles onto their surface that were probably due to a massive gas release from samples as shown in Figure 4.29

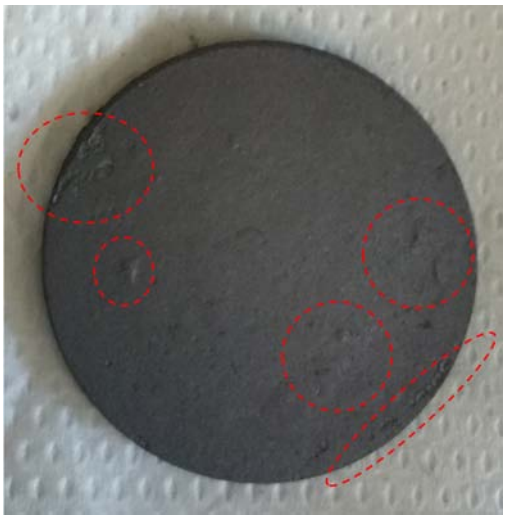

Figure 4.29: First heat treated 30 *mm* sample. Bubbles resulting from the heat treatment are the red-circled ones.

SEM analysis in Figure 4.30 shows the defective region toward sample boundary that were reacted with calcium stearate causing some flat dense areas, therefore calcium stearate was not anymore used for the following pellets production.

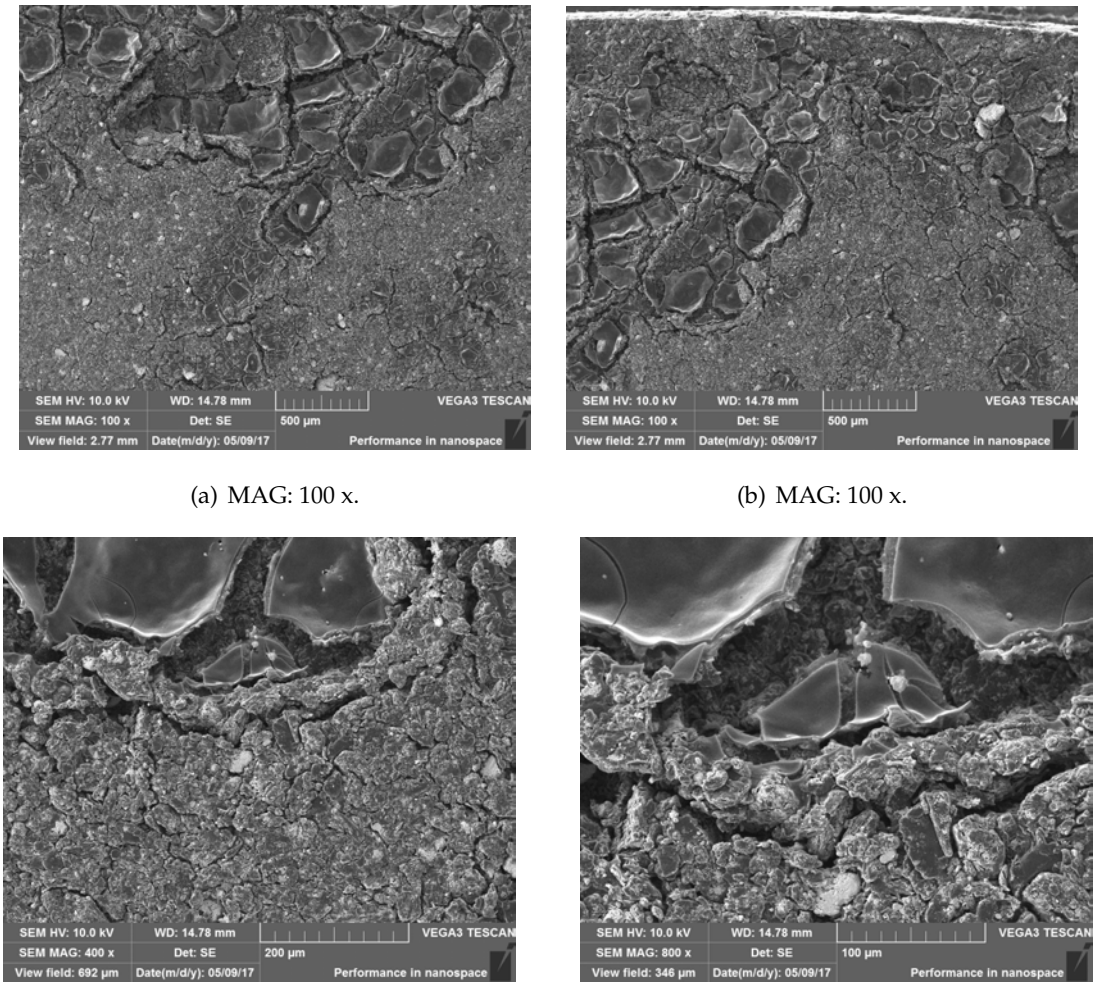

(a) MAG: 100 x.

(b) MAG: 100 x.

(c) MAG: 400 x.

(d) MAG: 800 x.

Figure 4.30: Sample regions placed on its boundary effected by calcium stearate reaction.

SEM micrographs extracted from the sample core present a non-uniform microstructure really different with respect to the one observed in 13 *mm* discs, in particular it was characterized by presence of several aggregates in both surface and internal parts of the specimen.
Large white grains were distributed through the whole specimen, indeed it may be that the reaction did not complete causing some residual ZrO_2; EDS analysis in Figure 4.34 excluded this hypothesis, furthermore it revealed that such a white grains were composed by carbon and zirconium.
Consequently, the heat treatment maximum temperature was enough to complete the carbothermal reduction, nevertheless the heating and cooling ramps used to produce 13 *mm* samples were not suitable for 30 *mm* ones because they led to a non-uniform microstructure.

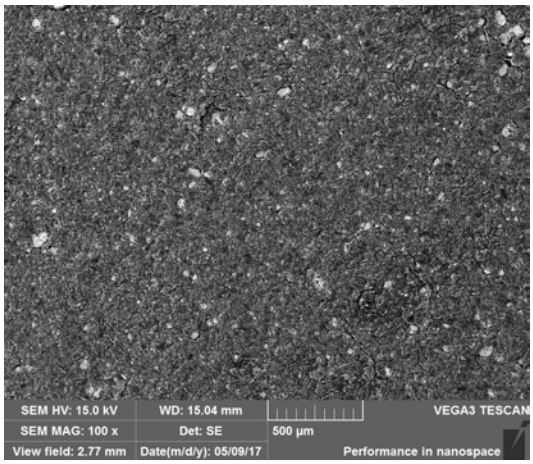

(a) Sample surface, MAG: 100 x.

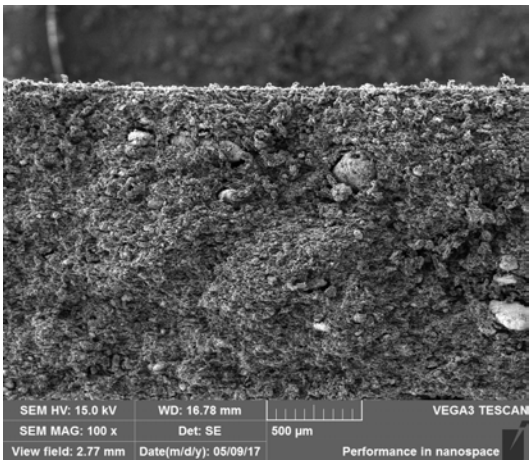

(b) Sample internal section, MAG: 100 x.

Figure 4.31: Internal and superficial microstructure after heat treatment 1. MAG: 100 x.

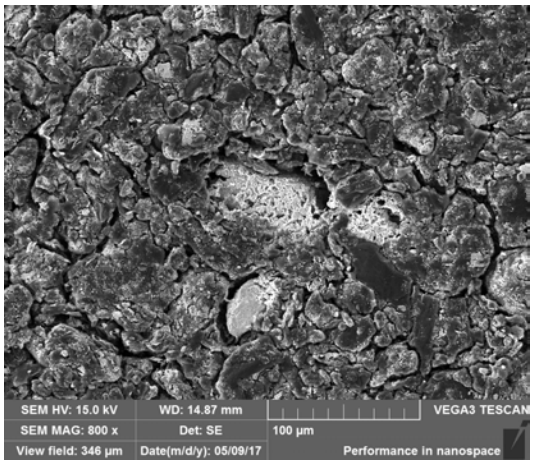

(a) Sample surface, MAG: 800 x.

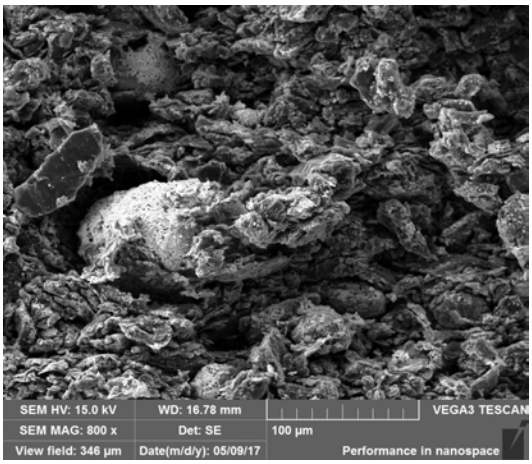

(b) Sample internal section, MAG: 800 x.

Figure 4.32: Internal and superficial microstructure after heat treatment 1. MAG: 800 x.

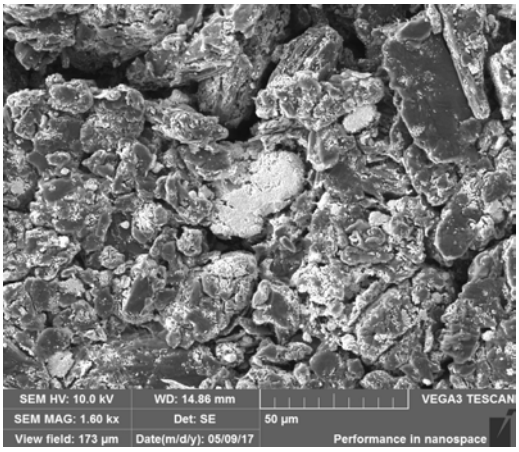

(a) Sample surface, MAG: 1600 x.

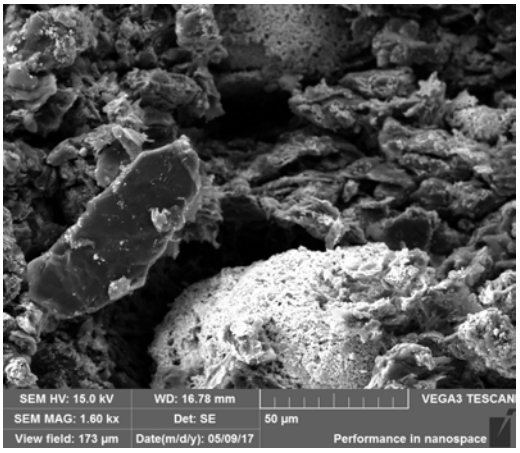

(b) Sample internal section, MAG: 1600 x.

Figure 4.33: Internal and superficial microstructure after heat treatment 1. MAG: 1600 x.

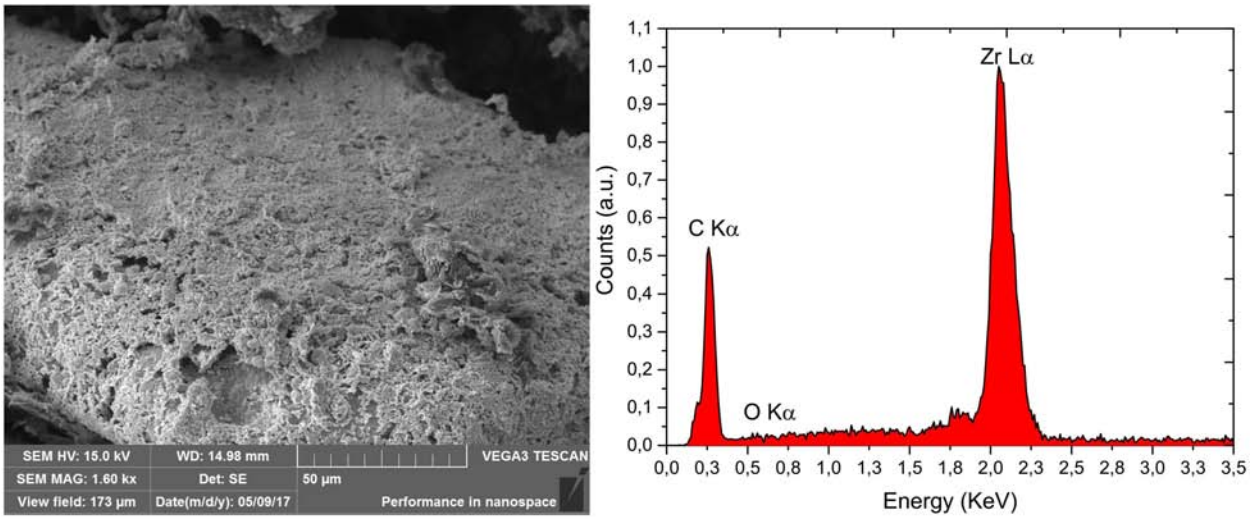

Figure 4.34: White grain EDS analysis, SEM MAG:1600 x .

With respect to 13 *mm* ZrC_x specimen, theoretically, the developed gas of a 30 *mm* sample should be about three times the former one, but observing the pressure trend inside the reaction chamber during the heat treatment in Figure 4.35, it did not occur; in fact, the pressure corresponding to phenolic resin - water decomposition at temperature interval 350 ÷ 800 °C was so much more than three times the pressure of a 13 *mm* sample. Such a phenomena may be happened because of too high heating rate which led to quick gas development from the specimen that was not capable to drain it, consequently both bubbles formation and microstructure destruction occurred.
Contrariwise, when T>1000 °C the developed gas due to CO formation resulting from carbothermal reduction was not enough as expected: even in this case, if heat treatment occurred too quickly, the material did not have enough time to homogenize its microstructure, consequently it resulted non-uniform as shown in microstructural analysis.

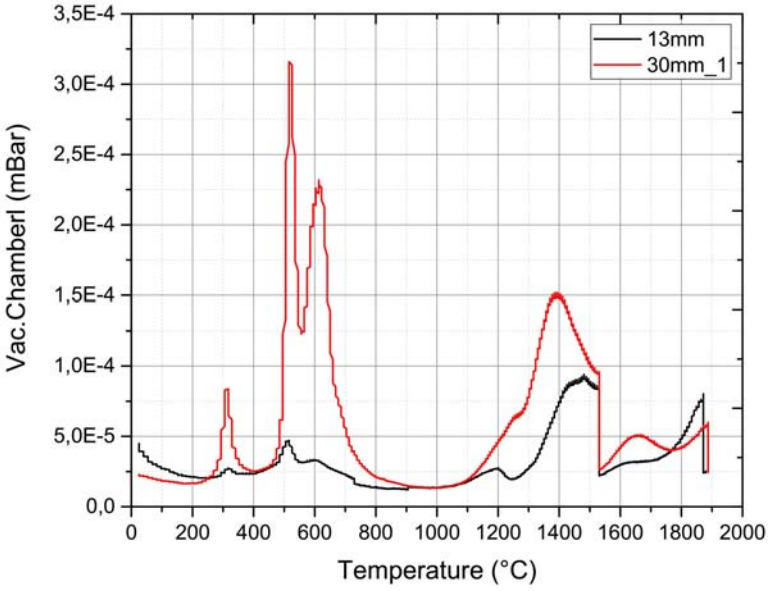

Figure 4.35: Pressure inside the reaction chamber related to first 30 *mm* heat treated sample.

The mass loss was about a half than the theoretical one (which is 33,8%), furthermore both diameter and thickness increased as reported in Figure 4.3. Even in this case the behavior of 30 *mm* samples was different from the 13 *mm* one, so this was another probe that the heat treatment must be changed in order to provide a better microstructure.

Table 4.3: Samples size (D=diameter, t= thickness) and mass (m) before treatment (b.t) and their variations after heat treatment.

Sample	m b.t. $[mg]$	Mass loss %	D b.t. $[mm]$	D increase %	t b.t. $[mm]$	t increase %
1	1957	18	30,2	5,6	1,27	25,3
2	1987	18	30,25	5,7	1,28	25,9

Porosity resulting from the heat treatment calculated using equations (4.1.2), (4.1.3), (4.1.4) and collected in Table 4.4 was larger than the 13 *mm* one because of increasing of voids inside the specimen due to an excessive gas development.

Table 4.4: Measured values after heat treatment to estimate porosity

Sample	Mass $[mg]$	Diameter $[mm]$	Thickness $[mm]$	Density $[g/cm^3]$	Porosity %
1	1608	32,00	1,7	1,777	74
2	1625	32,07	1,74	1,157	75

The heat treatment discussed in this paragraph provides a non-homogeneous microstructure characterized by dense aggregates. Moreover the average porosity value of about 74,5% reduced too much samples mechanical resistance.
Therefore, a new heat treatment must be designed to provide better mechanical and microstructural properties to the material.

4.2.3 Heat treatment 4

A maximum heating temperature of 1900 °C is necessary to complete the carbothermal reduction, moreover, to produce a 30 *mm* it is necessary to have a slow gas release employing a low heating rate, which is even helpful to uniform the final microstructure. A new heat treatment called Heat treatment 4 was designed as follow:

1. Slow heating (50 °C/h) up to 1500 °C, dwell time of 4 hours at 1500 °C, to promote and possibly complete the carbothermal reaction (4.1.1) ;

2. Heating (50 °C/min) up to 1900 °C, dwell time of 8 hours at 1900 °C, to sinter the carburized powders.

3. Cooling to room temperature (100 °C/h).

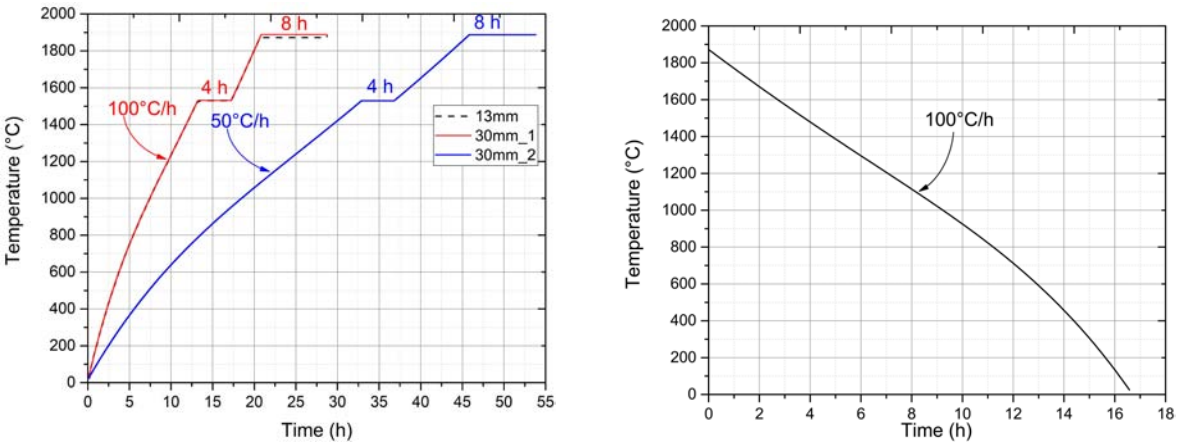

(a) Carburization ramp.

(b) Cooling ramp.

Figure 4.36: Comparison between heat treatments. The heating rate of new heat treatment (30 *mm*_2) is a half of the one described in paragraph 4.2.2 (30 *mm*_1) which is the same used to produce 13 *mm* ZrC_x targets.

The reaction chamber pressure measurement during Heat treatment 4 is represented in Figure 4.37 in which the differences with the other heat treatments (Heat treatment 2 of 13 *mm* sample and Heat treatment 3 of 30 *mm* sample) can be observed.

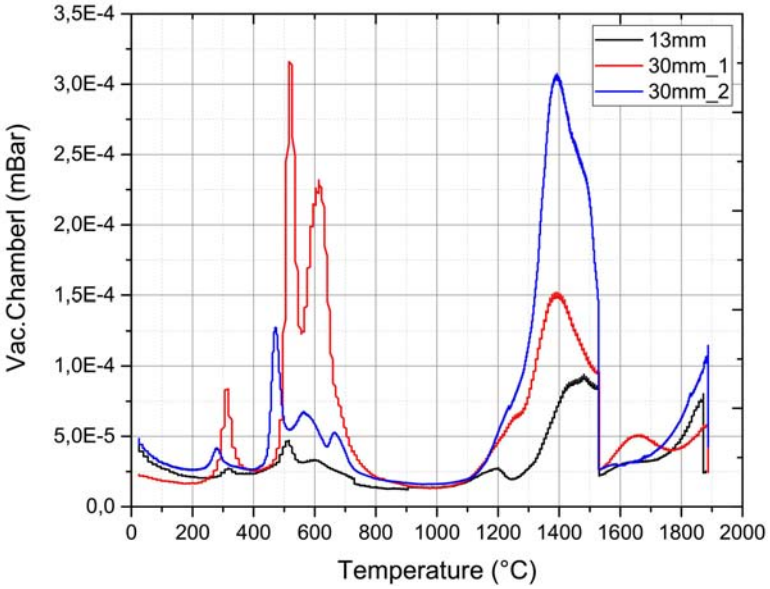

Figure 4.37: Pressure measurement inside the reaction chamber during heat different heat treatments. 13 *mm* concerns 13 *mm* targets production (Figure 4.19), 30 *mm*_1 is related to heat treatment 1 of 30 *mm* pellets (Figure 4.35), finally 30 *mm*_2 represents the new heat treatment reaction chamber pressure measurement for 30 *mm* targets production.

Observing Figure 4.37, both peaks between 350 ÷ 800 °C due to phenolic resin - water decomposition and peaks at T>1000 °C related to carbothermal reaction of new heat treatment applied to 30 *mm* pellets were about three times larger than 13 *mm* ones, as it should be.
Therefore, gas produced by phenolic resin and water decomposition was released very slowly from the sample allowing its drainage through the material, indeed after Heat treatment 4 the specimens did not present bubbles onto their surface as shown in Figure 4.38.

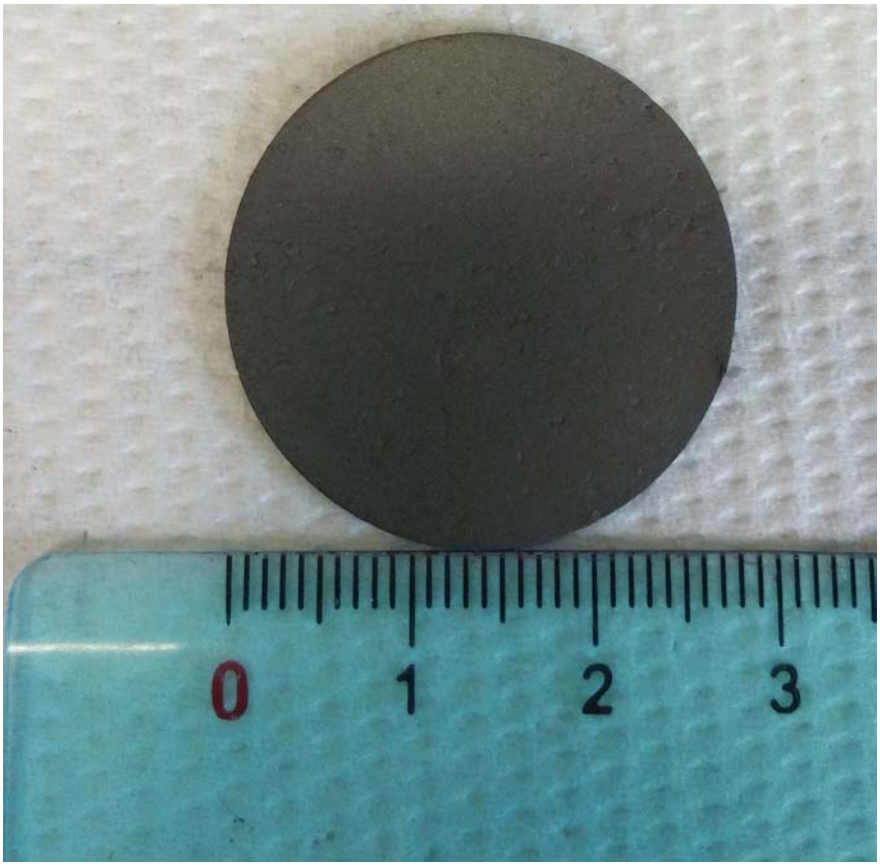

Figure 4.38: ZrC_x target after Heat treatment 4.

After Heat treatment 4, 30 *mm* samples presented a uniform microstructure in both surface (Figures 4.39, 4.40, 4.41) and internal section (Figures 4.42, 4.43, 4.44): excess carbon foils (black colored) were well distributed all over the material, while there were neither large dense aggregates such as in Heat treatment 3 nor white grains.
Moreover, an extreme similarity between 30 *mm* and 13 *mm* targets microstructures (both superficial and internal) can be observed, which means that the gas release and the carbothermal reaction occurred in the same way providing a good microstructrure.
Therefore, decreasing the heating rate bubbles formation was avoided thanks to a slower gas release through the material and carbothermal reduction had enough time to complete and to homogenize the microstructure, which resulted uniform and without oxides (white grains) in both samples surface and internal section.

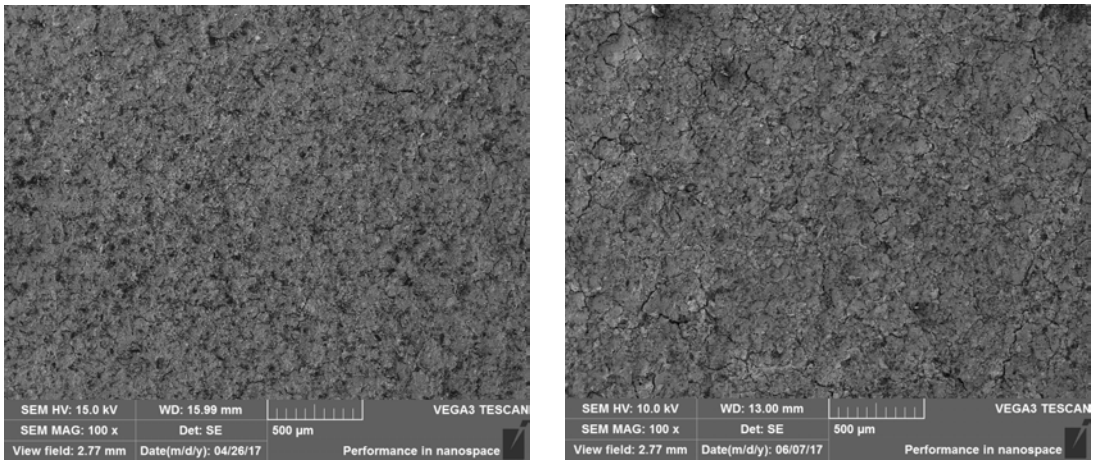

(a) 13 *mm* sample. (b) 30 *mm* sample.

Figure 4.39: Comparison between surfaces of 13 *mm* and 30 *mm* samples. MAG: 100 x.

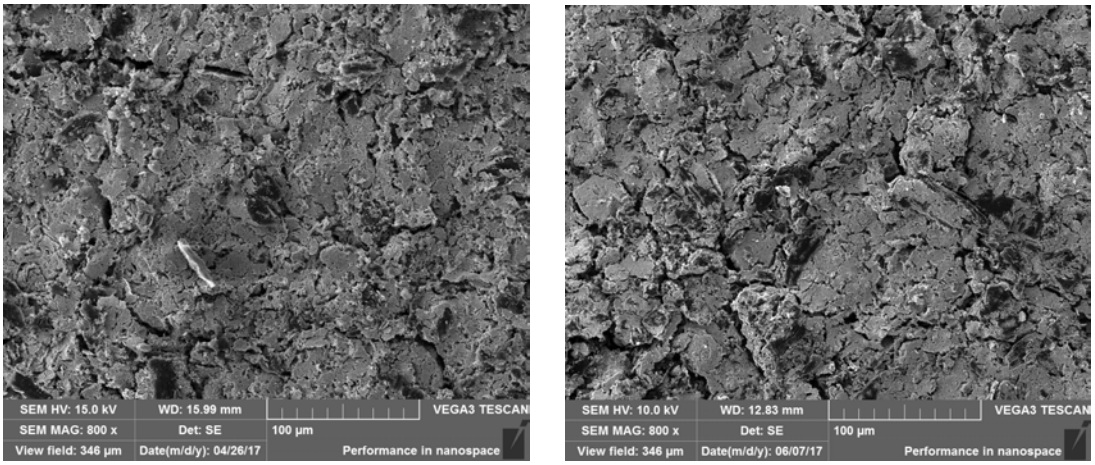

(a) 13 *mm* sample. (b) 30 *mm* sample.

Figure 4.40: Comparison between surfaces of 13 *mm* and 30 *mm* samples. MAG: 800 x.

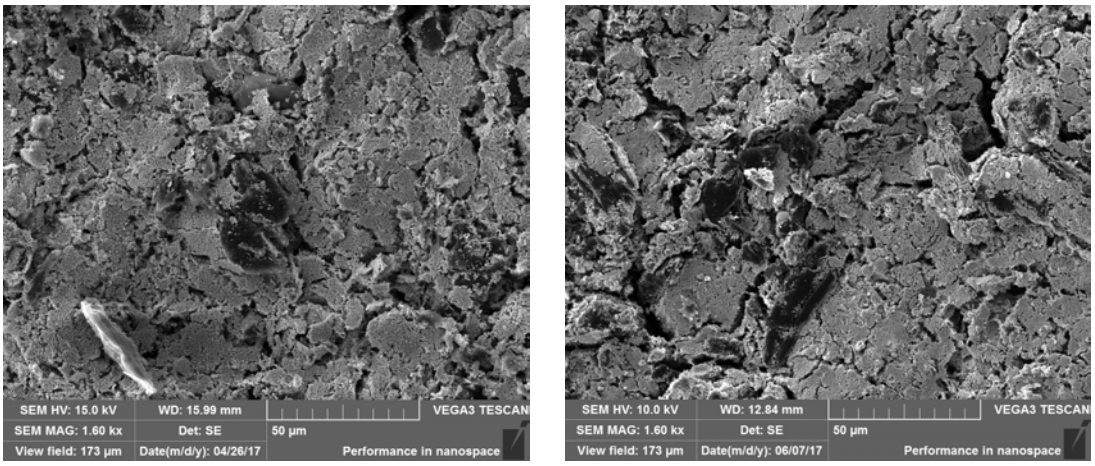

(a) 13 *mm* sample. (b) 30 *mm* sample.

Figure 4.41: Comparison between surfaces of 13 *mm* and 30 *mm* samples. MAG: 1600 x.

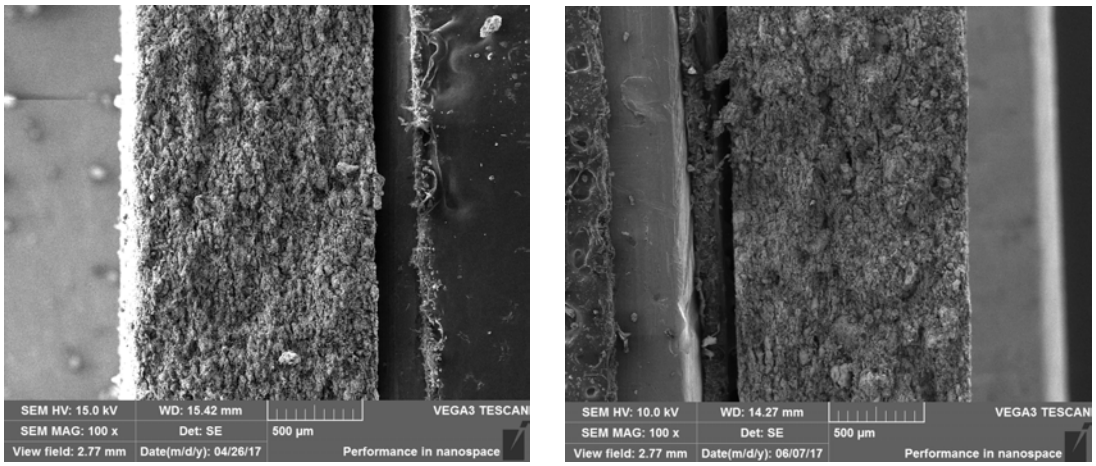

(a) 13 *mm* sample. (b) 30 *mm* sample.

Figure 4.42: Comparison between internal sections of 13 *mm* and 30 *mm* samples. MAG: 100 x.

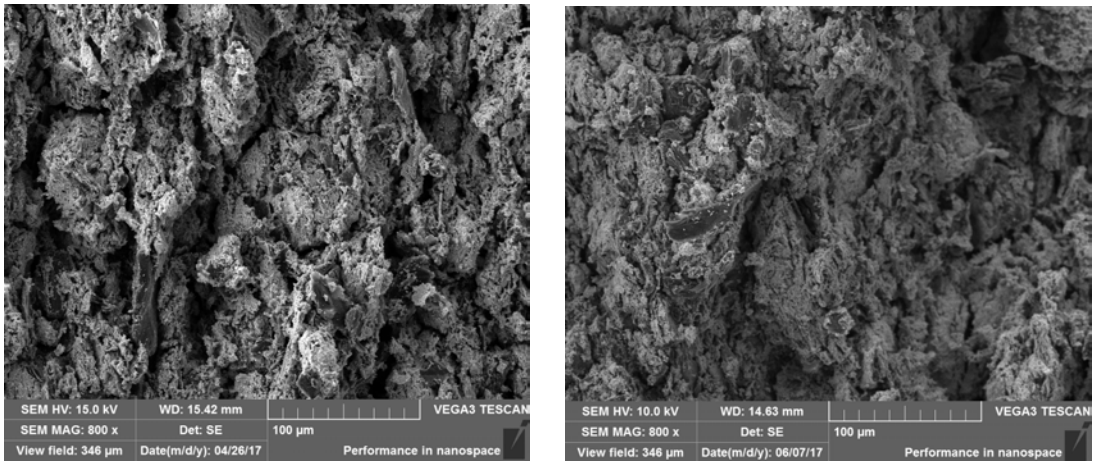

(a) 13 *mm* sample. (b) 30 *mm* sample.

Figure 4.43: Comparison between internal sections of 13 *mm* and 30 *mm* samples. MAG: 800 x.

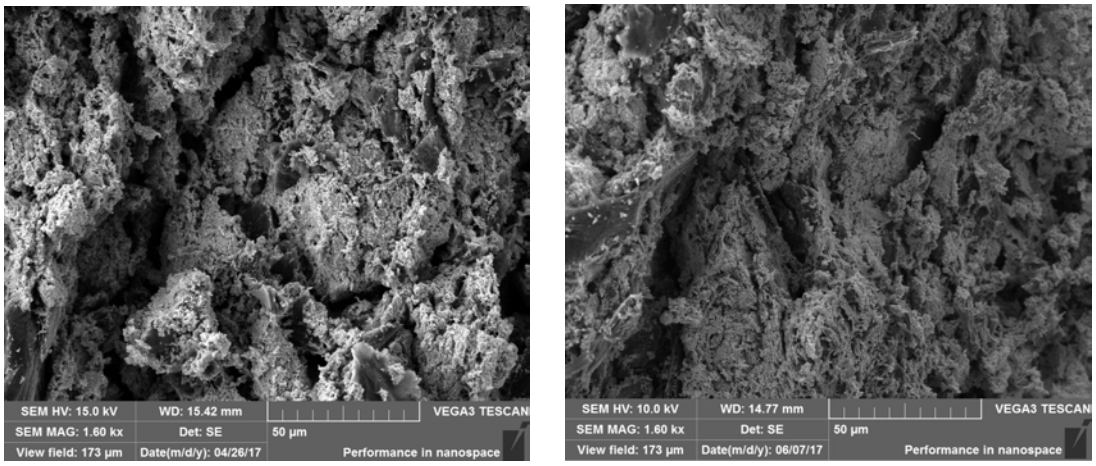

(a) 13 *mm* sample. (b) 30 *mm* sample.

Figure 4.44: Comparison between internal sections of 13 *mm* and 30 *mm* samples. MAG: 1600 x.

The average mass loss reported in Table 4.5 was about 32%, which is very close to the theoretical one (about 34%) ; furthermore, 30 mm ZrC_x targets treated with Heat treatment 4, shown a diameter shrinkage and a thickness expansion, that was the same behavior of 13 mm samples after Heat treatment 2 (Paragraph 4.1.4).
Therefore a slow heating rate allowed completion of carbothermal reduction in which all ZrO_2 was converted in ZrC thanks to the reaction with graphite.

Table 4.5: Samples size (D=diameter, t= thickness) and mass (m) before treatment (b.t) and their variations after Heat treatment 4.

Sample	m b.t. $[mg]$	Mass loss %	D b.t. $[mm]$	D reduction %	t b.t. $[mm]$	t increase %
3	1940	33,3	30,14	6,4	1,17	9,3
4	1947	32,9	30,11	6,1	0,95	22,8
5	1998	31,0	30,23	5,9	1,05	13,2
6	2001	30,6	30,11	5,1	1,12	13,8
7	1998	30,7	30,08	5,5	1,15	13,5
Average	1977	31,7	30,13	5,8	1,09	14,5

The average porosity value in Table 4.6 was much less than the one obtained after Heat treatment 3 (74,5%), which means that Heat treatment 4 avoided quick gas release that caused bubbles formation inside samples.

Table 4.6: Measured values after Heat treatment 4 to estimate porosity by equations .

Sample	Mass $[mg]$	Diameter $[mm]$	Thickness $[mm]$	Density $[g/cm^3]$	Porosity %
3	1294	28,21	1,29	1,606	65
4	1306	28,27	1,23	1,692	63
5	1379	28,46	1,21	1,792	61
6	1388	28,58	1,30	1,665	63
7	1384	28,42	1,33	1,641	64
Average	1350	28,39	1,27	1,679	63

4.2.4 X-Ray Diffraction analysis

For 30 *mm* ZrC_x samples subjected to Heat treatment 4, XRD analysis confirmed the presence of two phases: graphite, which was in excess as desired, and ZrC; indeed experimental XRD pattern peaks were perfectly overlapped by "standards" of both carbon and ZrC as shown in Figure 4.45.

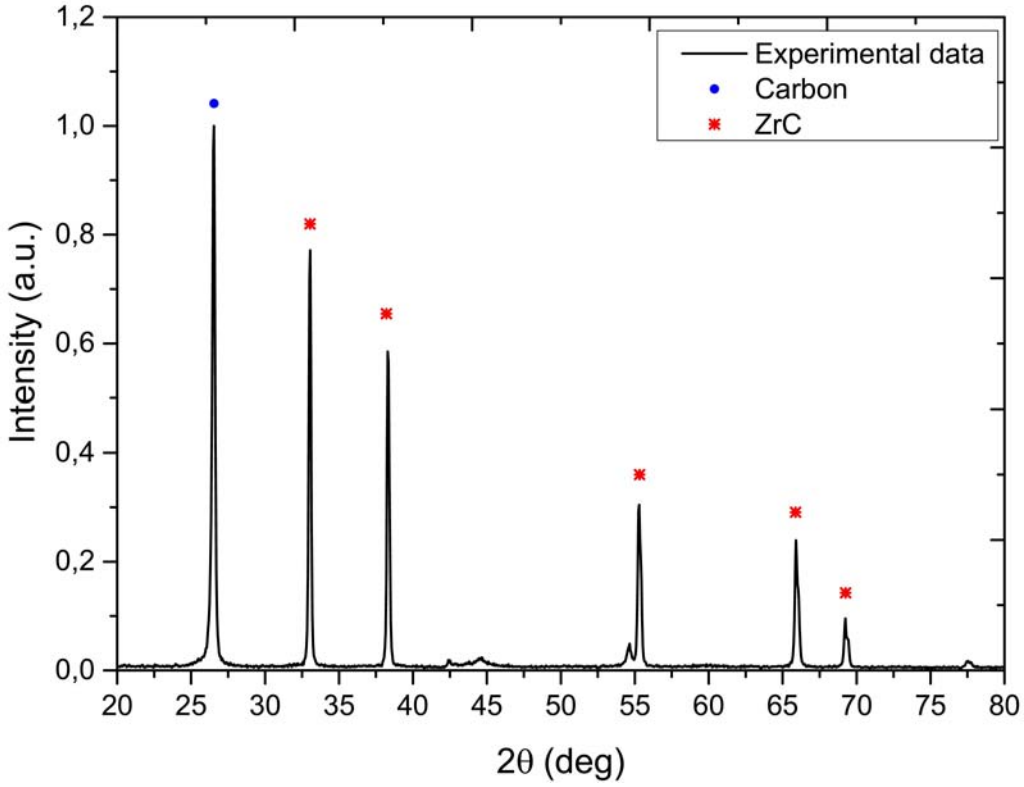

Figure 4.45: Experimental XRD pattern peaks correspond perfectly both to graphite and zirconium carbide ones.

4.3 Physisorption

The term “physical adsorption” or “physisorption” refers to the phenomenon of gas molecules adhering to a surface without the formation of a chemical bond at a pressure less than the vapor pressure. This process takes places on all the surface and it can form multiple layers: the attractions between the molecules being adsorbed and the surface are relatively weak and definitely not covalent or ionic, thus it is is easily reversed. Furthermore the adsorption could be accompanied by absorption, which is the penetration of the fluid into the solid phase. [41]

This phenomena allows the micro and meso-porosity study of a material thanks to a physisorption analyzer such as Micromeritics ASAP 2020 used in this work (see Figure 4.46). The analysis is based on the measurement of the adsorption and desorption isotherm which is the measurement of the amount of gas (nitrogen) adsorbed versus its relative P/P^0, where P^0 is the is the gas saturation pressure, at constant temperature. The slightest change in the shape of the plotted isotherm is indicative of a particular surface feature. Analyses of physical adsorption isotherm data reveal the surface areas, pore sizes, shapes and distributions.

In order to investigate the type of generated porosity, the samples were analyzed by nitrogen physisorption at -196 °C. The specimens were broken in small pieces and placed inside a sample holder ampoule where they are firstly outgassed at 350 °C for 24 hours in vacuum (10^{-2} *mbar*) to remove surface contamination and adsorbed species. Next, the outgassed sample can be moved inside the analysis station for other 24 hours where nitrogen is introduced at cryogenic temperatures; known aliquots are dosed up to saturation pressure, then a vacuum is applied and the gas is removed, which may result in hysteresis behavior.

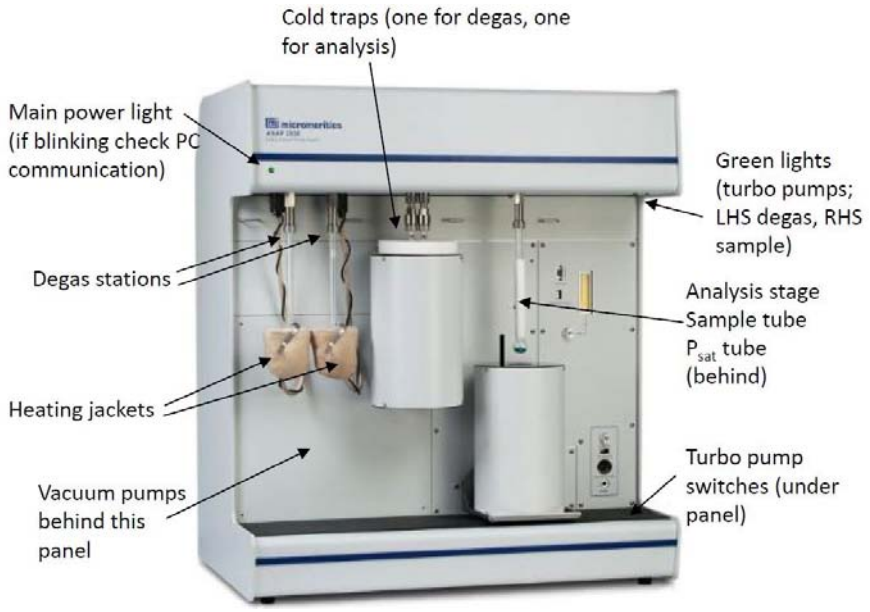

Figure 4.46: Micromeritics ASAP 2020.

Since physisorption is a complex process involving various interaction, the different types of isotherms and of hysteresis loops were described according to IUPAC classifications as shown in Figure 4.47 [59].

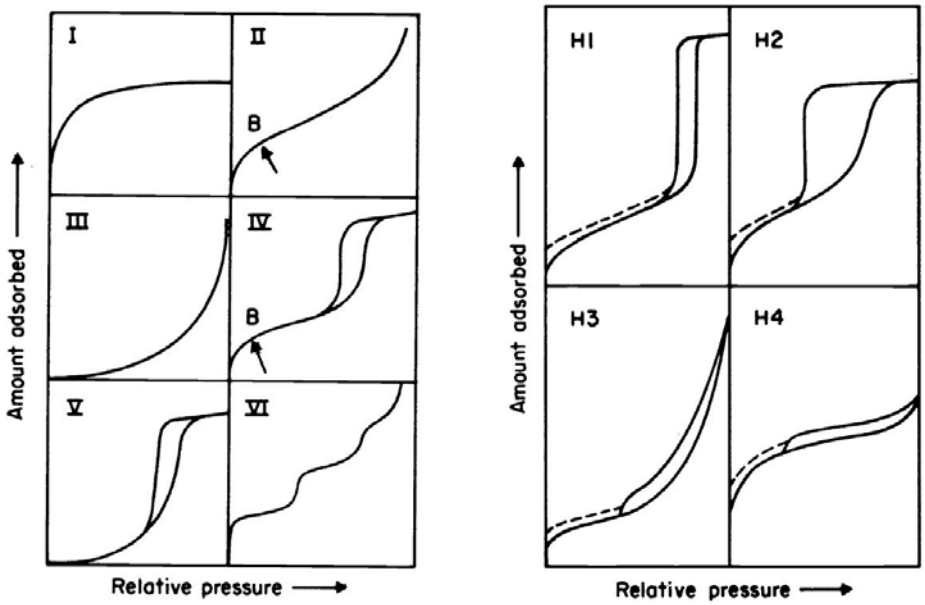

(a) Types of physisorption isotherms. (b) Types of hysteresis loops.

Figure 4.47: IUPAC classifications of physisorption isotherms and hysteresis loop. [59]

The isotherms in Figure 4.47(a) are related to the following materials [59]:

I) Microporous materials with the exposed surface residing almost exclusively inside the micropores, which once filled with adsorbate, leave little or no external surface for further adsorption;

II) Most frequently found when adsorption occurs on nonporous powders or powders with diameters exceeding micropores. Inflection point occurs near the completion of the first adsorbed monolayer;

III) non-microporous materials and materials which have a weak interaction between the adsorbate and adsorbent;

IV) Occurs on porous adsorbents with pores in the range of $1,5 \div 100\ nm$. At higher pressures the slope shows increased uptake of adsorbate as pores become filled, inflection point typically occurs near completion of the first monolayer;

V) Are observed where there is small adsorbate-absorbent interaction potentials (similar to type III), and are also associated with pores in the $1.5 \div 100\ nm$ range;

VI) Homogeneous surface materials.

The main types of hysteresis loop are exposed in Figure 4.47(b) and they are related to the following systems [59]:

H1) Materials produced by compaction of spherical particles, quite regular, which leads to a narrow pore size distribution;

H2) Non-uniform pore size and distribution;

H3) Materials composed by crushed particles with stretched form with a broad pore size distribution;

H4) Materials characterized by stretched and tight pores.

Once the isotherm obtainment, several models was developed to analyze the experimental data. In particular applying the BET method (Brunauer, Emmett, Teller) it was possible to calculate the total specific surface area (SSA $[m^2/g]$), while the computational method developed by Barrett, Joyner and Halenda (BJH) can be employed to derive the micro and meso-pore size distribution, their volume and specific surface [41].

4.3.1 Physisorption results

For 30 mm ZrC_x samples subjected to Heat treatment 4, BET method provided a surface area of 3.6977 m^2/g which was relatively low and similar to that of other carbides obtained by carbothermal reduction in high vacuum; however, according to IUPAC classification and comparing the obtained curves in Figure 4.48 with the reference ones reported in Figure 4.47, the absorption isotherm can be identified as of Type III, while the hysteresis shape is between H3 and H4 (which are similar), according to Figure 4.47(b).

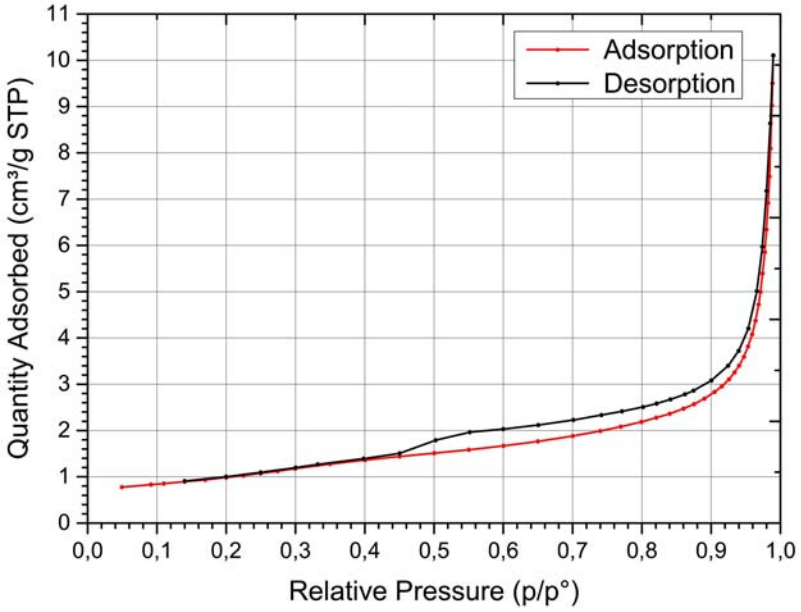

Figure 4.48: Isothermal liner plot.

Pore size distribution is displayed in Figure 4.49, in particular a little sharp peak at about 4 *nm* can be observed; however pore size distribution is considered almost broad because the single peak does not prevail with respect to pore widths over 30 *nm*.

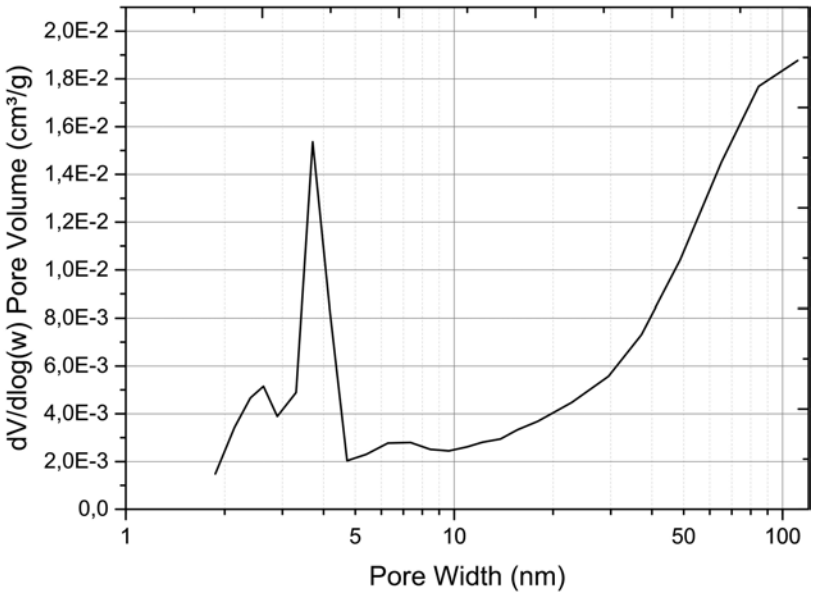

Figure 4.49: BJH desorption pore size distribution.

4.4 Conclusions

ZrC targets with carbon excess to improve the isotopes release, called ZrC_x, of different size (13 *mm* and 30 *mm* diameters) were successfully obtained through carbothermal reduction using ZrO_2 and graphite as precursors.
The first stage consisted of finding the minimum binder (phenolic resin) amount that provided, after pressing, enough mechanical resistance to allow for pellets handling without loss of powder. After that, the heat treatment to realize reaction 4.1.1 for 13 *mm* targets was designed; when samples were heat treated at 1800 °C (Heat treatment 1), oxides presence were found thanks to a SEM-EDS analysis in Figure 4.16 and 4.17. Whereby, heat treatment maximum temperature was increased at 1900 °C (Heat treatment 2) providing an oxide-free material.
Sample microstructure resulted after Heat treatment 2 was characterized as desired by:

- ZrC matrix;
- residual graphite shaped as "black foils" that were well randomly distributed through both the sample surface and internal cross section;
- porosity.

In particular, the estimated material porosity fraction (through Equations (4.1.2), (4.1.3), (4.1.4)) was $P = 57\%$.
30 *mm* samples were heat treated employing the latter heating cycle, but results were not satisfying: microstructure was not uniform as the 13 *mm* one, indeed it was characterized by the presence of many dense harmful aggregates, furthermore porosity fraction estimation amounted to 74,5%. However, no oxides were detected by EDS analysis, which means that the heat treatment maximum temperature (1900 °C) was enough to complete the carbothermal reduction, nevertheless the heating ramp used to produce 13 *mm* samples was not suitable for 30 *mm* one because of a too high heating rate that did not provide microstructure homogeneity .
Consequently, a new heat treatment with a very low heating rate was designed (Heat treatment 4); it successfully provided about the same microstructure obtained by Heat treatment 2 for 13 *mm* samples, a porosity value of 63% and mass loss very close to the theoretical one. Moreover, XRD analysis confirmed the presence of only ZrC and excess carbon.
In order to have a better understanding of porosity, a phisisorption analysis was performed: the material was characterized as non-microporous, having a low surface area of 3.6977 m^2/g, composed by crushed particles with stretched form with a broad pore size distribution (confirmed by BJH desorption analysis) having stretched and tight pores.

CHAPTER 5

Zirconium Germanide

Zirconium germanide does not take place in common applications, consequently literature provides such a low amount of information that both its synthesis and characterization result problematic for several aspects that will be analyzed in this chapter.
In particular, two different synthesis method will be described, moreover SEM, EDS, XRD analysis will give new information about this material and its production issues.

5.1 Germanothermic reduction

Germanothermic reduction employs as precursors ZrO_2 (Sigma-Aldrich, 99% trace metals basis, particle size 5 μm) and germanium powders (Sigma-Aldrich powder, -100 mesh, $\geq$ 99.999% trace metals basis - very expensive) which were mixed together, pressed at 750 MPa for one hour to form 13 mm pellets and heat treated under high vacuum conditions to avoid oxygen contamination using the same apparatus described in Section 4.1.
The reaction can be described as follows:

$$ZrO_2 + 3\,Ge \longrightarrow ZrGe + 2\,GeO \tag{5.1.1}$$

Powder mixture were prepared taking into account that germanium was more volatile than transition metal oxides, indeed at temperatures of the order of 1000 °C its vapor pressure is $1,33 - 10^{-1}\ Pa$ [15]. Because of this, the amounts of germanium introduced into the charges were in excess with respect to the theoretical quantity required for the reaction stoichiometry.
The first mixture were prepared without any binder and Ge excess was 10 wt.% [15]:

- ZrO_2 : 34 wt.%;
- Ge : 66 wt.%.

5.1.1 Heat treatment 1

Such a mixture composition did not allow the pellet integrity; as a consequence of that, pellets broke in several pieces, however the first heat treatment (Heat treatment 1) that was tested is represented by graph in Figure 5.8 and it consisted of two phases [15]:

1. Slow heating (100 °C/h) up to 1700 °C, dwell time of 45 minutes at 1700 °C, to homogenize the temperature and to allow germanothermic reaction completion;

2. Cooling to room temperature (100 °C/h).

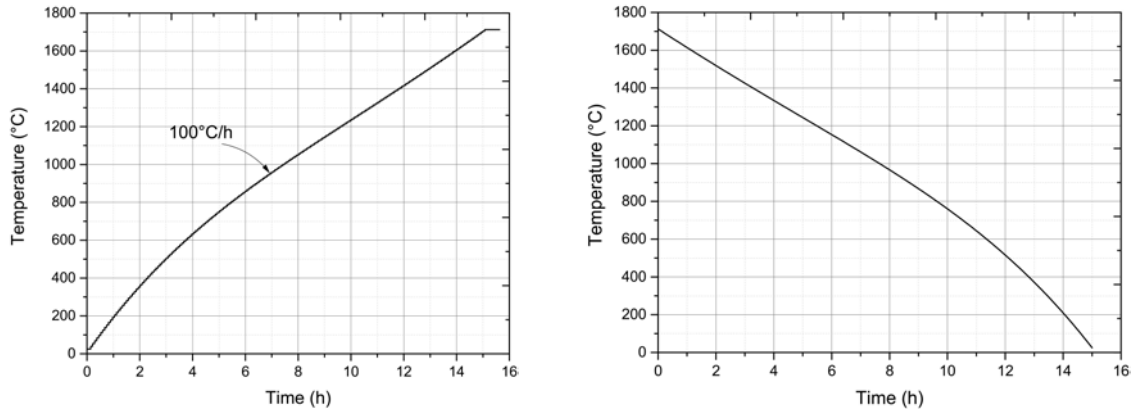

(a) Heating ramp. (b) Cooling ramp.

Figure 5.1: First heat treatment for 13 *mm* samples.

Figure 5.2 displays the pressure measurement inside the furnace reaction chamber during the heat treatment, in particular two peaks that represent the gas development can be observed: the former at about 500 °C and the latter above 1200 °C; unluckily the mass spectrometer was not in function during treatment, therefore the developed gas composition is unknown.

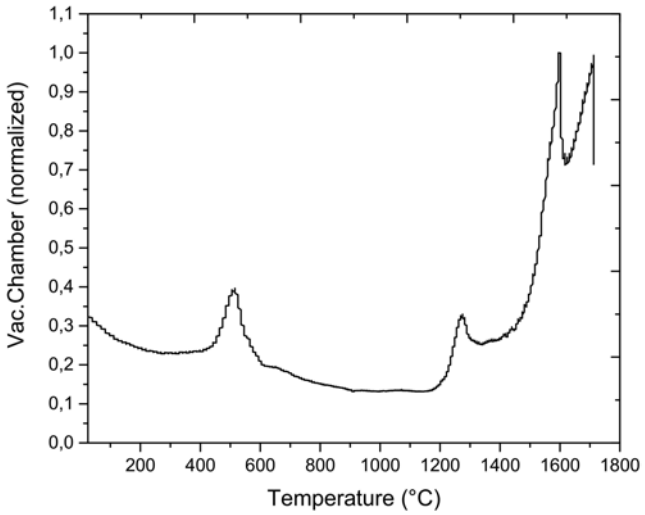

Figure 5.2: Pressure inside the reaction chamber related to the first 13 *mm* heat treated sample.

Figure 5.3(a) shows that pellets reacted with the graphite plate used as samples support during the heat treatment, indeed in Figure 5.3(b) the difference at naked eye between the sample surface in contact with graphite plate and the one which were not in contact (called "*free*") is shown.

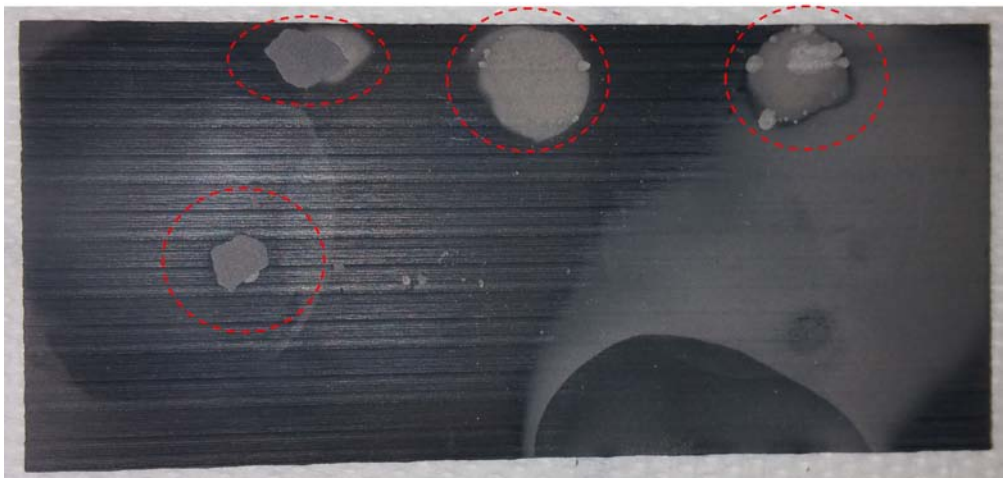

(a) Clear regions circled in red are the ones where samples reacted.

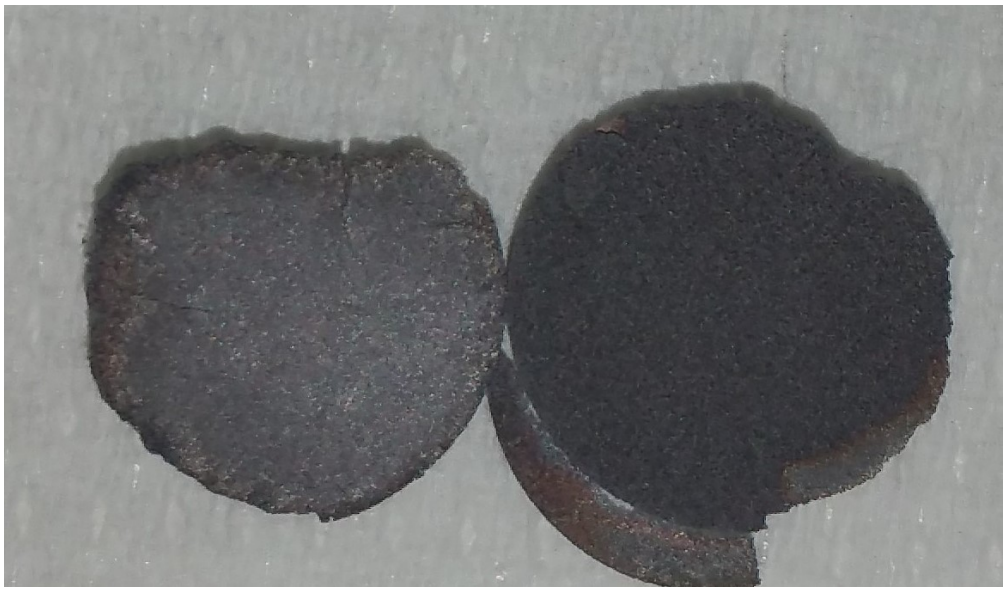

(b) Difference between the two sample sides. The right one was in contact with graphite plate, while the other one was free.

Figure 5.3: Samples reacted with graphite plate.

SEM micrographs shown in Figure 5.4, 5.5, 5.6 demonstrate the difference between the two sample surfaces at different magnifications; microstructures were very different from each other, furthermore they were both caracterized by a high porosity which led to an extremely low mechanical resistance.

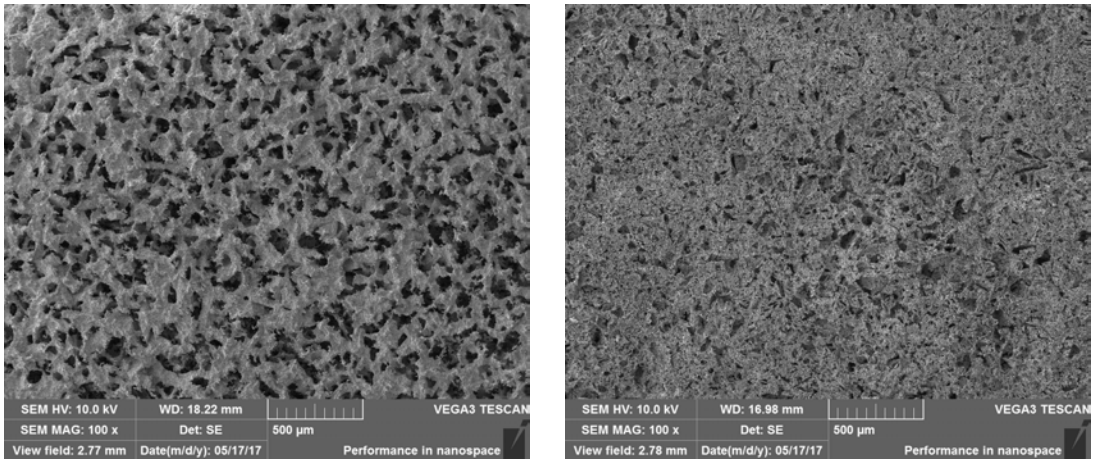

(a) Contact surface. (b) Free surface.

Figure 5.4: Comparison between the two sample surfaces. MAG: 100 x.

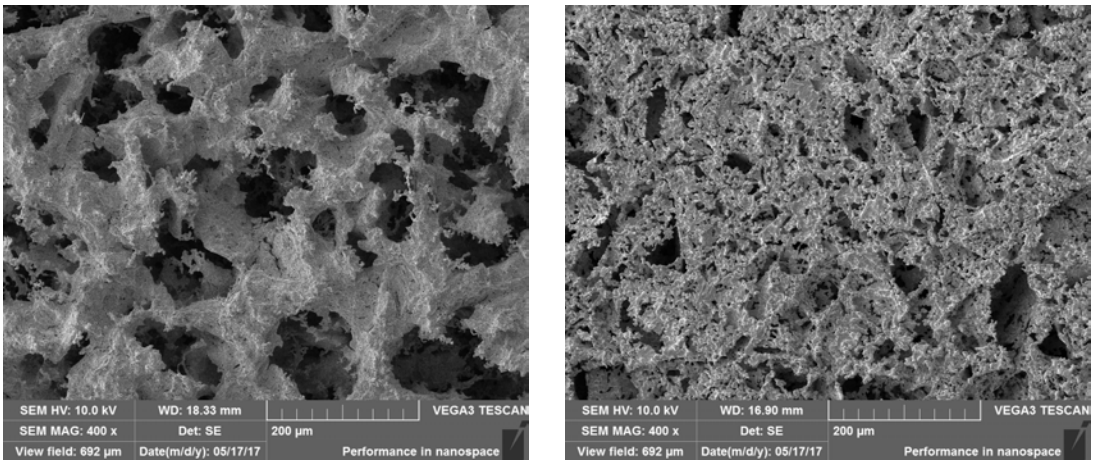

(a) Contact surface. (b) Free surface.

Figure 5.5: Comparison between the two sample surfaces. MAG: 400 x.

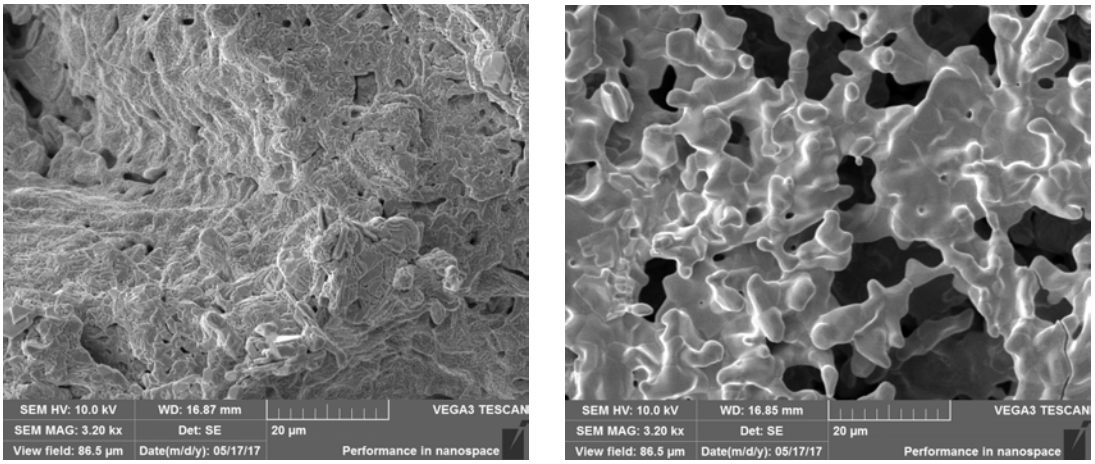

(a) Contact surface. (b) Free surface.

Figure 5.6: Comparison between the two sample surfaces. MAG: 3200 x.

5.1.2 Heat treatment 2

In order to avoid any possible reaction between the pellets and the graphite plate, a tantalum sheet were fixed thanks two tantalum wires onto graphite plate as shown in Figure 5.7.

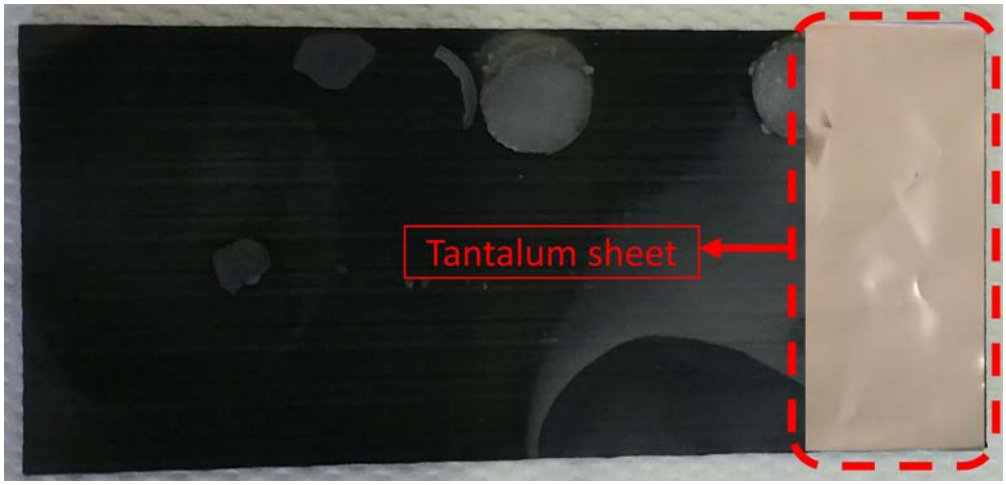

Figure 5.7: Tantalum sheet used to avoid reaction between pellets and graphite.

The new heat treatment (called "Heat treatment 2") was designed to complete the germanothermic reaction that probably occurred in correspondence of maximum gas development shown in Figure 5.2 between 1450 °C and 1600 °C; it consisted of three steps:

1. Slow heating (100 °C/h) up to 1550 °C, dwell time of 3 hours at 1550 °C, to promote and possibly complete the germanothermic reaction (5.1.1) ;
2. Heating (100 °C/min) up to 1700 °C, dwell time of 4 hours at 1900 °C, to sinter the powders.
3. Cooling to room temperature (100 °C/h, as for Heat treatment 1).

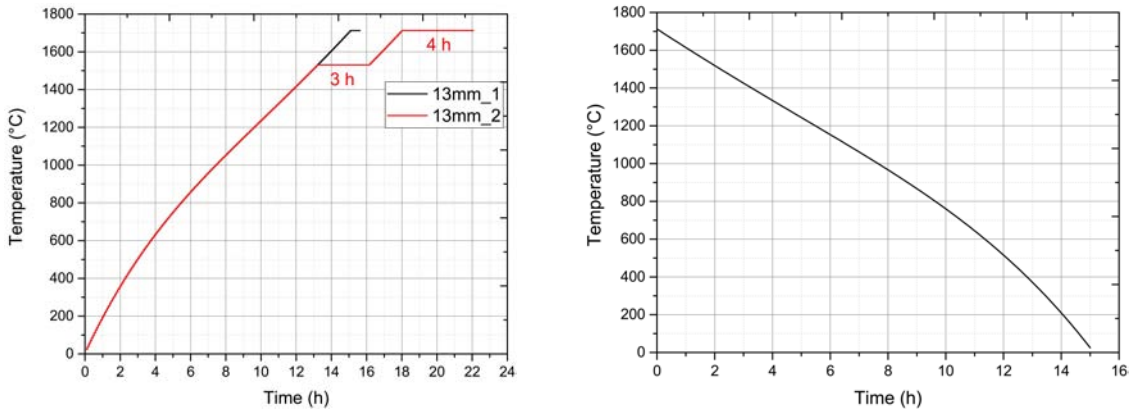

(a) Heating ramp.

(b) Cooling ramp.

Figure 5.8: Heat treatment 2 (13mm_2) for 13 *mm* samples.

Figure 5.9 displays the pressure measurement inside the reaction chamber during different heat treatments; the peak at around 500 °C almost disappeared in Heat treatment 2, since the only

difference between heat treatments was the Ta sheet, it may be that such a pressure increase during Heat treatment 1 occurred as consequence of reaction between graphite plate and pellets. Moreover, pressure increased in Heat treatment 2 even after dwell at 1550 °C, in particular it could be due to:

- Uncompleted germanothermic reaction;
- Ge evaporation (its vapor pressure is high at such temperatures);
- Gas release from from the materials that constitutes the furnace internal components.

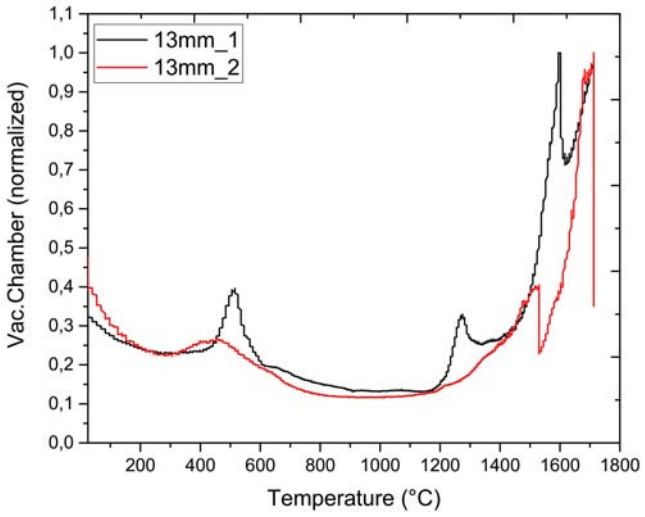

Figure 5.9: Pressure inside the reaction chamber during Heat treatment 2 (13mm_2).

SEM micrographs taken at different magnifications in Figure 5.10, 5.11, 5.12 show the difference between contact (with Ta sheet) and free surfaces microstructure, therefore even changing heat treatment steps and modifying the contact surface material, different processes characterized the two sample sides leading to different microstructures which both resulted very porous.

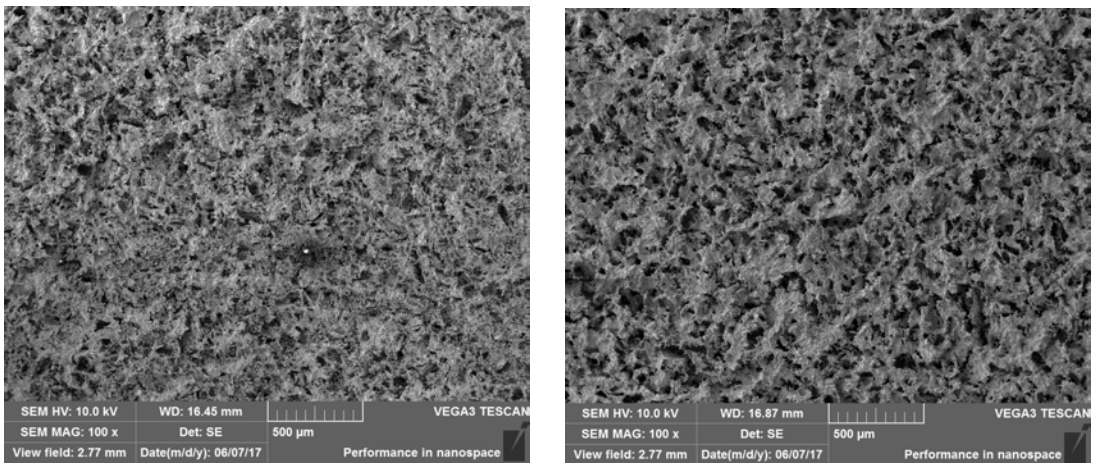

(a) Tantalum contact surface.

(b) Free surface.

Figure 5.10: Comparison between the two sample surfaces. MAG: 100 x.

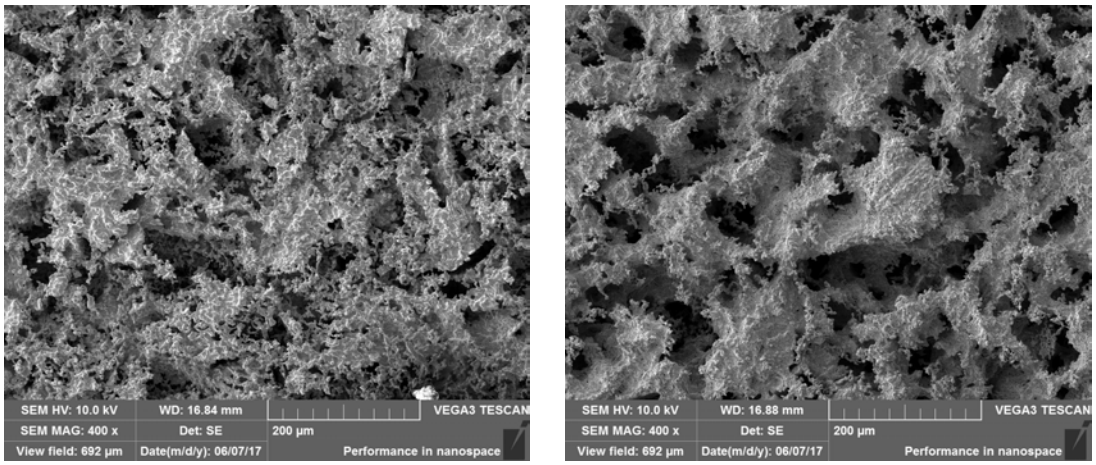

(a) Tantalum contact surface. (b) Free surface.

Figure 5.11: Comparison between the two sample surfaces. MAG: 400 x.

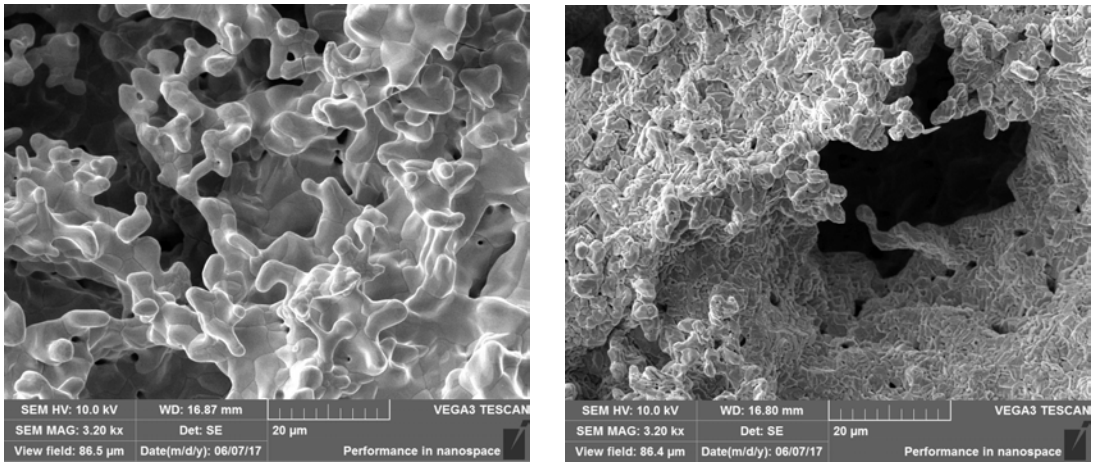

(a) Tantalum contact surface. (b) Free surface.

Figure 5.12: Comparison between the two sample surfaces. MAG: 3200 x.

Such a difference was investigated by EDS analysis in Figure 5.13: free surface was constituted by only zirconium (Figure 5.13(b)), while contact surface presented both germanium and zirconium (Figure 5.13(a)); therefore, the aforementioned hypothesis of Ge evaporation due to its high vapor pressure at heat treatment maximum temperature was confirmed, but only concerning the free surface. The Ta sheet was probably capable to retain Ge which remained available for germanothermic reduction in the contact surface.

Moreover, a little peak corresponding to oxygen in Figure 5.13(a) can be observed: its presence could be due both to uncompleted ZrO_2 transformation and air contamination during samples handling. Therefore an XRD analysis will be necessary to identify the material phases.

However, no Ta was identified, thus the tantalum sheet is a suitable support for the pellets because it did not react with them.

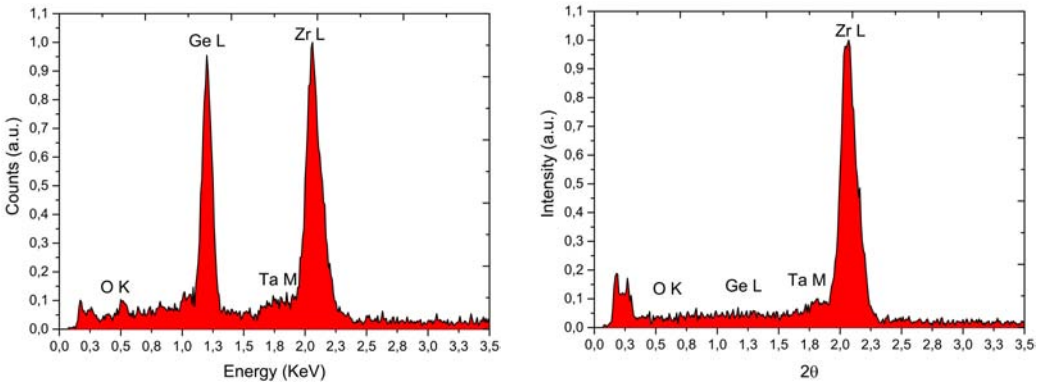

(a) Tantalum contact surface.

(b) Free surface.

Figure 5.13: EDS analysis taken at MAG 3200 x (Figure 5.12) of the two sample surfaces.

Samples after Heat treatment 2 were subjected to an XRD analysis, which is displayed in Figure 5.14: most of peaks corresponded to Ge_3Zr_5 which was characterized by a Ge content lower than ZrGe; furthermore, even peaks referred to Zr_3GeO_8 were identified in the experimental pattern which means that the oxygen presence was not given by a contamination during specimens handling, but it was probably due to uncompleted ZrO_2 transformation through germanothermic reduction.

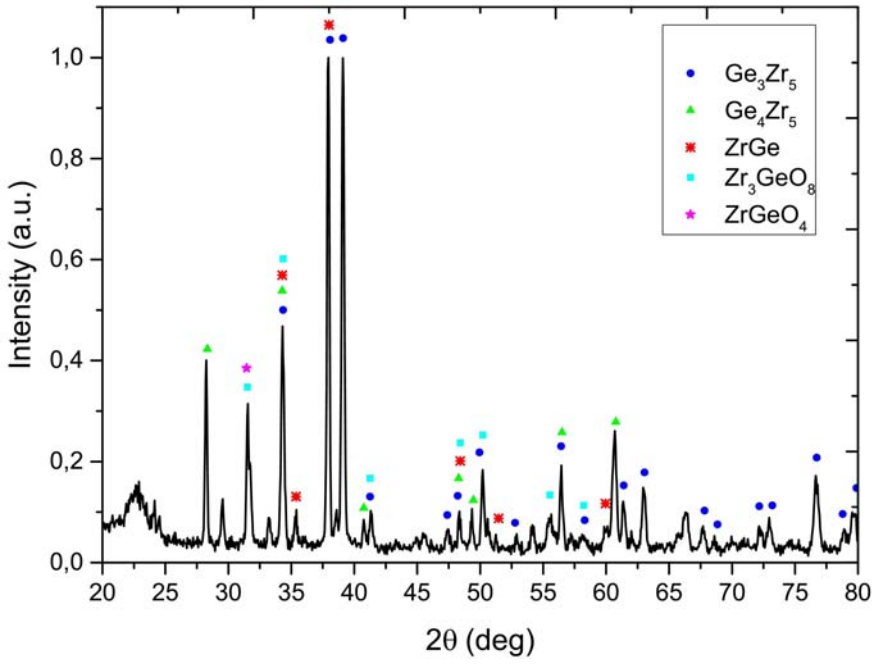

Figure 5.14: XRD analysis after Heat treatment 2.

The average weight loss after Heat treatment 2 was 67%, while the theoretical one calculated from reaction 5.1.1 amounts to 59,6%, thus more material (likely Ge) left pellets during heat treatment than the expected one.

The great stability of ZrO_2 at high temperature did not allow its reaction completion with Ge at

1700 °C, however increasing the heat treatment temperature, Ge loss will increase as well; since germanium powder is very expensive and considering that most of Ge naturally left because of GeO formation during germanothermic reaction, this process was not convenient so it was abandoned to develop the zirconium hydride method described in the following Section.

5.2 Zirconium hydride method

ZrGe can be produced thanks to reaction 5.2.1 using as precursors zirconium hydride (Sigma Aldrich, -325 mesh, 99%) and germanium powders (Sigma-Aldrich powder, -100 mesh, $\geq$ 99.999% trace metals basis) [51].

$$ZrH_2 + Ge \longrightarrow ZrGe + H_2 \tag{5.2.1}$$

Powder mixtures were prepared employing the same apparatus described in Section 4.1: reagents were mixed together, pressed at 750 *MPa* for one hour to form 13 *mm* pellets and heat treated under high vacuum conditions to avoid oxygen contamination.
Pellets obtained by pressing only powders broke in several pieces after mold extraction, therefore it was necessary to find a binder that provided a mechanical resistance high enough to allow samples handling without leaving contamination after heat treatment.; in this case, polyethylene glycol (PEG), which is one of the most used binders for dry pressed ceramics, was adopted since it ensures a very low carbon residual after its thermolysis.
Several pellets were produced to find the minimum PEG amount to guarantee a high enough mechanical resistance, in particular the ones containing 2 wt.% of PEG broke partially only in their perimeter, while mixtures with 4 wt.% of PEG produced pellets that retained their shape after extraction from mold and they were easily handled for measurements. Table 5.1 collects mixture compositions calculated by reaction stoichiometry 5.15 employed to realize the pellets.

Table 5.1: Different mixture compositions used to produce pellets.

Mixture	wt.% ZrH_2	wt.% Ge	wt.% PEG
1	55,1	42,9	2,0
2	54,0	42,0	4,0

Heat treatments developed for this material were all characterized by two important temperature:

- T_{max} was the maximum heat treatment temperature and it was even used to classify the heat treatment;
- T_1 was an intermediate temperature between room temperature and T_{max}.

Therefore, in order to study the material evolution with treatment temperature, several heat treatments, that were all structured as follows and represented in Figure 5.15, were performed:

1. Slow heating (50 °C/h) up to T_1, dwell time of 3 hours at T_1, to promote and possibly complete reaction 5.2.1;
2. Heating (50 °C/h) up to T_{max}, dwell time of 5 hours at T_{max}, to sinter the reacted powders and homogenize the microstructure;
3. Cooling to room temperature (100 °C/h).

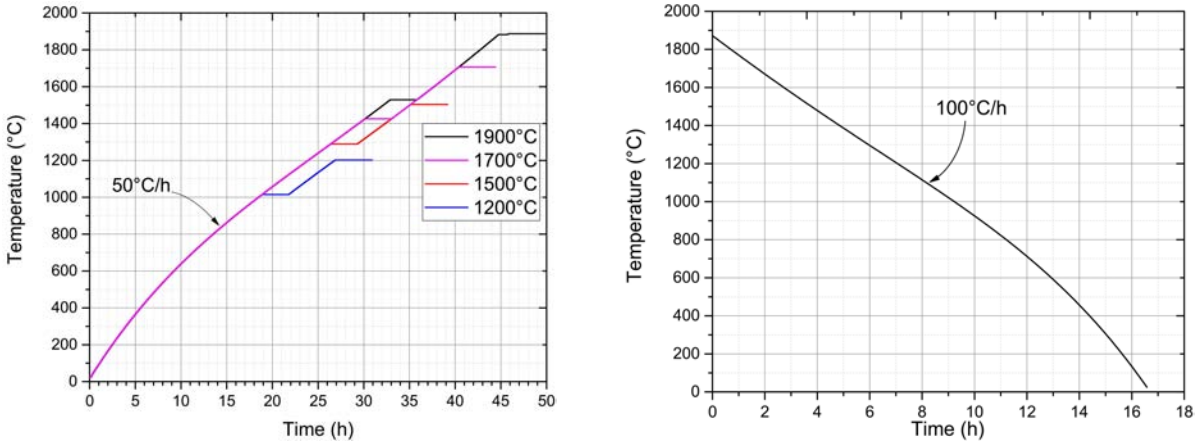

(a) Heating ramps. (b) Cooling ramp example (from 1900 °C).

Figure 5.15: Heat treatments performed on pellets.

For each heat treatment performed, pressure inside the furnace reaction chamber was measured as shown in Figure 5.16.

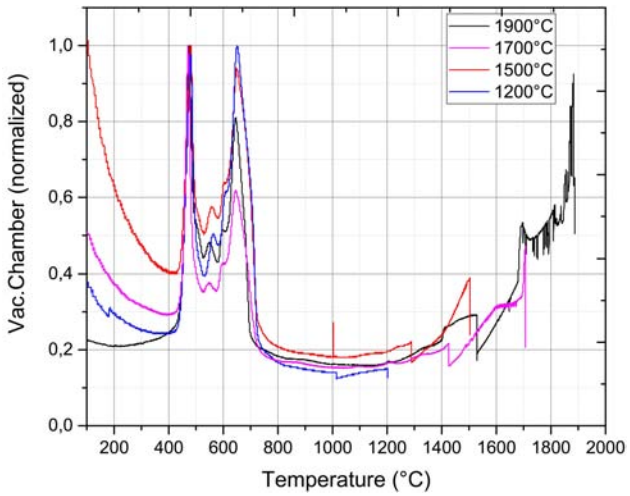

Figure 5.16: Reaction chamber pressure comparison between heat treatments performed.

Between 400 °C and 750°C all heat treatments were characterized by a high pressure increase constituted by two major peaks at about 500 °C and 650 °C which may be caused by both PEG

thermolysis and reaction 5.2.1; however, there were another gas development region for samples heat treated at T>1200 °C which may be due to either Ge evaporation or reaction 5.2.1 if the latter did not occur during previous pressure peaks at 400 ÷ 750 °C just discussed.
Next paragraphs will explain the material evolution in function of the heat treatment performed thanks to SEM, EDS, XRD analysis.

5.2.1 T_{max} =1900 °C heat treatment effects

After the heat treatment at T_{max} =1900 °C samples containing different PEG amounts were deformed in a different way, as shown in Figure 5.17: in particular, the sample characterized by the highest PEG content was swollen due to a large gas development caused by PEG thermolysis; the sample containing 2 wt.% of PEG was even partially deformed, however a lower PEG quantity did not provide pellets integrity during extraction, thus all pellets were realized with 2 wt.% of PEG.

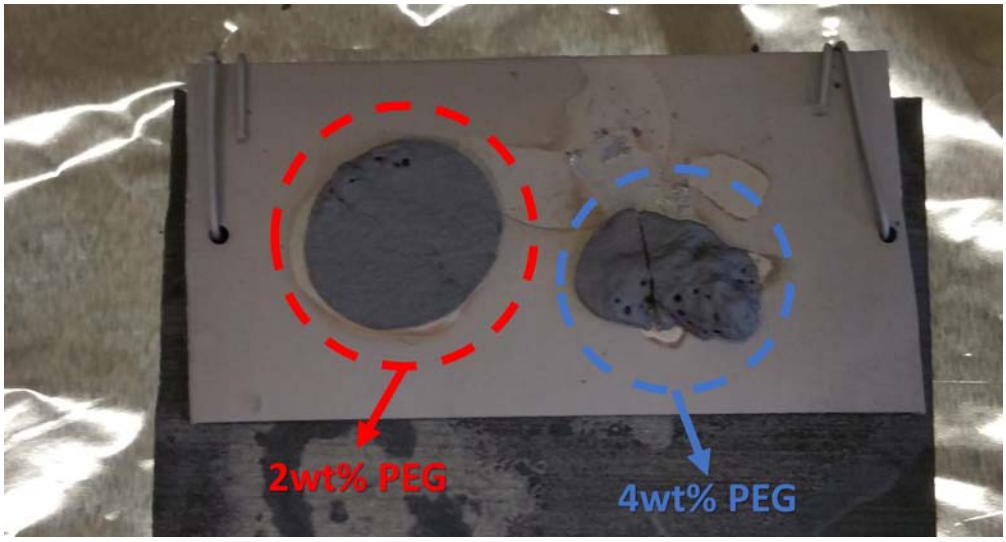

Figure 5.17: Difference between samples heat treated at T_{max} =1900 °C containing 2 wt.% and 4 wt.% of PEG.

SEM micrographs in Figure 5.18 and 5.19 shows the microstructure difference between the contact and free surfaces of the same specimen as well as happened for germanothermic reaction in Paragraph 5.1.2.
EDS analysis demonstrated that the contact surface contained both Zr and Ge, while the free surface was characterized by Ge absence as displayed by Figure 5.20; the tantalum sheet placed below samples was likely capable to retain Ge, which instead evaporated from the specimen free surface. Moreover, neither oxygen nor tantalum by EDS analysis were detected, which means that both oxidation and Ta sheet-pellets reaction did not occur.
The observed microstructures can be both considered very porous: such a porosity may be likely due to a large amount of gas developed by both PEG thermolysis and hydrogen from reaction 5.2.1.

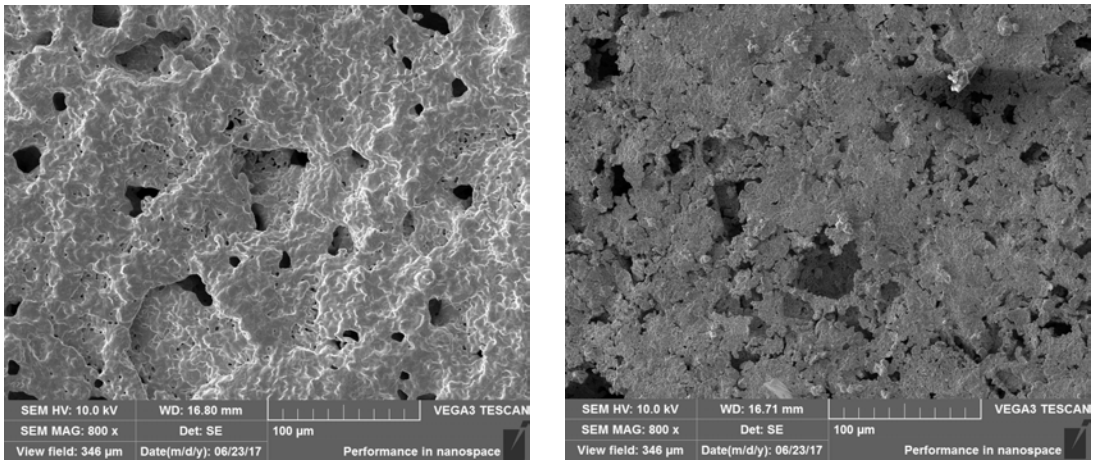

(a) Tantalum contact surface. (b) Free surface.

Figure 5.18: Comparison between the two sample surfaces. MAG: 800 x.

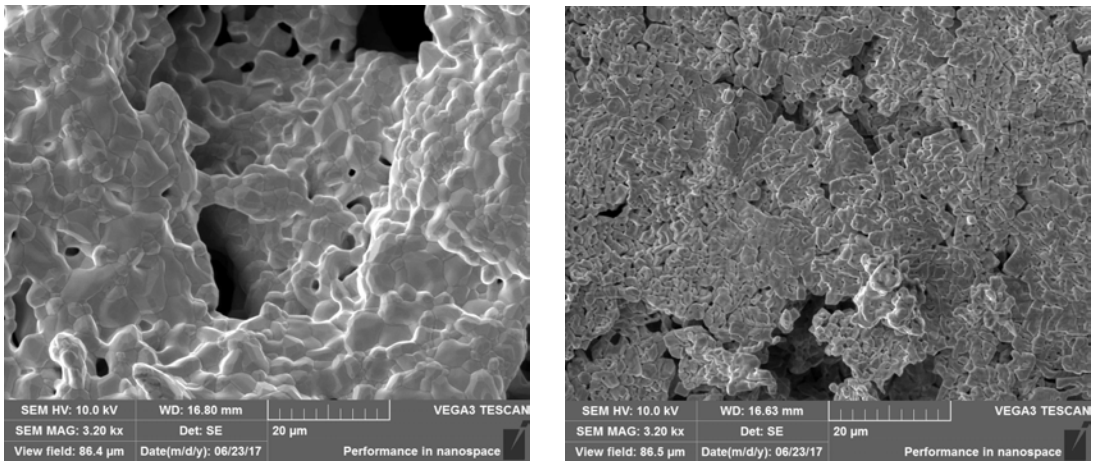

(a) Tantalum contact surface. (b) Free surface.

Figure 5.19: Comparison between the two sample surfaces. MAG: 3200 x.

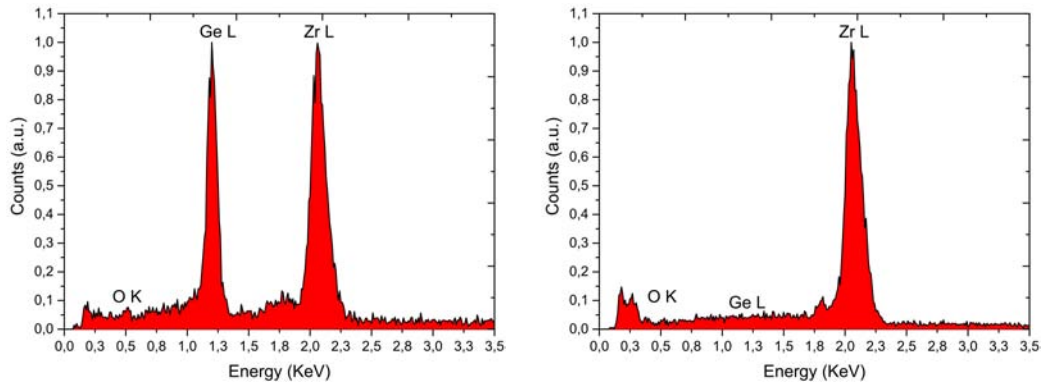

(a) Tantalum contact surface. (b) Free surface.

Figure 5.20: EDS analysis confirmed presence of both Zr and Ge only on contact surface, while on the free surface only Zr was detected.

XRD analysis reported in Figure 5.21 revealed the presence of different phases from ZrGe (Ge_3Zr_5 and Ge_4Zr_5), which were characterized by a lower germanium content, that was expected consequently to germanium evaporation.
However, the experimental pattern did not have any peaks in common with oxidized phases such as Zr_3GeO_8 and $ZrGeO_4$ which were found using ZrO_2 as precursor like in Paragraph 5.1.2.

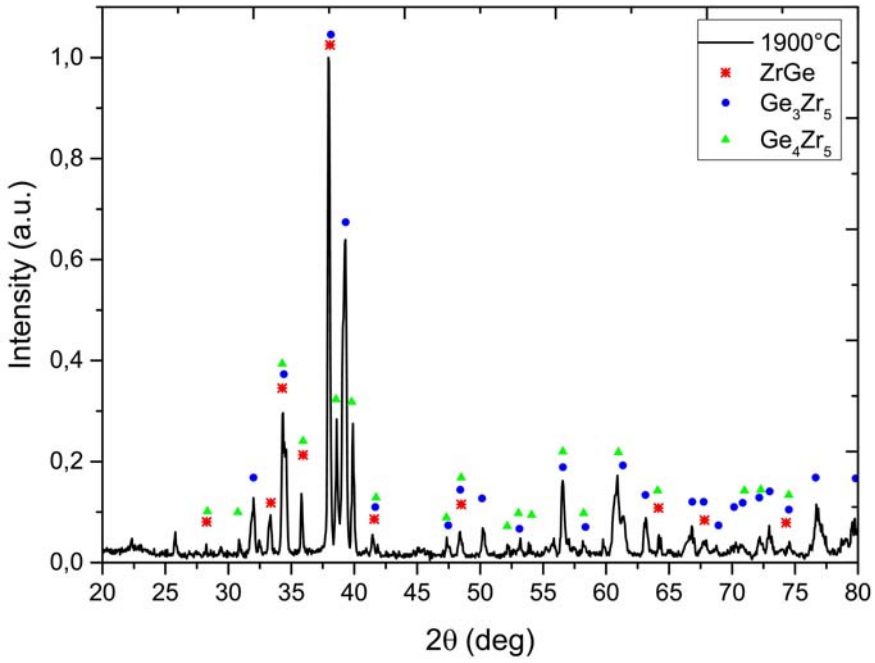

Figure 5.21: XRD analysis after heat treatment characterized by T_{max} =1900 °C.

5.2.2 T_{max} =1700 °C heat treatment effects

Ge evaporation from samples free surfaces issue was solved by placing another tantalum sheet onto the specimen upper surface, since thanks to SEM and EDS analysis in Paragraph 5.1.2 and 5.2.1, the capability of Ta sheet to retain Ge was observed.
Therefore, samples were positioned between two tantalum sheets as in Figure 5.22 in order to avoid Ge loss from the upper samples surface; this solution worked well, indeed SEM and EDS analysis confirmed no differences both in microstructure and composition between the bottom and upper sample surfaces.

Figure 5.22: Samples were placed between two tantalum sheets to prevent Ge evaporation.

Sample cross section in Figure 5.23 was characterized by a core in which several macropores can be observed and a dense skin due to pressure exerted by Ta sheet in upper surface and by sample own weight in bottom surface.

Figure 5.24(b) and 5.25(b) display the internal cross section shown at higher magnifications (800 x and 1600 x, respectively), in particular the difference between the internal sample part and surface can be clearly observed: sample surfaces were characterized by pores of different size as shown in Figure 5.24(a) and 5.25(a), which were formed by gas developed consequently to both PEG thermolysis and reaction 5.2.1 (i.e. hydrogen) while the internal cross section was characterized only by large pores. Such a inhomogeneity may be caused by several factors such as temperature gradients between the specimen core and surface during heat treatment, local germanium evaporation that formed bubbles, gas development that created big bubbles which remained trapped within the material, inhomogeneous reagents mixing.

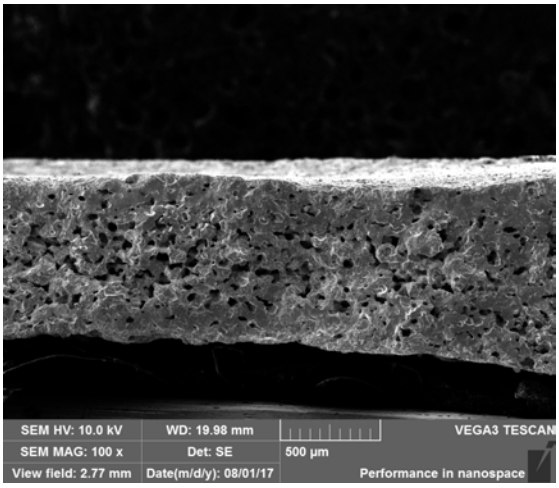

Figure 5.23: SEM micrograph sample cross section. MAG: 100 x

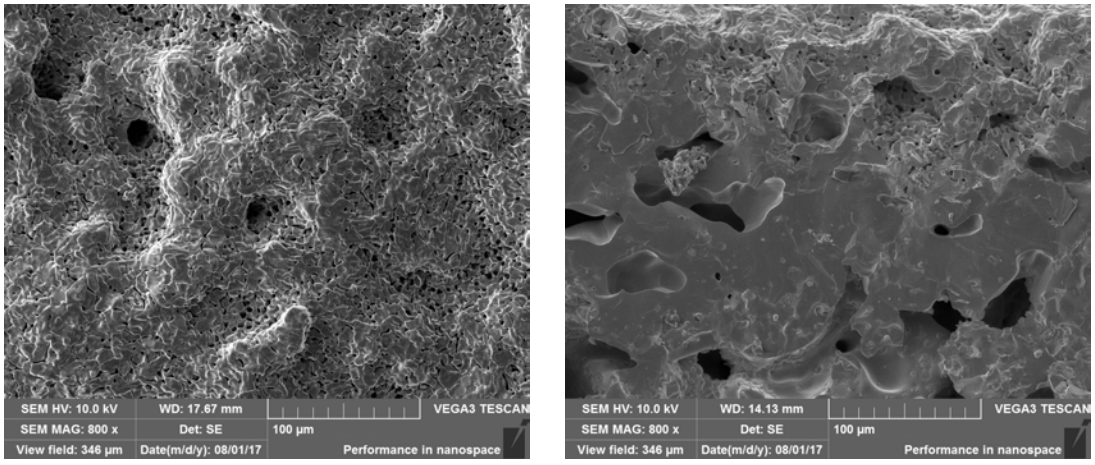

(a) Sample surface. (b) Sample internal cross section.

Figure 5.24: Comparison between surface and internal microstructures. MAG: 800 x.

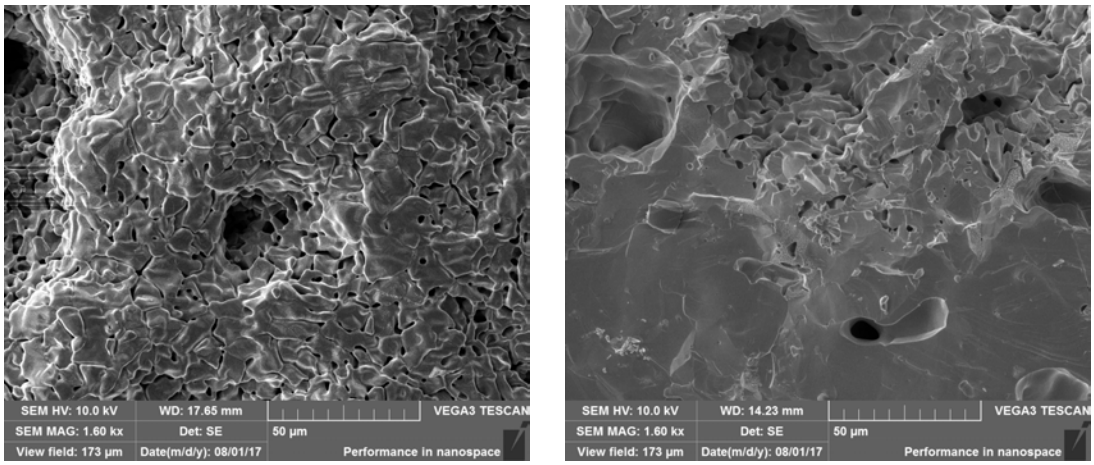

(a) Sample surface. (b) Sample internal cross section.

Figure 5.25: Comparison between surface and internal microstructures. MAG: 1600 x.

The XRD spectrum in Figure 5.26 shows the presence of Ge_4Zr_5, while only few peaks corresponded to ZrGe; the heat treatment maximum temperature was still too high to avoid germanium loss, thus phases containing less Ge than ZrGe were formed.
However, with respect to XRD pattern obtained by samples heat treated at T_{max} =1900 °C in Figure 5.21, Ge_3Zr_5 phase disappeared, which means that less germanium evaporated thanks to both lower temperatures and Ta sheet placed onto the sample upper surface.

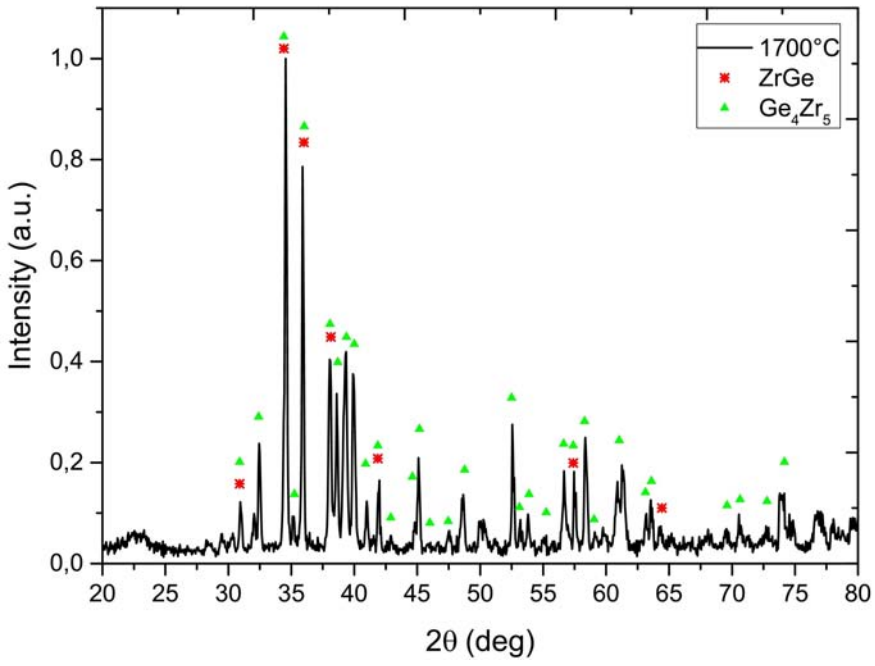

Figure 5.26: XRD analysis after heat treatment characterized by T_{max} =1700 °C.

5.2.3 T_{max} =1500 °C heat treatment effects

Ge evaporation was decreased undergoing samples at a heat treatment characterized by T_{max} =1500 °C. Figure 5.27 and 5.28 SEM micrographs show a less porous microstructure than the one obtained by previous heat treatments, indeed performing a heat treatment having a lower T_{max} led to reduce gas development caused by Ge evaporation; as a consequence, these samples were more mechanically resistant than than the previous ones, however some shape distortions occurred.
Moreover, in Figure 5.28(a) grain boundaries can be clearly observed, thus particles sintering occurred even at this temperature.

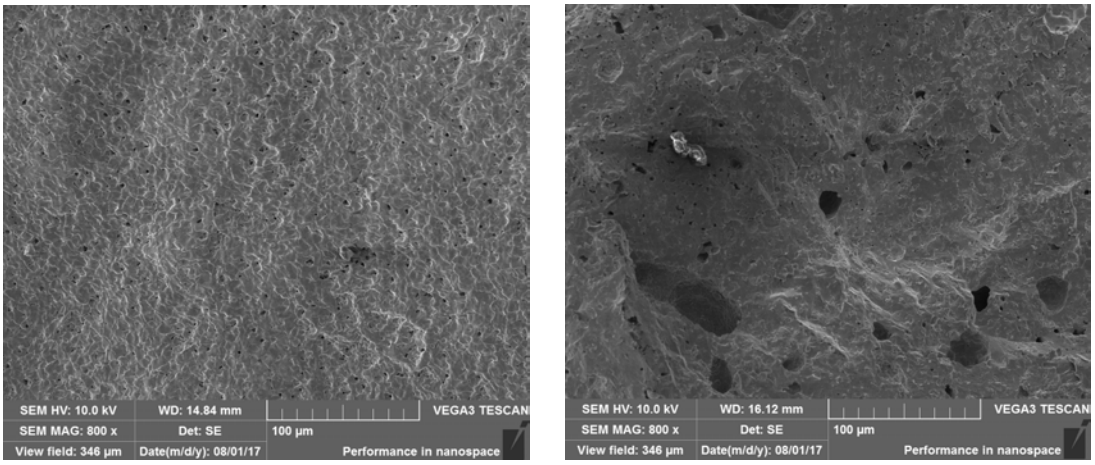

(a) Sample surface. (b) Sample internal cross section.

Figure 5.27: Comparison between surface and internal microstructures. MAG: 800 x.

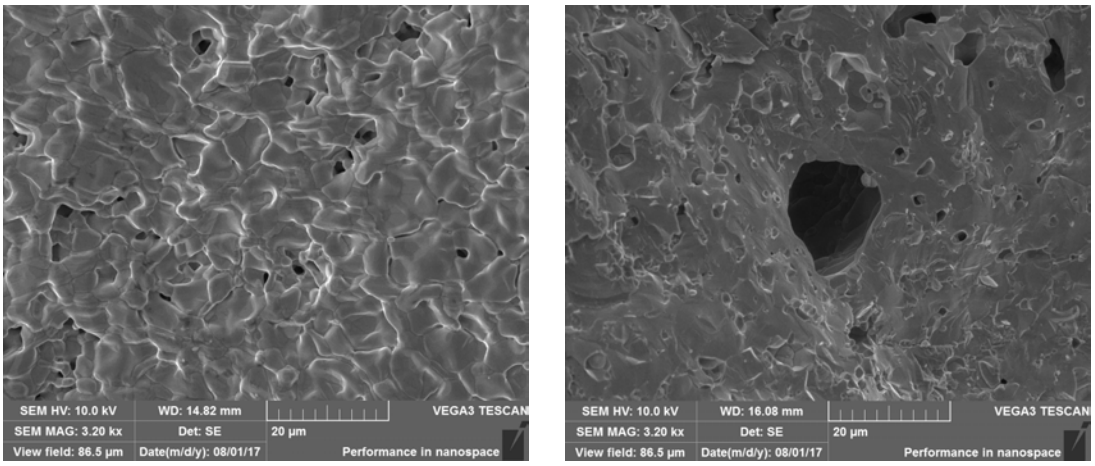

(a) Sample surface. (b) Sample internal cross section.

Figure 5.28: Comparison between surface and internal microstructures. MAG: 3200 x.

XRD pattern in Figure 5.29 shows the presence of peaks corresponding both to ZrGe and Ge_4Zr_5; in particular, with respect to XRD spectrum obtained by samples heat treated with T_{max} =1700 °C, new peaks attributable to ZrGe appeared.

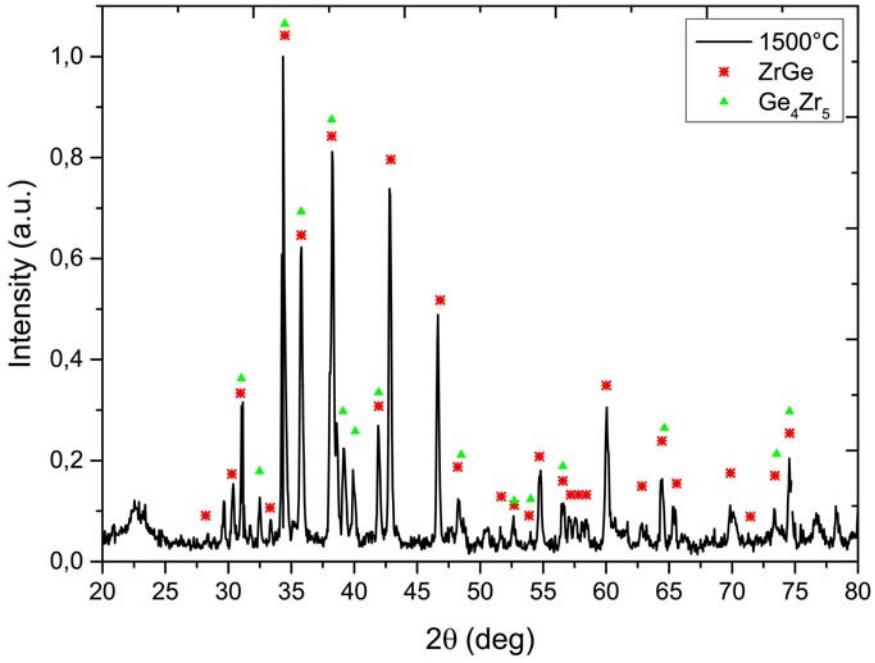

Figure 5.29: XRD analysis after heat treatment characterized by T_{max} =1500 °C.

5.2.4 T_{max} =1200 °C heat treatment effects

Figure 5.30 and 5.31 SEM micrographs obtained after T_{max} =1200 °C heat treatment show a dense surface (Figure 5.30(a) and 5.31(a)) and an internal cross section characterized by isolated pores (Figure 5.30(b) and 5.31(b)); whereby, microstructure resulted more dense than the one provided by heat treatment having T_{max} =1500 °C due likely to a lower Ge loss.

These samples were characterized by a higher mechanical resistance than the previous ones, however shape distortions occurred as well as for the other heat treatments.

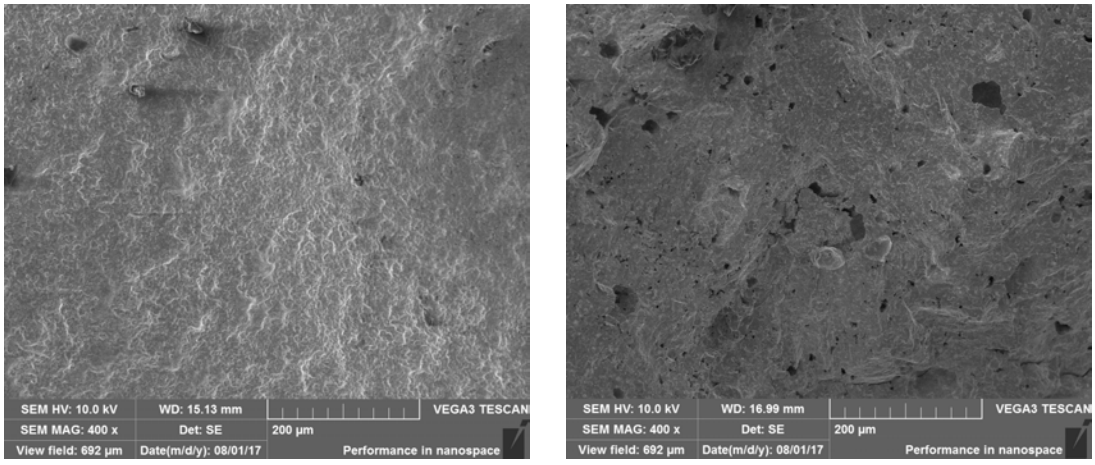

(a) Sample surface.

(b) Sample internal cross section.

Figure 5.30: Comparison between surface and internal microstructures. MAG: 400 x.

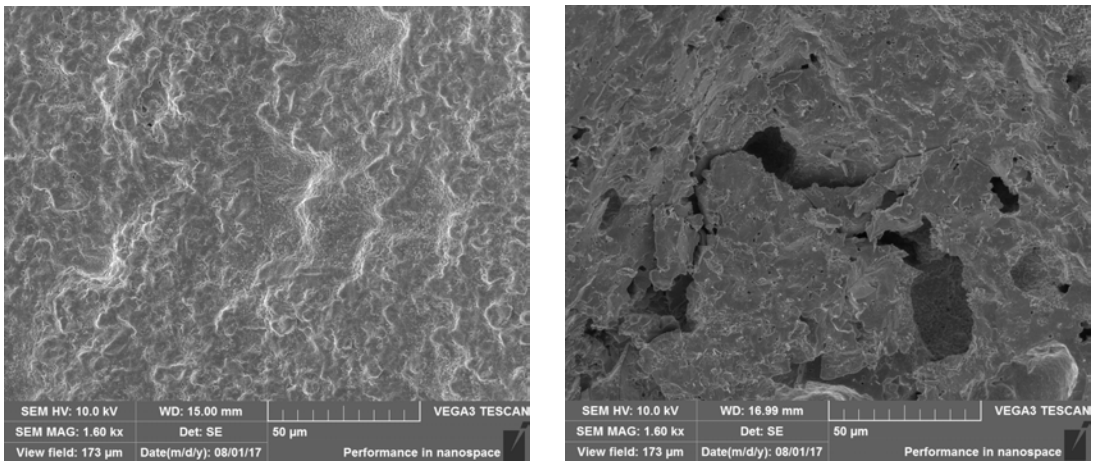

(a) Sample surface. (b) Sample internal cross section.

Figure 5.31: Comparison between surface and internal microstructures. MAG: 1600 x.

Figure 5.32 shows the XRD spectrum obtained after T_{max} =1200 °C heat treatment: the experimental pattern peaks corresponded exactly with ZrGe ones; Ge loss was reduced with respect to the other heat treatments, therefore the available germanium was enough to satisfy reaction 5.2.1 stoichiometery and to produce the desired zirconium germanide.

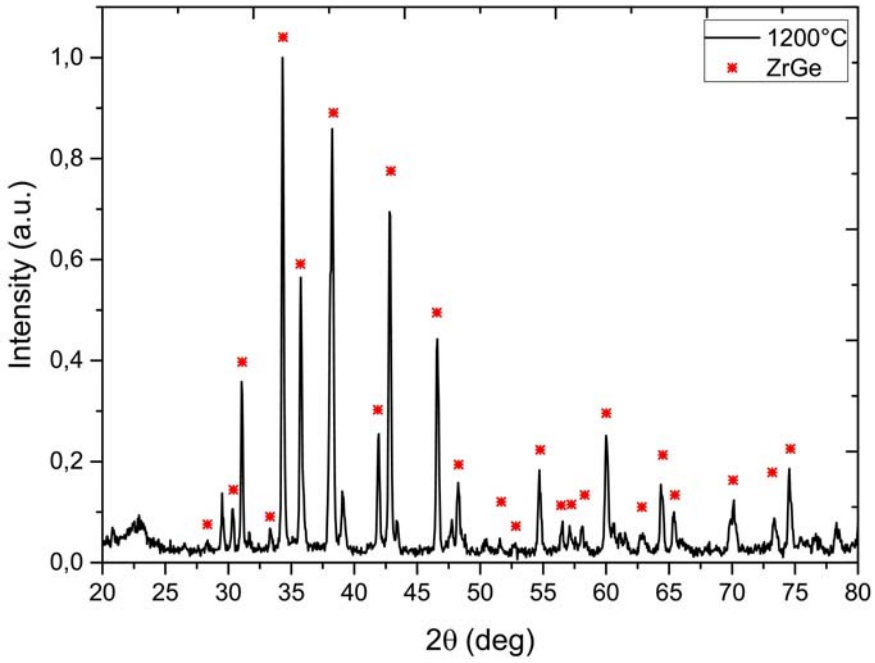

Figure 5.32: XRD analysis after heat treatment characterized by T_{max} =1200 °C.

5.3 Conclusions

Two different ZrGe synthesis methods were studied: the former was germanothermic reduction, while the latter was zirconium hydride method.

Germanothermic reduction could be realized using as precursors ZrO_2 and Ge, but it was not convenient: most of Ge loss was due to GeO formation (59,6%) which was a reaction 5.1.1 product, moreover another Ge fraction evaporated because of high temperatures required to react all ZrO_2. XRD analysis in Figure 5.14 revealed oxide presence even after a heat treatment at 1700 °C (Heat treatment 2 - 5.1.2), therefore to convert all the starting oxide, higher temperatures were necessary; however, it was not possible to increase the heat treatment temperature because further germanium evaporation would have lead to compounds characterized by a lower germanium content than ZrGe, such as Ge_3Zr_5 or Ge_4Zr_5.

Zirconium hydride method surely provided better results than the germanothermic reduction, indeed by heat treating pellets made of ZrH_2 and Ge at such a temperature that allowed reaction 5.2.1 without an excessive Ge loss, ZrGe was obtained.

Materials produced after heat treatments characterized by different maximum temperatures T_{max} were studied: decreasing T_{max}, microstructures resulted more dense, but Ge loss decreased providing compounds increasingly similar to ZrGe, indeed XRD analysis in Figure 5.32 revealed that by employing a proper heat treatment with T_{max} =1200 °C, ZrGe was produced.

Figure 5.33 collects samples average weight loss after heat treatments at different T_{max}, in particular the one obtained after T_{max} =1200 °C was very close to theoretical weight loss calculated from reaction 5.2.1 stoichiometry which was 3,2% of initial pellet weight (considering mixture composition 2 in Table 5.1).

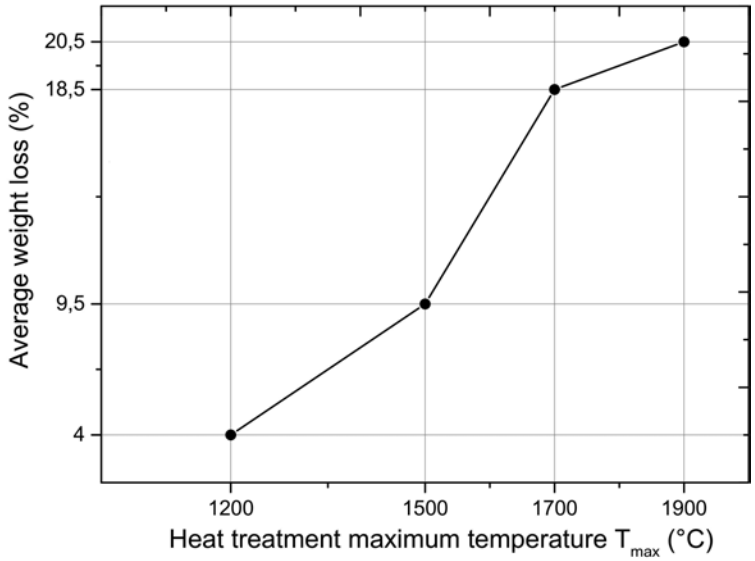

Figure 5.33: Average weight loss for heat treatments characterized different T_{max}.

After these considerations, reaction chamber pressure variations in Figure 5.16 can be better analyzed: since ZrGe was obtained using a T_{max} =1200 °C and its microstructure resulted dense, reaction 5.2.1 occurred likely in correspondence of maximum pressure increase before 1200 °C, i.e. between 450 and 750 °C; therefore, gas release for T>1200 °C is caused only by Ge evaporation that formed germanium poor compounds as Ge_3Zr_5 and Ge_4Zr_5 found in XRD spectra displayed by Figure 5.21 and Figure 5.26, 5.29, respectively.

The main problem of this process consisted of samples mechanical resistance before and after heat treatment: without a binder, samples broke during mold extraction, while using a binder that after heat treatment left low carbon residual such as PEG, its thermolysis and consequently gas development caused specimens deformation; whereby, in order to obtain a higher mechanical resistance, heat treated samples could be pulverized and re-processed using a proper binder.

CHAPTER 6

Titanium carbide SPES target produced by additive manufacturing

6.1 Introduction: additive manufacturing

Additive manufacturing (AM, also known as 3D printing) is considered an innovative technology for producing components with topologically optimized complex geometries as well as functionalities that are not achievable by traditional methods. The full potential of 3D printing can be realized by optimizing as well as possible the computational design tools, generic material feedstocks, techniques for monitoring thermomechanical processes under in situ conditions, and microstructural heterogeneity in order to minimize anisotropic static and dynamic properties.
Conventional AM processes have three fundamental limitations [38]:

1. low production rate ($< 30\ cm^3/min$);
2. the produced part are still small ($< 1000\ cm^3$)
3. The material feedstock is expensive.

However, significant improvements in speed, size, and cost can satisfy the requirements to use this technique in industrial applications.
In AM, materials in their basic form (such as powders, wires, and tapes) are transformed into a finished part through manipulation using different energy sources. These energy sources, including electrons, photons, plasma, and phonons, interact with the materials, leading to localized diffusion, melting, and high-strain-rate deformation to consolidate them. These interactions are often complex and might not yield the expected target properties, thus high-performance computing (HPC) tools are being developed to simulate and resolve many problems for instance

- localized melting with heat transfer in granular powder media;
- heat and mass transfer with abrupt temperature gradients and high liquid-solid interface velocities;

- microstructure evolution;
- thermomechanics.

In this work, the 3D Direct Ink Writing (DIW) technique was used to realize the first 3D structure-controlled targets made of titanium carbide, starting from a properly designed ink. The term "direct ink writing" describes fabrication methods that employ a computer-controlled translation stage, which moves a pattern-generating device, that is an ink-deposition nozzle, to create materials with controlled architecture and composition.[45, 44]
The adopted 3D printer (see Figure 6.1) to realize the desired 3D structures was the Delta Wasp 2040 Turbo®model (Wasproject, Massa, Lombardia, IT) which employed the Filament-Based Writing (FBW) approach [45]: the ink, which was contained inside a syringe, was continuously extruded through a fine cylindrical nozzle thanks to a lead screw, to create a filamentary element. The filament diameter was determined by the nozzle diameter, ink rheology, and printing speed.
In particular the fluid that accomplished the rheological requirements for the AM is the Bingham pseudoplastic one: when stressed beyond its yield point (τ_y) it exhibited shear thinning flow behavior, as described by:

$$\tau = \tau_y + K\,\dot{\gamma}^n \tag{6.1.1}$$

Where τ is the shear stress, n is the shear thinning exponent (< 1) and $\dot{\gamma}$ is the shear rate.
Through the control of ink composition, rheological behavior, and printing parameters, 3D structures that consisted of continuous solids, high aspect ratio (e.g., parallel walls), or panning (unsupported) elements can be produced. The latter structures offered the greatest challenge for designing inks, because they contained self-supporting elements that must bridge gaps in the underlying layers.
Like other layered manufacturing techniques, the design process started with the creation of a computer model of the component to be assembled. Then the model was sliced by a series of parallel planes with a fixed interplane spacing equivalent to the thickness of the layers that were printed. After slicing and calculation of tool paths for each layer, the 3D object was examined to identify whether support structures were needed, furthermore for spanning structures as well as the designed 3D TiC target, the tool-path spacing within individual layers must exceed the deposited filament width. The DIW design process therefore required:

1. The ability to assemble the desired structure;
2. Control over the three axis (x,y,z) for the appropriate spacing of the tool path (i.e., resolution);
3. Control over the rate of ink deposition;
4. Proper accounting for the dimensional and property changes that occur during post-deposition processes (i.e., drying, binder removal, and sintering).

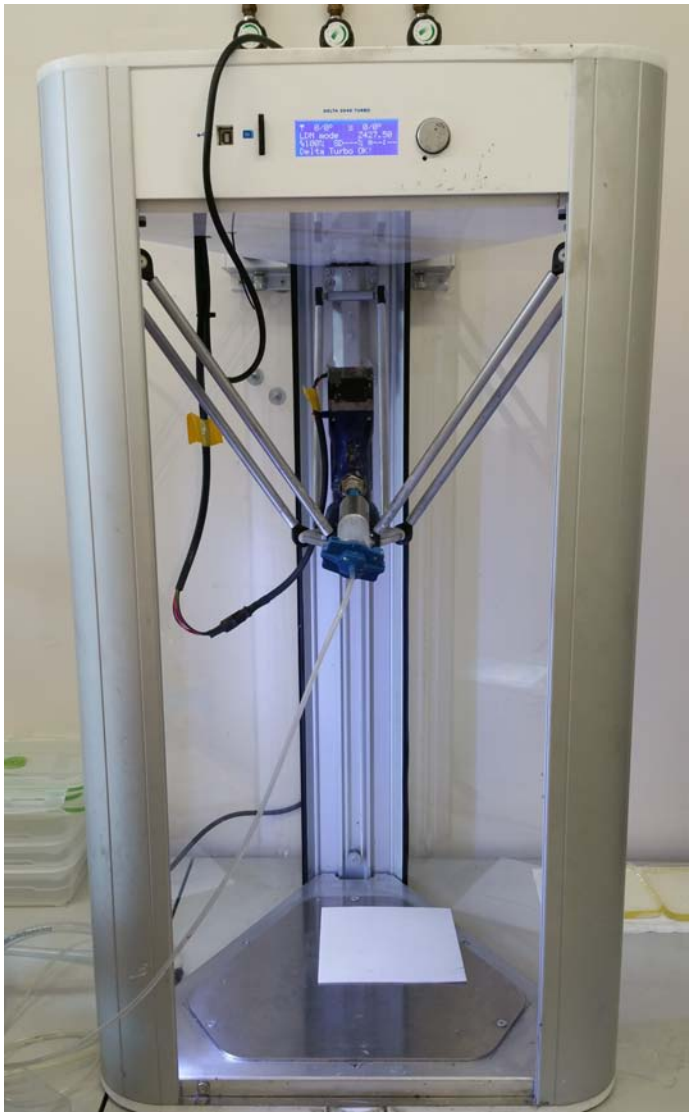

Figure 6.1: Delta Wasp 2040 Turbo®3D printer. It can reach an extruder speed of 1000 mm/s and a print volume of $200 \times 200 \times 400$ mm^3. Nozzles are usually made in polypropylene and their diameter ranges from 100 to 1500 μm.

The ink came out the nozzle as a continuous, rod-like filament with a rigid (gel) core-fluid shell architecture, which simultaneously promoted its shape retention while allowing the rods to fuse together at their contact points. Upon deposition, these filaments solidified first at their outer surface, and then radially through their core.

Ceramic green bodies produced via filamentary DIW contain varying amounts of binder and can be sintered to achieve the desired mechanical resistance and density.

6.2 Target production

The AM technique changes the way to design the SPES target: it allows the preparation of a target structure having a perfectly controlled macroporosity in order to enhance both the isotopes release and thermal dissipation. The material used for these new concepts is titanium carbide which ensures a high temperature resistance and provides the isotopes already discussed in Paragraph 3.2.2. The following paragraphs explain the 3D TiC targets production procedure.

6.2.1 Design

The 3D models were realized in SOLIDWORKS®and exported as mesh files (.stl); each mesh was then sliced using the add-on Slic3r contained in the printing software Repetier-Host and represented in Cartesian coordinates in the form of G-code. The slicing algorithm intersects the input mesh based on the layer height and develops a toolpath which includes information on the nozzle size, on the feed and on the flow rate. G-code files were checked and manually adapted in order to allow for continuous deposition of the filament.[28]
Three 3D models characterized by different patterns were generated and optimized for the 3D printer, thus they can be classified as follow:

- **TiC 3D normal**: The macropores are all perfectly aligned overlapping exactly the different layers (Figure 6.2);
- **TiC 3D 45°**: The layers are tilted of 45° with respect to each other (Figure 6.3);
- **TiC 3D shifted**: the structure is obtained shifting the layers with respect to each other (Figure 6.4);

All the targets were designed to have a diameter of about 30 mm and a thickness of $1,3$ mm which corresponded to 4 layers. In order to obtain this number of layer, a nozzle having 400 μm diameter must be used. The lattices geometrical porosity, calculated by SOLIDWORKS®, is about 55vol.%.

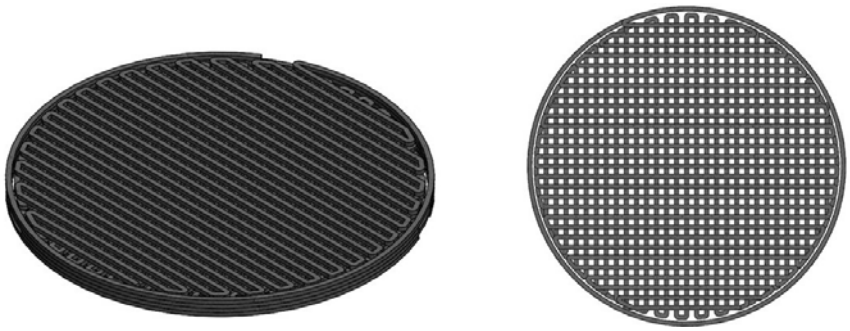

Figure 6.2: SOLIDWORKS®3D model of the normal pattern.

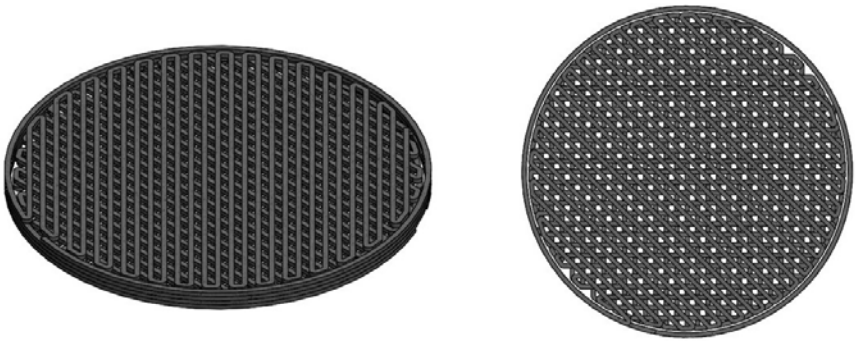

Figure 6.3: SOLIDWORKS®3D model of the 45° pattern.

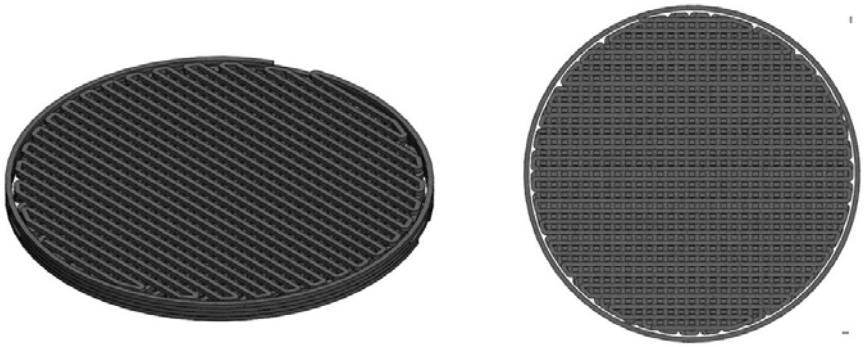

Figure 6.4: SOLIDWORKS®3D model of the shifted pattern.

6.2.2 Ink preparation

As explained previously, the ink rheology must be perfectly optimized to realize as well as possible the aforementioned structures, therefore the mixture preparation was fundamental.
The ink production can be divided in two steps: the former in which different ink compositions were studied in order to choose the one having the desired behavior; the latter was the refinement of the chosen composition, which means that small composition variations of the reagents were performed in order to optimize the printing stage.
Usually the inks employed for AM processes were constituted by ceramic powder ($50 \div 60\%$ in volume), organic additives ($< 1\%$) and volatile solvents as distilled water ($35 \div 50\%$). After several tests of different mixtures [67], the chosen one is represented in Table 6.1:

Table 6.1: Ink composition.

Reagent	Weight fraction %	Volumetric fraction %	Weight $[g]$	Volume $[cm^3]$
TiC powder	78,52	41,91	50	10,14
Distilled water	20,94	55,1	13,33	13,33
Methylcellulose	0,54	2,99	0,347	0,72

The TiC powder was characterized by a 44 μm granulometry acquired by Sigma Aldrich (Munich, Germany), while the methylcellulose A4C (Dow Chemical, Michigan, USA) was useful to achieve the desired ink rheology forming a gel structure typical of a pseudoplastic fluid. The ink preparation was done following these steps:

1. Heat the distilled water up to 90 °C to increase the methylcellulose solubility;
2. Add and mix the methylcellulose until to reach the ideal fluid consistence;
3. Add and mix all the TiC powder.

6.2.3 3D printing

Since this was the first time that this kind of ink was used to realize circular shaped spanning structures, the feed rate of the printer must be accurately calibrated: if it was too much, the extruded material did not maintain the shape because it collapsed under its own weight, while if the feed rate was too low, the provided material did not be enough to produce the desired shape.
The material was extruded onto a Teflon plate (see Figure 6.5(a)) which ensured a weak sample sticking. As shown in Figure 6.5(b) the specimen maintained perfectly its shape, thus the produced ink was suitable for this application.
The mechanical resistance of the newly printed samples (called “green”) was too low for their handling, therefore they must be dried for several hours.
Once the samples were dried, they were removed from the Teflon plate and subjected to weight, diameter and thickness measurement.

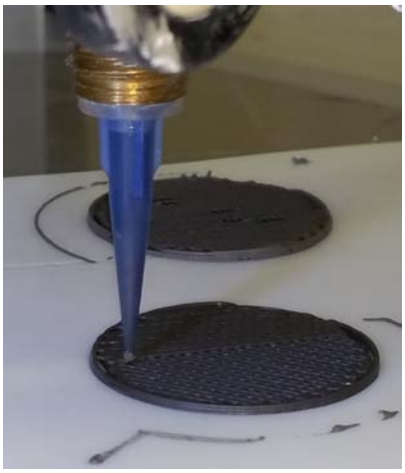

(a) The ink is extruded through the blue nozzle generating a 45° sample.

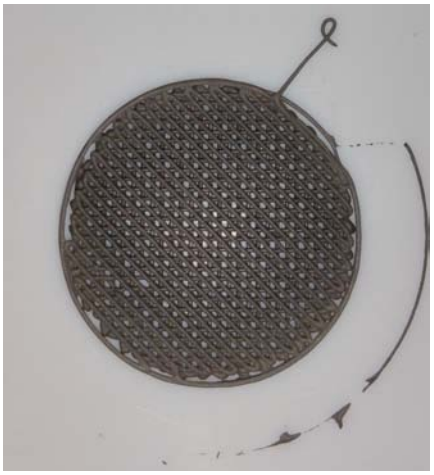

(b) The 45° green maintain its shape just after printing.

Figure 6.5: 45° specimen printing stage.

6.2.4 Heat treatment

Different heat treatments were tested for this mixture[1], however the one that provided better results is graphically represented in Figure 6.6 which consisted of three phases:

1. The specimens were kept in vacuum for about 1 hour at room temperature;
2. Heating (600 °C/h) up to 1800 °C, dwell time of 1,5 h at 1800 °C;
3. Cooling to room temperature (500 °C/h).

After the thermal treatment the samples acquired mechanical resistance thanks to sintering. Furthermore, Figure 6.7 graphically represents the pressure measured inside the vacuum chamber during the heating stage: the peak at about 650 °C was due to gas development caused by H_2O evaporation and methylcellulose decomposition.
The samples average dimensions and weight are collected in Table 6.2: the samples diameter was subjected to an isotropic decrease, the thickness increases were not statistically significant, while the mass losses were relatively low for all the three patterns.

Table 6.2: Average samples size (D=diameter, t= thickness) and mass (m) before treatment (b.t) and their variations after heat treatment.

Sample	m b.t. $[mg]$	Mass loss %	D b.t. $[mm]$	D reduction %	t b.t. $[mm]$	t increase %
Normal	1181	2	30,05	3	1,32	1
45°	1190	3	30,07	4	1,32	3
Shifted	1189	1	30,11	3	1,35	4

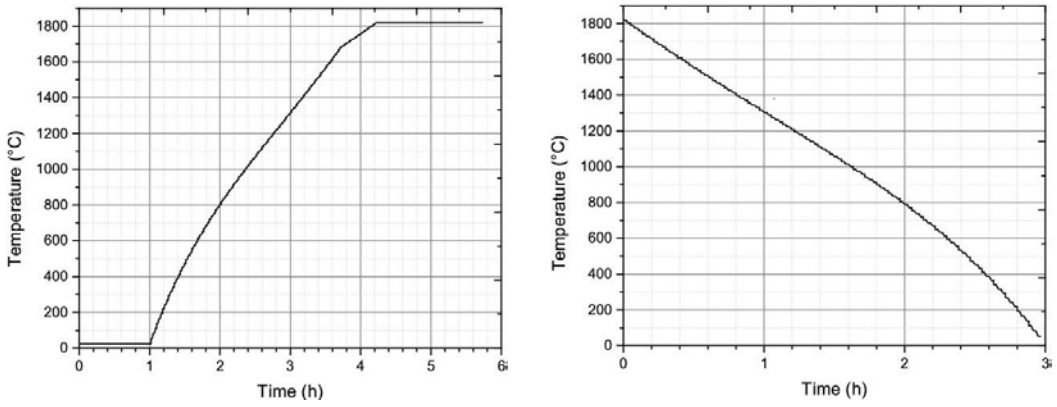

(a) Heating stage. (b) Cooling stage.

Figure 6.6: TiC 3D heat treatment.

[1]The specimens were heat treated under vacuum using the same system described in Paragraph 4.1.2.

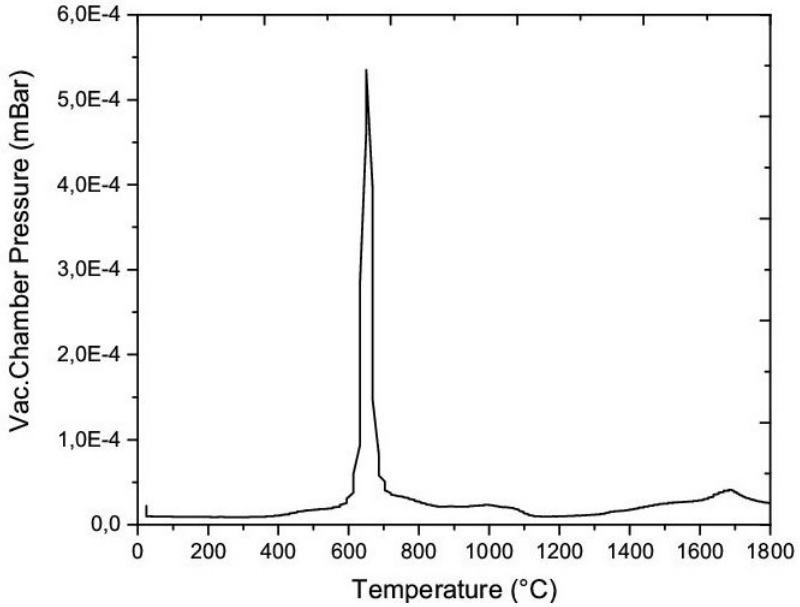

Figure 6.7: Vacuum chamber pressure measurement during the heating stage.

As shown in Figure 6.8 the TiC 3D targets synthesis was successful: after the heat treatment the specimens retained their shape and obtained a good mechanical resistance. The following paragraphs will provide more information concerning their microstructure, composition, permeability and porosity.

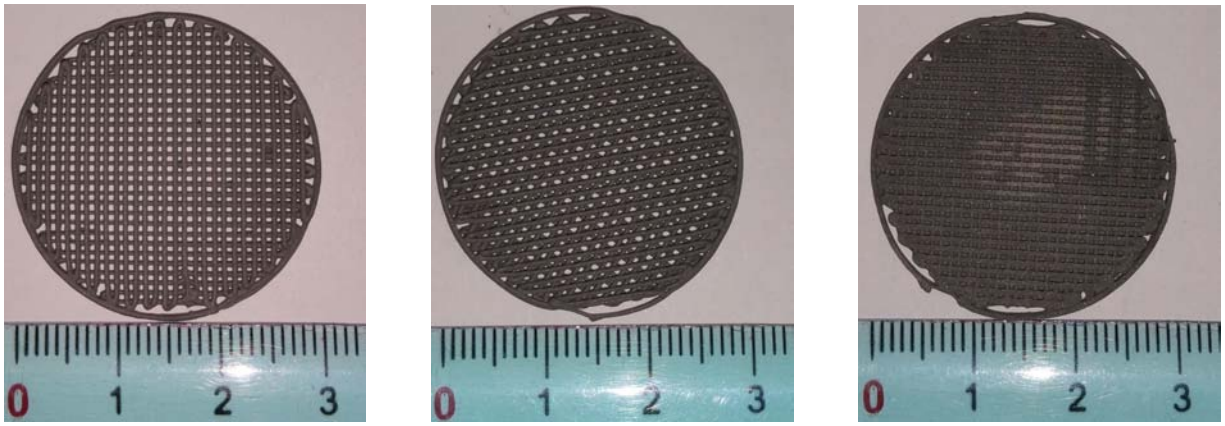

(a) TiC 3D normal. (b) TiC 3D 45°. (c) TiC 3D shifted.

Figure 6.8: 3D TiC targets having different patterns.

6.3 Microstructural analysis

The three different 3D patterns are clearly shown in Figure 6.9: macropores were well aligned in Figure 6.9(a), the tilting of 45° between two different layers can be appreciated in Figure 6.9(b) and the layers shifting was almost perfect in Figure 6.9(c). Furthermore the shifted structure was the only one which was characterized by a little swelling (collapse) where the layer intersection occurred. However the precision of the printing stage can be considered definitely satisfying. Increasing the magnification, the uniformity of the surface microstructure is observed in Figure 6.10. The presence of pores having a diameter less than 5 μm which is appreciated for this application can be observed in Figure 6.10(b) and 6.10(c); nevertheless the porosity analysis will be addressed in the following paragraphs. The grains were well packaged and their size distribution seems to be broad as shown in the internal pattern section in Figure 6.11. Moreover it presented a uniform microstructure as well as the pattern surface.

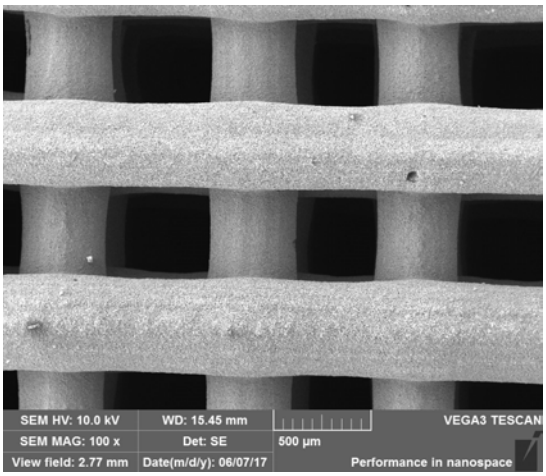

(a) TiC 3D normal.

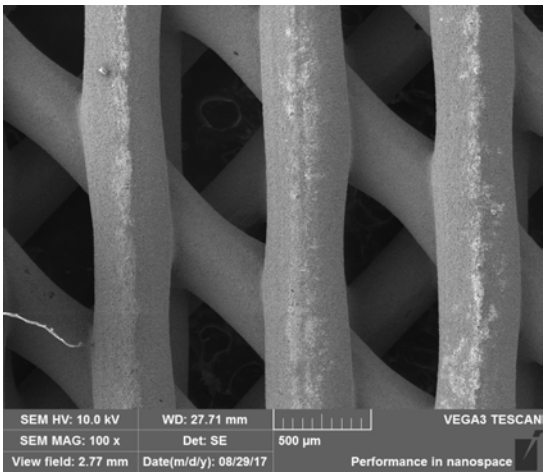

(b) TiC 3D 45°.

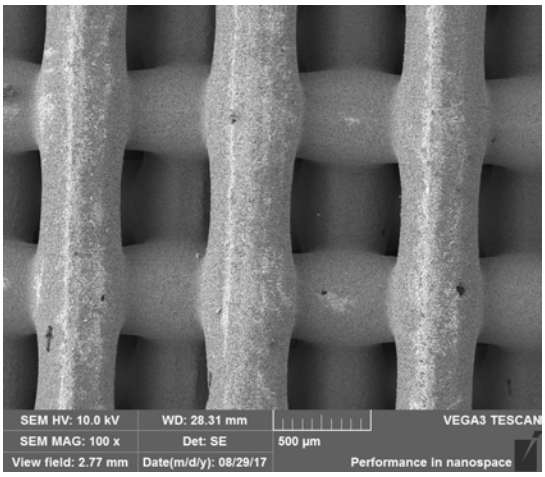

(c) TiC 3D shifted.

Figure 6.9: SEM images of TiC 3D patterns at 100 x.

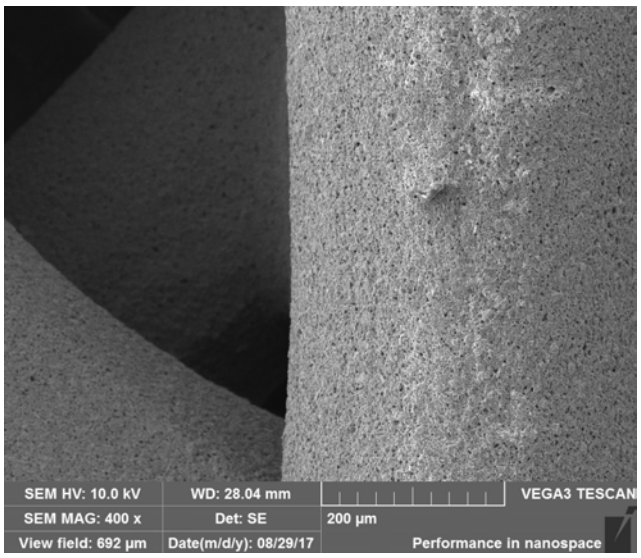

(a) 400 x.

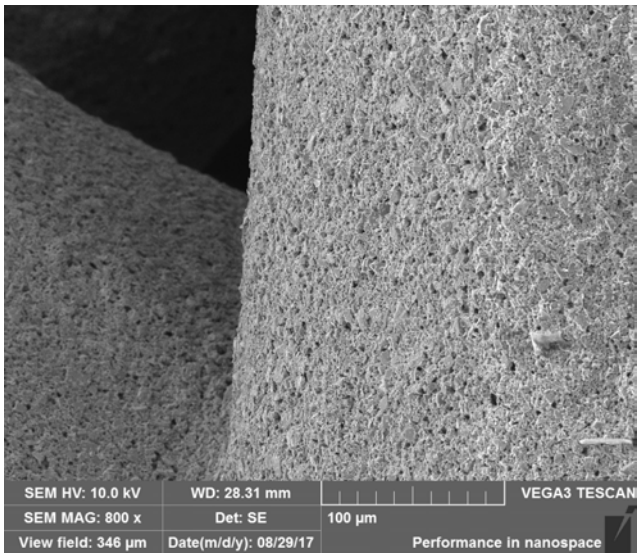

(b) 800 x.

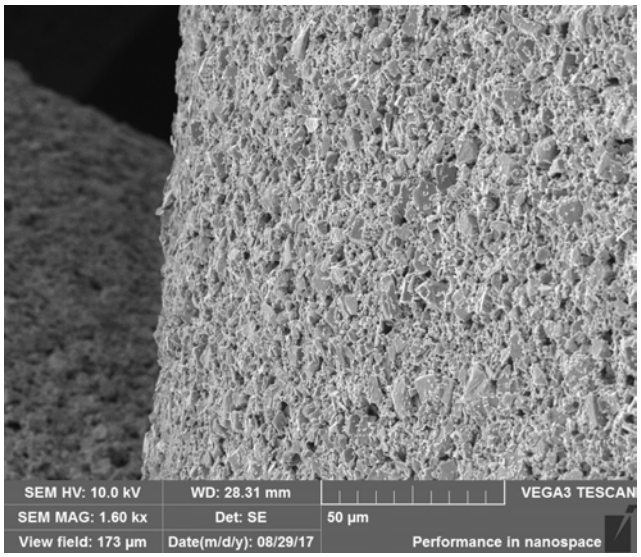

(c) 1600 x.

Figure 6.10: SEM images of TiC 3D pattern surface.

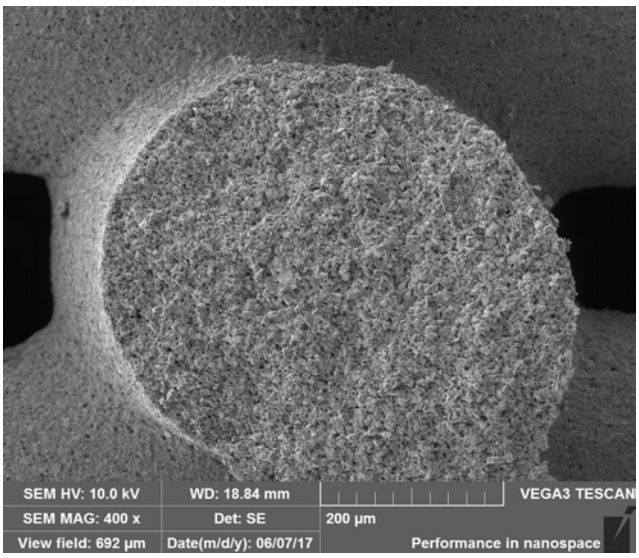

(a) 400 x.

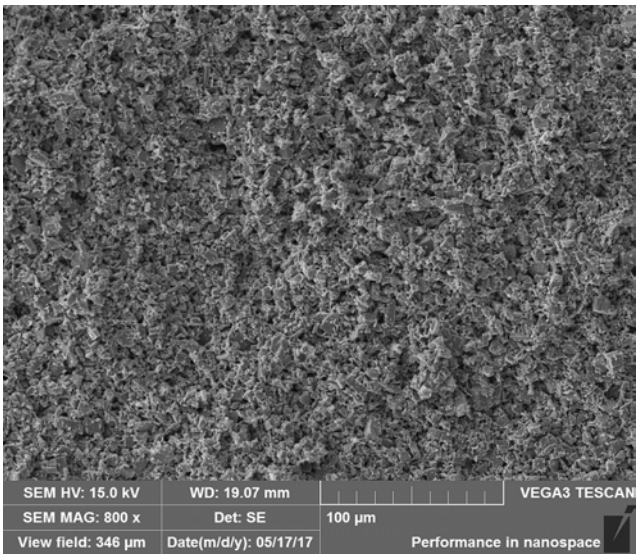

(b) 800 x.

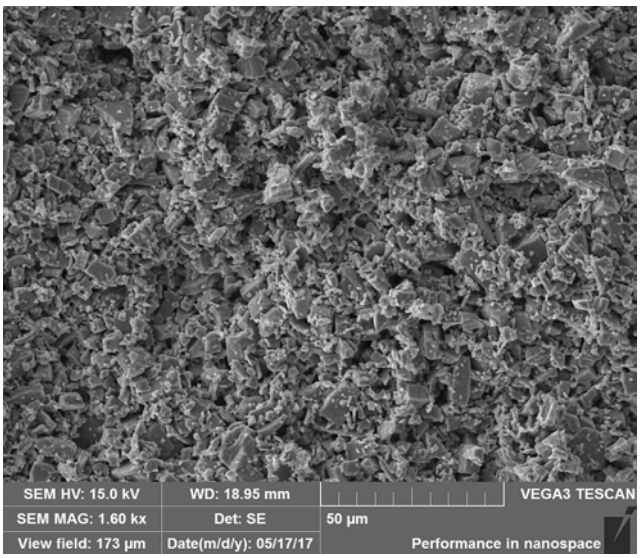

(c) 1600 x.

Figure 6.11: SEM images of TiC 3D internal pattern section.

Finally Figure 6.12 shows a comparison between the microstructure before and after the heat treatment. The relatively high heating rate and the low dwell time at 1800 °C did not permit the grain growth; sintering phenomena cannot be clearly observed, but the larger mechanical resistance after the heat treatment could be attributed to a certain grade of densification. Unfortunately the SEM used in this work lost resolution when magnification increased, thus this effect was not confirmed.

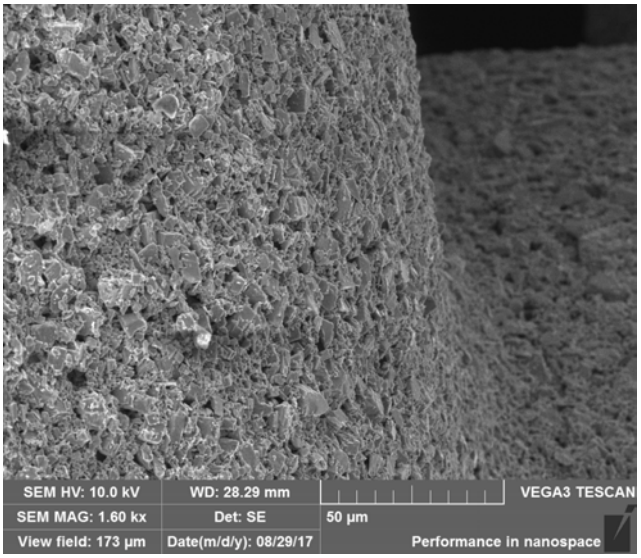

(a) Heat treated sample.

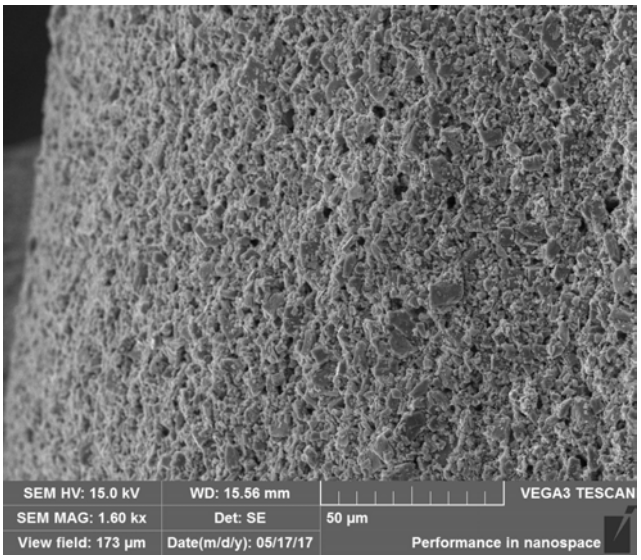

(b) As printed sample.

Figure 6.12: Microstructure comparison before and after the heat treatment. Both the SEM images were taken at 1600 x .

6.4 XRD analysis

Figure 6.13 shows the X-Ray diffractometer used in this work which is located at Padova University.

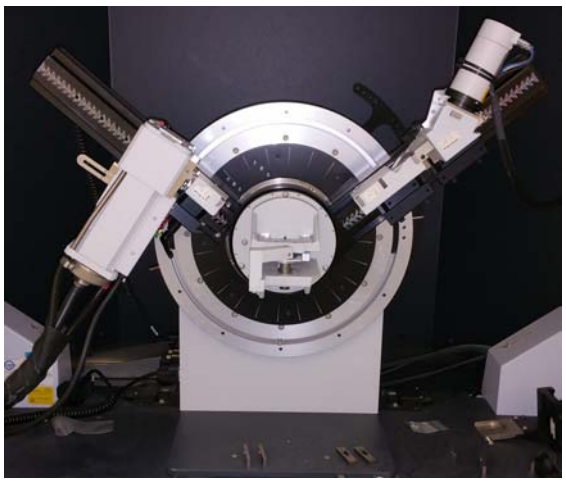

Figure 6.13: X-Ray diffractometer.

The XRD analysis observed in Figure 6.14 confirmed the presence of the single phase titanium carbide, therefore it was clear that the heat treatment in high vacuum did not permit the oxide formation.

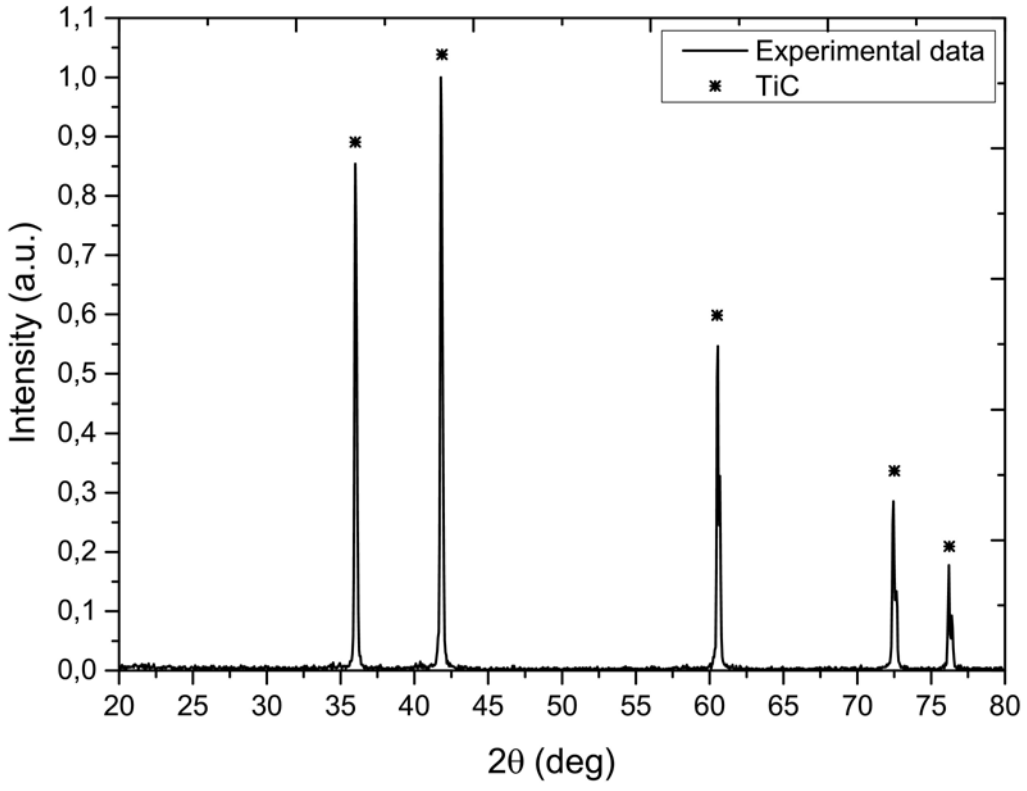

Figure 6.14: Experimental XRD pattern peaks correspond perfectly to titanium carbide ones.

6.5 Permeability

Permeability measures the capability of a fluid to pass through pores of a certain material. It indicates directly the presence or not of interconnected pores inside the material, thus it is fundamental to measure it in order to understand how the type of pattern realized for the TiC target influence the isotopes release. [35]

The Darcy Equation (6.5.1) indicates that the pressure gradient dP/dx $[Pa/m]$ inside the sample along the flow direction x is directly proportional to the input fluid velocity v $[m/s]$ which can be calculated from the ratio between the volumetric flow rate Q $[m^3/s]$ and the section of crossed material A $[m^2]$. The proportionality coefficient between dP/dx and v is the ratio between the fluid viscosity μ $[Pa\ s]$ and the k_1 $[m^2]$ which is called "*intrinsic (or Darcian) permeability of the medium*". The negative sign before the pressure gradient indicates that the fluid moves from the high-pressure region towards the low-pressure region.

$$-\frac{dP}{dx} = \frac{\mu}{k_1}\, v \tag{6.5.1}$$

Darcy's law is only valid for slow, viscous flow. Indeed for high flow rates which leads to a non-laminar regime, the pressure gradient calculated with the Equation (6.5.1) is lower than the experimentally measured one and the direct proportionality was not still valid.

The Forchheimer law 6.5.2 is able to account for the non-linear behavior of the pressure difference thanks to the Forchheimer (or inertial) term which is added to the first Darcy term. It takes takes into account the fluid density ρ $[kg/m^3]$ and the so-called "*inertial or non-darcian permeability*" k_2 $[m]$.

$$-\frac{dP}{dx} = \frac{\mu}{k_1}\, v + \frac{\rho}{k_2}\, v^2 \tag{6.5.2}$$

Coefficients k_1 and k_2 measure the medium permeability when the fluid passes through and they depend only on the structural properties of the porous medium.

Integrating (6.5.1) and (6.5.2) for compressible fluids (gas and vapor) is possible to obtain the Equations (6.5.3) and (6.5.4), respectively:

$$\frac{\Delta P}{L} = \frac{\mu}{k_1}\, v \tag{6.5.3}$$

$$\frac{\Delta P}{L} = \frac{\mu}{k_1}\, v + \frac{\rho}{k_2}\, v^2 \tag{6.5.4}$$

$$\Delta P = \frac{P_i^2 - P_o^2}{2P} \tag{6.5.5}$$

- P_i $[Pa]$ is the input pressure;
- P_o $[Pa]$ is the output pressure;
- P $[Pa]$ is the reference pressure (usually P_i or P_o);

- L $[m]$ is the thickness passed by the flow.

Furthermore the Forchheimer number Fo $[adm]$, defined by Equation (6.5.6), expresses effectively the ratio between the laminar flow and the turbulent flow through the ratio k_1/k_2. Therefore the Equation (6.5.4) can be rewritten in function of the Forchheimer number (6.5.7). Finally, after several mathematical steps, it is possible to calculate the ratio between the generated pressure gradient from the viscous forces or inertial forces with Equations (6.5.8) and (6.5.9), respectively.

$$Fo = \frac{\rho v}{\mu}\left(\frac{k_1}{k_2}\right) \tag{6.5.6}$$

$$\frac{\Delta P}{L} = \frac{\mu}{k_1} v(1 + Fo) \tag{6.5.7}$$

$$\frac{\Delta P_{viscous}}{\Delta P_{tot}} = \frac{1}{1 + Fo} \tag{6.5.8}$$

$$\frac{\Delta P_{inertial}}{\Delta P_{tot}} = \frac{Fo}{1 + Fo} \tag{6.5.9}$$

If $Fo >> 1$ the viscous effects are negligible, the flow regime is turbulent and $\Delta P_{tot} \approx \Delta P_{inertial}$, thus the Forchheimer equation can be approximated as follow:

$$\frac{\Delta P}{L} = \frac{\rho}{k_2} v^2 \tag{6.5.10}$$

Contrarily if $Fo << 1$ the flow regime is laminar, so approximately $\Delta P_{tot} \approx \Delta P_{viscous}$ and the Darcy's law remains valid. It is clear that the fluid movement through the medium is really different respect to the isotopes motion within the pores which occurs in molecular regime, thus are the coefficients k_1 and k_2 still significant under the extreme conditions of temperature and pressure occurring inside the SPES target? [14]

The aforementioned equations are based on the Navier-Stokes assumption which considers the fluid a Newtonian continuum[2]. This hypothesis is not satisfied for rarefied gas whereby the mean free path[3] λ $[m]$ (6.5.11) is comparable with pore size d_p $[m]$, so the particles collides more frequently with the pore wall than each other. This is defined as molecular flow and it is controlled by quantum mechanics effects [37].

$$\lambda = \frac{k_b T}{\sqrt{2}\pi\sigma^2 p} \tag{6.5.11}$$

- k_b is the Boltzmann constant;
- T is temperature;
- p is the gas pressure;

[2]Considering the fluid as a continuum means that is not made up of discrete particles but rather a continuous substance.

[3]The mean free path is the average distance traveled by a moving particle between successive collisions.

- $\sigma\ [m^2]$ is the effective cross-sectional area for spherical particles.

The Knudsen number $K_n\ [adm]$ calculated as follow, needs to understand if the system can be considered as a continuum or a molecular flow:

$$K_n = \frac{\lambda}{d_p} \tag{6.5.12}$$

If $K_n > 10$ the regime is molecular, while if $K_n < 0,1$ the continuum fluid condition is valid. The Figure 6.15 shows the difference between the target working conditions and the permeability measurement conditions.

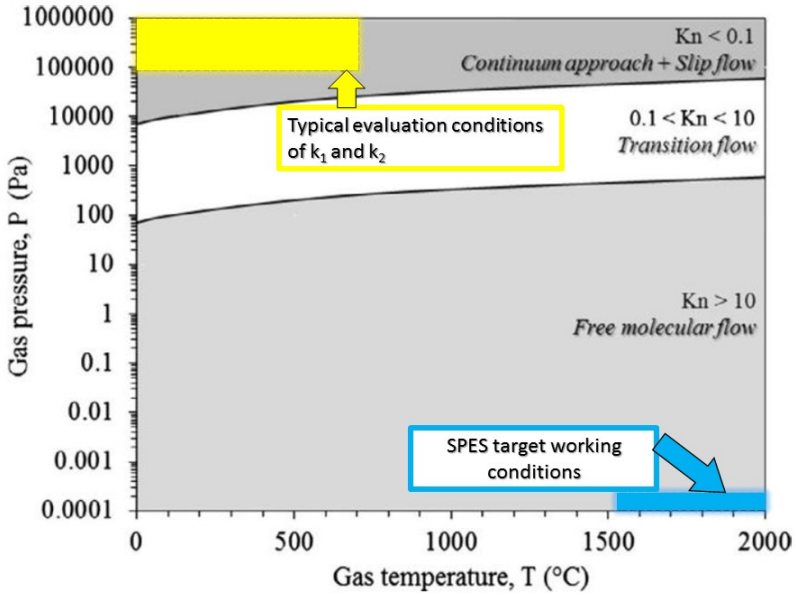

Figure 6.15: Difference between target working conditions and permeability measurement conditions.[14]

However the permeability measurement remains valid to measure the interconnection degree of pores; Hy et al.[34] and Mella[47] demonstrated that the interconnection is a factor which can be used to qualify the isotopes release from the target.

6.5.1 Permeability measurement

The test consists in forcing a certain fluid (in this case air, but either argon or helium could be used) through the porous sample in stationary flow condition. In Figure 6.16 the experimental apparatus which was used is shown. The fluid cross section $A\ [m^2]$ and the mean thickness $L\ [m]$ of the specimen must be measured before the experiment, while during the test the pressure variation between the gas entry and exit $(P_i - P_o)\ [Pa]$ and the volumetric flow rate $Q\ [m^3/s]$ can be registered by a digital manometer and a rotameter, respectively. Therefore during the experiment different values of Q and $(P_i - P_o)$ can be collected which are used to calculate the flow velocity v

and ΔP using Equations (6.5.13) and (6.5.5).

$$v = \frac{Q}{A} \tag{6.5.13}$$

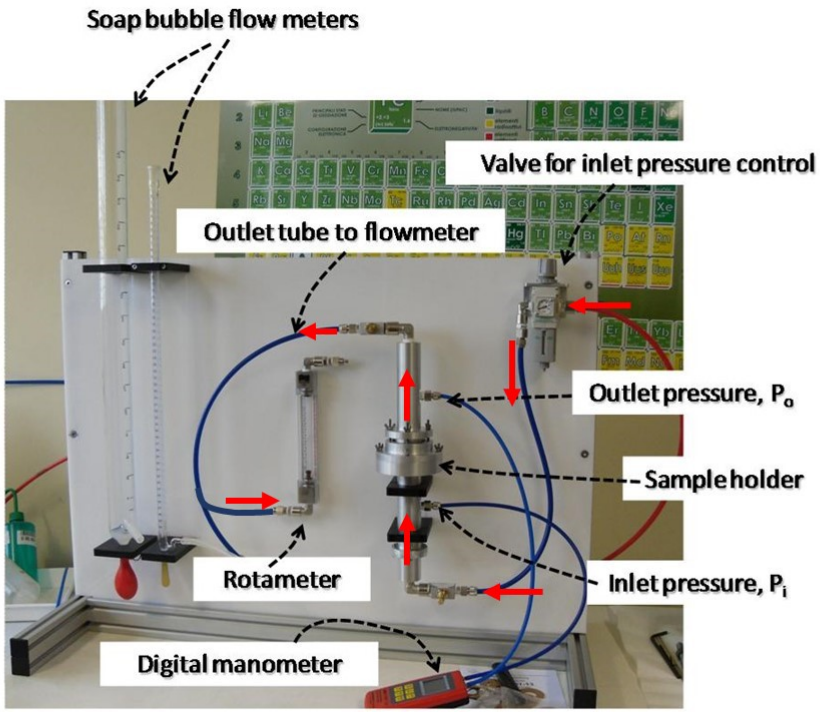

Figure 6.16: The experimental apparatus used for the permeability measurement located in LNL-INFN has been designed by Prof. M.D.M. Innocenti.

The obtained values are then inserted in a graph ΔP vs. v as shown in Figure 6.17. Thanks to a fitting with a parabolic curve that represents the Forchheimer equation (6.5.4), it is possible to get the coefficients a and b that are related to k_1 and k_2, respectively:

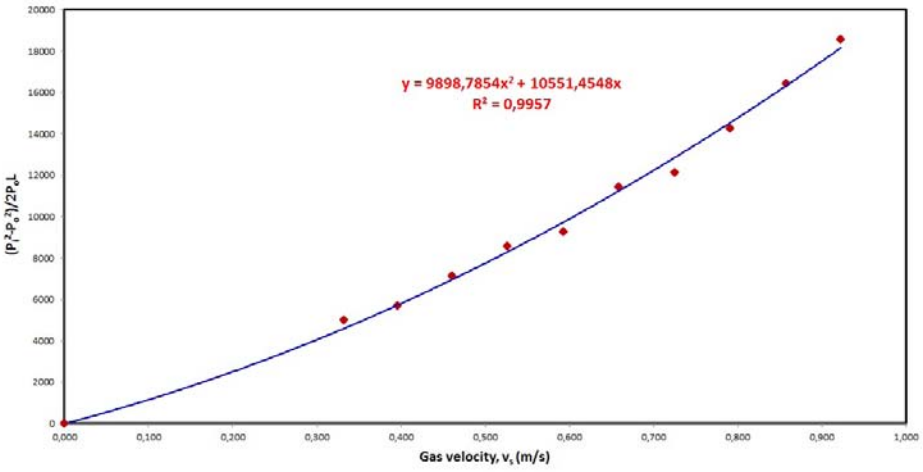

Figure 6.17: Through the ΔP vs. v curve fitting, the coefficients k_1 and k_2 can be determined.

$$\frac{\Delta P}{L} = av + bv^2 \tag{6.5.14}$$

$$k_1 = \frac{\mu}{a} \tag{6.5.15}$$

$$k_2 = \frac{\rho}{b} \tag{6.5.16}$$

The variation of μ $[Pa \cdot s]$ and ρ $[g/cm^3]$ with temperature is respectively given by the empirical Equations 6.5.17[4] and 6.5.18:

$$\mu = \mu_0 \left(\frac{T+273}{273}\right)^{1,5} \left(\frac{273+C_n}{T+273+C_n}\right) \tag{6.5.17}$$

$$\rho = \frac{PM}{R}\frac{P_0}{T+273} \tag{6.5.18}$$

- $\mu_0 = 1,73 \cdot 10^{-5}\ Pa \cdot s$ is an empirical constant,
- T [°C] is the output gas temperature;
- $C_n = 125$ is an empirical constant;
- $P_0 = 759,3\ mmH$ is the atmospheric pressure;
- $R = 62,364\ l \cdot mmHg/K \cdot mol$ is the gas constant.

Moreover it is possible to predict k_2 thanks to Equation (6.5.19) which was obtained empirically taking into account the fitting of many experimental data collected in the graph in Figure 6.18.

$$k_{2,pred} = \exp\left(-\frac{1,71588}{k_1^{0,08093}}\right) \tag{6.5.19}$$

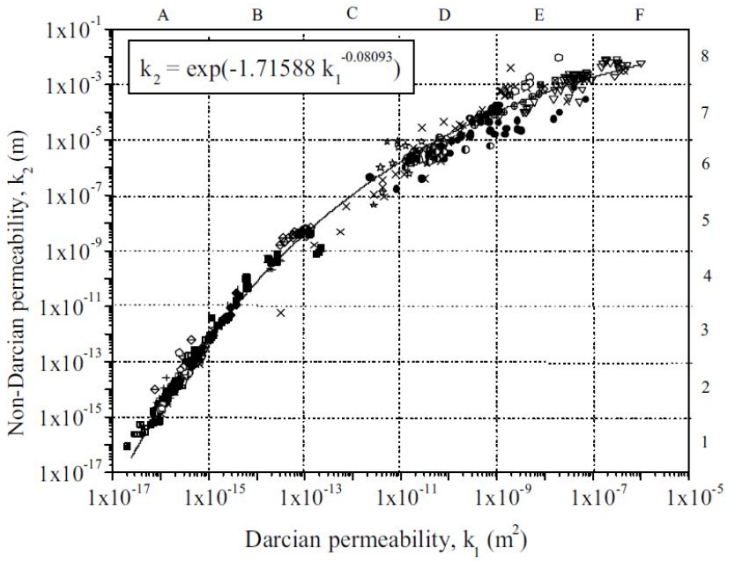

Figure 6.18: Empirical correlation between k_1 and k_2.

As aforementioned, the experimental apparatus in Figure 6.16 was used for the permeability of 3D TiC target measurement: the air flow path is indicated by the red arrows, thus first it passes

[4]It is called *Sutherland equation*: for each gas, μ_0 $[Pa \cdot s]$ and C_n $[adm]$ are given for a certain temperature range.

through the valve which needs to control the inlet air pressure. Then it reaches the sample holder which is shown in Figure 6.19. It consists of a hollow cylindrical tube in which are placed following this order:

1. Hollow plastic support (see Figure 6.19(c));
2. Two rubber rings with a circular hole having a diameter $D = 14\ mm$ (see Figure 6.19(c));
3. Sample, opportunely prepared;
4. Other rubber rings having the same hole diameter until to fulfill the sample holder.

(a) Sample holder parts fixed with the clamp.

(b) Internal hollow part of the sample holder.

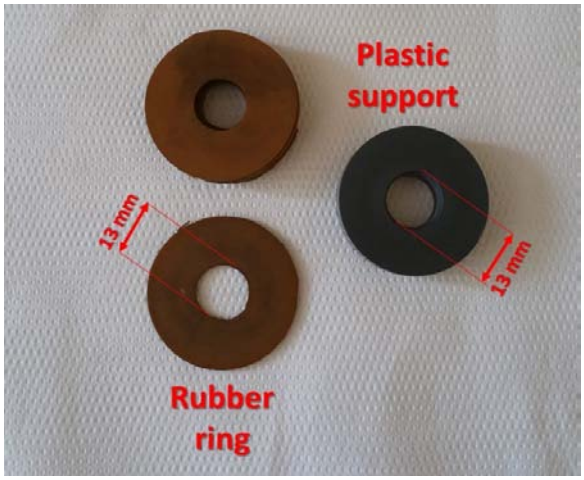

(c) Plastic support and rubber rings.

Figure 6.19: Sample holder apparatus.

The sample preparation is not really complicated, but it requires some attentions: the sample boundary must be covered by both Teflon and graffer's tape as shown in Figure 6.20 in order to avoid the air reflux inside the material which causes the abnormal variation of the outlet pressure. Moreover the upper and the bottom faces of the specimen must not be touched during its handling.

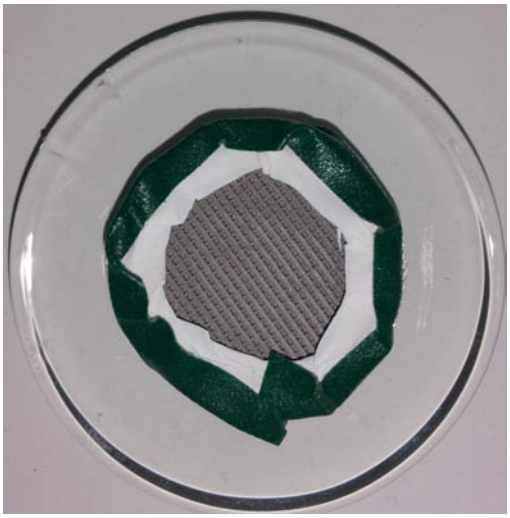

Figure 6.20: TiC 3D sample preparation for a permeability measurement.

The top part of the sample holder is fixed thanks to a clamp (see Figure 6.19(a). The rubber rings define a cross section of the gas during the measure, furthermore they seal the sample avoiding eventually flux leakage and they adsorb the pressure of the top part of the sample holder which could cause the sample fracture.
Finally the gas flux reaches the rotamereter, which is an instrument opportunely calibrated to measure the volumetric flow rate.

6.5.2 Results

The permeability measure was done for the three kind of pattern (normal, 45° and shifted) realized for the 3D target. For each pattern three sample was analyzed in order to get an average measure of the coefficients k_1, k_2 and $k_{2,pred}$. The measure started controlling the inlet gas pressure thanks to the valve on the top right of Figure 6.16: increasing the gas pressure, the volumetric flow rate read from the rotameter increased as well. Thanks to the digital manometer, the pressure variation between the inlet and the outlet gas can be registered. For instance the following Table 6.3 contains the data collected from the permeability measurement of one of the samples having the normal pattern.
Each of these values was helpful to calculate the gas velocity v and $\Delta P/L$: the former was obtained with the relation (6.5.13) taking into account that the gas crossed a circular section of $D = 14\ mm$ given by the rubber rings, the latter was calculated dividing by the sample thickness L the Equation (6.5.5).

Table 6.3: Example of data collecting for the permeability measurement.

$Q\ [l/min]$	$(P_i - P_o)\ [mBar]$
2,5	0,03
3	0,03
3,5	0,04
4	0,04
4,5	0,05
5	0,06
5,5	0,06
6	0,07
6,5	0,08
7	0,09

In this way was possible to get for each analyzed specimen the graph $\Delta P/L$ vs. v; in particular in Figure 6.21 were represented the curves which belonged to samples having the three different 3D patterns realized in this work.

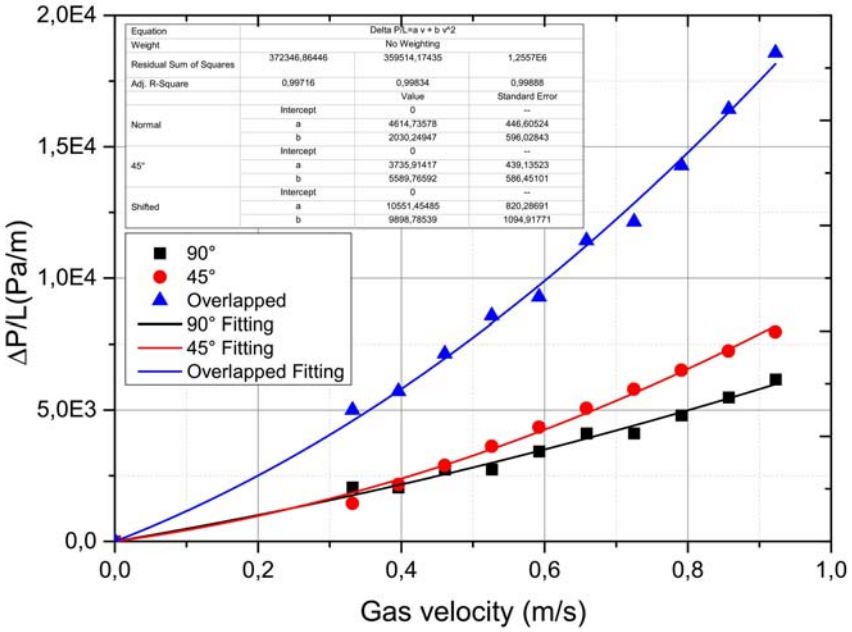

Figure 6.21: Permeability comparison between the three different structure.

Therefore the obtained points must be fitted using the Equation (6.5.14) in order to get the a and b coefficients and consequently k_1 and k_2 employing the relations (6.5.15) and (6.5.16), respectively. Analyzing the graph in Figure 6.21 was clear that the pressure drop changed between the three pattern: the normal structure had all the macropores aligned and it was more permeable than the others, as expected. The 45° lattice ensured a pressure drop slightly larger than the normal one,

while the $\Delta P/L$ in the shifted structure was the highest, consequently it was the less permeable. k_1, k_2 and $k_{2,pred}$ for each 3D structure are collected in the following three tables, while the average values of k_1 and k_2 are represented in Figure 6.22.

Considering that the geometrical porosity was about the same for all the three patterns, the one which provided the lowest k_1 and k_2 coefficients was the shifted lattice, as expected. The coefficients comparison between the 45° and normal structures was surprising: the former had a coefficient k_1 slightly larger than the latter, conversely when the layers were tilted of 45° with respect to each other the coefficient k_2 was smaller the structure having the pores all the aligned; moreover the experimental data of these two structures collected in the $\Delta P/L$ vs v graph occupied almost the same region, thus the fitted curves were close to each other. This confirmed that the 45° pattern had almost the same permeability of the normal pattern.

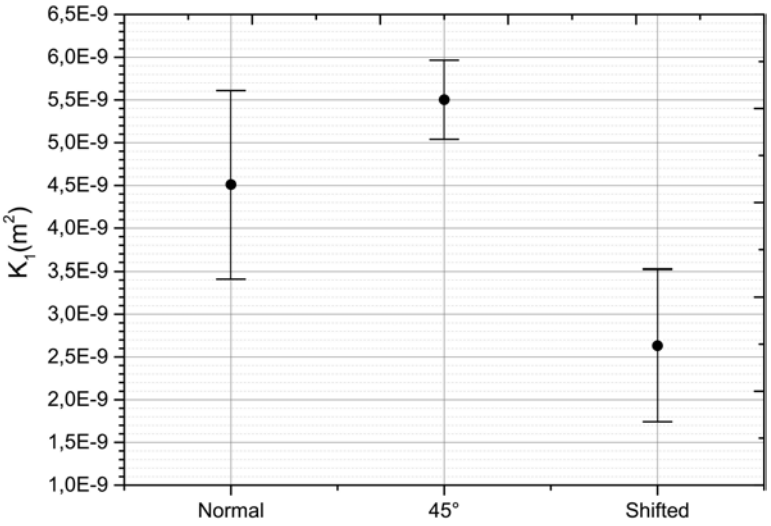

(a) k_1 average values for the different 3D patterns.

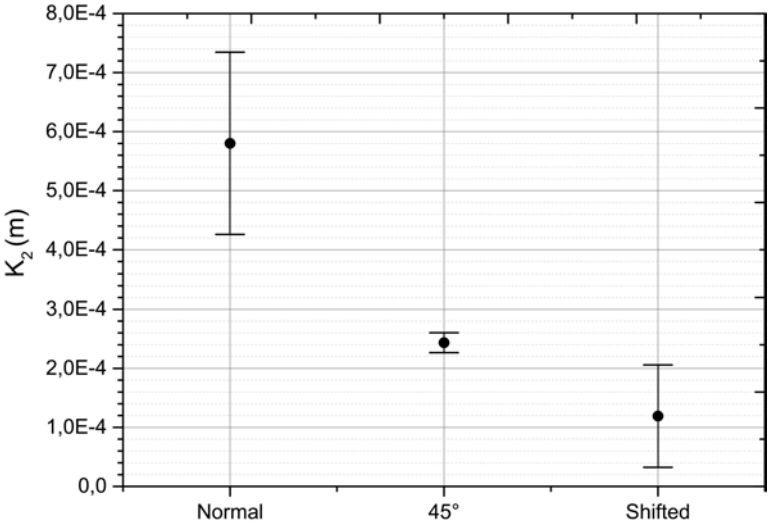

(b) k_2 average values for the different 3D patterns.

Figure 6.22: K_1 and k_2 average measured values with error bars.

Table 6.4: k_1, k_2 and $k_{2,pred}$ measurement for the normal pattern.

Pattern	normal			
Measure	1	2	3	Average
k_1	$5,77 \cdot 10^{-09}$	$3,73 \cdot 10^{-09}$	$4,04 \cdot 10^{-09}$	$4,83 \cdot 10^{-09}$
k_2	$2,94 \cdot 10^{-04}$	$5,37 \cdot 10^{-04}$	$5.80 \cdot 10^{-04}$	$3,45 \cdot 10^{-04}$
$k_{2,pred}$	$3,47 \cdot 10^{-04}$	$2,60 \cdot 10^{-04}$	$3,15 \cdot 10^{-04}$	$3,08 \cdot 10^{-04}$

Table 6.5: k_1, k_2 and $k_{2,pred}$ measurement for the 45° pattern.

Pattern	45°			
Measure	1	2	3	Average
k_1	$4,98 \cdot 10^{-09}$	$5,66 \cdot 10^{-09}$	$5,87 \cdot 10^{-09}$	$5,50 \cdot 10^{-09}$
k_2	$2,11 \cdot 10^{-04}$	$2,35 \cdot 10^{-04}$	$2,43 \cdot 10^{-04}$	$2,30 \cdot 10^{-04}$
$k_{2,pred}$	$3,15 \cdot 10^{-04}$	$3,43 \cdot 10^{-04}$	$3,51 \cdot 10^{-04}$	$3,36 \cdot 10^{-04}$

Table 6.6: k_1, k_2 and $k_{2,pred}$ measurement for the shifted pattern.

Pattern	Shifted			
Measure	1	2	3	Average
k_1	$3,35 \cdot 10^{-09}$	$2,59 \cdot 10^{-09}$	$1,77 \cdot 10^{-09}$	$2,63 \cdot 10^{-09}$
k_2	$5,89 \cdot 10^{-04}$	$1,72 \cdot 10^{-04}$	$1,19 \cdot 10^{-04}$	$1,93 \cdot 10^{-04}$
$k_{2,pred}$	$2,52 \cdot 10^{-04}$	$2,03 \cdot 10^{-04}$	$1,56 \cdot 10^{-04}$	$2,04 \cdot 10^{-04}$

Finally the $k_{2,pred}$ values calulated with Equation (6.5.19) were always comparable with the experimentally measured ones. This fact is confirmed by the graph in Figure 6.23 in which the measured experimental average values of k_1 and k_2 (colored spots in the top right) were added: they were placed very close to the ones represented by the aforementioned correlation (6.5.19).

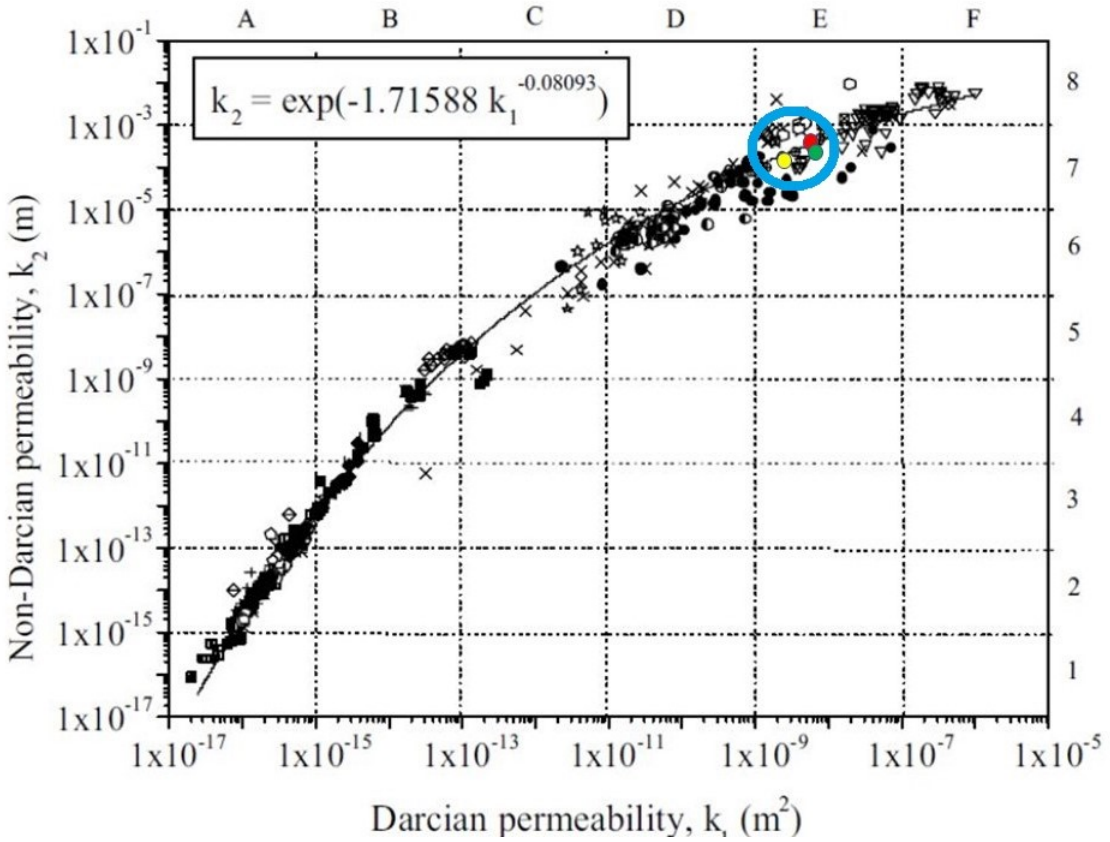

Figure 6.23: The obtained experimental data are close to the interpolation curve represented by Equation (6.5.19).

6.6 Conclusions

Structure-controlled targets made of titanium carbide were successfully realized, starting from a properly designed ink, through Direct Ink Writing (DIW) 3D printing technique.
Three kind of 3D structures characterized by different patterns having about 55vol.% porosity were firstly designed by CAD software SOLIDWORKS®and then realized thanks to Delta Wasp 2040 Turbo®3D printer.
The ink was designed by mixing in a proper way and quantities (Table 6.1) distilled water, methyl-cellulose and titanium carbide having a particle size lower than 44 μm ; it was suitable to produce these kind of structures in which even self-supporting elements were present and newly printed samples retained their shape after printing stage and drying, furthermore they had a mechanical resistance high enough to allow their handling and measurements. After that they were subjected to a heat treatment that further increased their mechanical resistance thanks to sintering.
SEM micrographs highlighted the precision of the printing in obtaining uniform microstructures in both samples surface and internal cross sections.
Permeability measurement was identified in previous works as a valid test to determinate pores interconnection degree which is a factor which can be used to qualify the isotopes release from the target even if permeability measurement conditions were very far from target working conditions (Figure 6.15), therefore the three different produced patterns were compared; in particular, shifted structure resulted to be the less permeable, while 45° and normal patterns were characterized by about the same permeability. However, 3D targets produced in this work presented k_1 and k_2 values that were about 4 and 3, respectively, order of magnitude higher than the ones already obtained by lanthanum carbide LaC_x targets which production was characterized by the burnout of polymeric sacrificial fillers to increase and tailor porosity [8].

CHAPTER 7

Conclusions and perspectives

SPES is a project of INFN aimed to develop an ISOL facility for the production of Radioactive Ion Beams in one of the four national laboratories of INFN, LNL.
Radioactive isotopes production will be achieved by nuclear reactions inside a properly designed target thanks to the interaction with a primary proton beam provided by an already installed cyclotron; the produced species will be then extracted from the target, ionized, mass separated and sent to different experimental areas, in which they will be employed for nuclear physics research, as well as other applications in different branches of science.
The SPES production target must be able to sustain extreme environmental conditions of pressure and temperature imposed to maximize isotopes production and release, without be subjected to damage, outgassing or undergoing degradation of its thermo-mechanical properties. Therefore, its material choice and design assume a key role for the whole project.
In this thesis, three ceramic targets materials were produced and characterized performing SEM, EDS, XRD, permeability and physisorption analysis.

ZrC_x targets made of zirconium carbide characterized by the presence of excess foil-shaped graphite to increase isotopes release were successfully produced by carbothermal reduction by reacting at high temperature zirconia (ZrO_2) and graphite.
Heat treatments to produce both 13 *mm* and 30 *mm* ZrC_x targets were properly designed to get a uniform microstructure in which the excess carbon was well distributed in both the sample surface and internal cross section; moreover, precursors were completely transformed into products composed by ZrC and C without the presence of residual oxide.
Nevertheless, physisorption analysis did not provide satisfying results concerning the surface area and the pores morphology which are both helpful for isotopes release.
In future, porosity would be enhanced by producing targets using polymeric fibers as sacrificial

fillers in order to create more pores and increase targets permeability as already done for LaC_x; moreover, carbon nanotubes (CNTs) will be used as an alternative carbon source with respect to graphite: the employ of CNTs is motivated by the fact that past investigations made on lanthanum carbide demonstrated that their use produced highly porous samples possessing high specific surface area (30 m^2/g, instead of 1,6 m^2/g for standard LaC_x) and consequently interconnected pores in the micro ($d < 2\ nm$) and meso ($2\ nm < d < 50\ nm$) range.

Zirconium germanide synthesis was characterized by several issues that were described in this work.

The first production method tested was the germanothermic reduction one in which zirconia and germanium powders were reacted to produce ZrGe and GeO (gaseous); after the first heat treatment, samples reacted with the graphite plate which was used as a sample holder inside the furnace reaction chamber, thus this problem was solved fixing a tantalum sheet onto the graphite plate.

The following heat treatment was performed at a maximum temperature of 1700 °C, but it was not high enough to transform all the starting ZrO_2 which remained as residual oxide within the final material; moreover, the mass loss during the heat treatment was about 10% larger than the theoretical one, in particular it was attributable to germanium evaporation due to its high vapor pressure at such a temperature. Therefore, the heat treatment maximum temperature temperature cannot be increased to complete germanothermic reaction because it would lead to further Ge evaporation, consequently germanium poor phases would be created; furthermore, the use of a germanium excess was not a convenient solution considering its expensiveness.

ZrGe was successfully obtained by the second production method presented in this work, in which zirconium hydride and germanium powders were reacted to produce ZrGe and hydrogen; because of literature missing information regarding the ideal heat treatment temperature, several heat treatment characterized by different maximum temperatures were performed and the different obtained materials were analyzed.

The first heat treatment, in which the maximum temperature was 1900 °C, gave samples having the bottom surface in contact with the tantalum sheet composed by zirconium and germanium, and the upper “free” surface constituted by only zirconium; therefore, Ge evaporated through the samples upper surfaces producing germanium poor phases as confirmed by the XRD analysis, but the tantalum sheet placed below the bottom surface was capable to avoid Ge evaporation.

Ge evaporation from the sample upper surface was avoided by placing specimens between two tantalum sheets and decreasing the heat treatment maximum temperature, indeed ZrGe was obtained by the heat treatment characterized a maximum temperature of 1200 °C.

The main problem of this production method was the pellets integrity, in fact they broke during

mold extraction even using PEG as a binder to increase their mechanical resistance; moreover, increasing the pellets PEG content was harmful for samples since gas development by PEG thermolysis during heat treatments caused specimens deformations.
Therefore, in future, new binders must be studied: the ideal one must provide a pellet mechanical resistance high enough to allow specimen handling without leaving contamination due to its thermolysis after heat treatment. Moreover, ZrGe produced samples were characterized by a dense microstructure, thus, controlling the heat treatment parameters, it would be possible to get a larger porosity value to increase isotopes release.

It was the first time in SPES project history that additive manufacturing (AM) technique was employed to produce circular shaped targets. They were realized with three different patterns characterized by about the same geometrical porosity in order to evaluate their permeability which is a property related to isotopes release.
Thanks to a permeability measurement it was established that 3D printed samples were several order of magnitude more permeable than other "standard" samples produced using the same production method employed for ZrC_x targets previously discussed (carbothermal reduction).
AM production method precision was stunning, indeed several specimens characterized by the same shape and size were successfully produced. Moreover, the production rate, that is a fundamental requirement for industrial applications, was much more larger than the standard process one.
For further improvements, a new ink composed by TiC powders having a particle size lower than the one employed in this work (44 μm) will be developed to obtain a final microstructure with a smaller grain size that will enhance the target release properties.
Since AM process was characterized by many advantages such as precision, versatility and high production rate, other inks composed by other materials will be designed, making this technique the most promising for SPES targets production.

Bibliography

[1] http://www.bestcyclotron.com/product_70p.html. (Cited at page 8)

[2] https://timeline.web.cern.ch/the-laser-ion-source-rilis-is-developed. (Cited at page 10)

[3] https://www.eurisol.org. (Cited at page 4)

[4] http://www.nuclear-power.net/nuclear-power/fission/. (Cited at page 22)

[5] https://web.infn.it/spes/. (Cited at page 6)

[6] J.S. Al-Khalili. An introduction to halo nuclei. In *The Euroschool Lectures on Physics with Exotic Beams, Vol. I*, 2004. (Cited at page 18)

[7] A. Andrighetto, M. Manzolaro, A. Monetti, S. Corradetti, F. Borgna, N. Realdon, D. Scarpa, M. Lollo, F. Pasquato, M. Rossignoli, M. Ballan, D. Conventi, G. Prete and. Gramegna, L. Biasetto, R. Oboe, P. Nicolosi, G. Meneghetti, P. Colombo, A. Tomaselli, M. Guerzoni, R. Michinelli, A. Margotti, I. Cristofolini, E. Mariotti, M. Ferrari, , and A. Zenoni and. The SPES ISOL-RIB unit. Technical report. (Cited at page 8)

[8] Caterina Anelli. Impiego di fibre polimeriche lunghe per la sintesi di target refrattari ad alta porosità e permeabilità per il progetto SPES, 2015. (Cited at page 137)

[9] J.R.J. Bennett. Delays in thick targets. *Elsevier*, 2002. (Cited at page 23)

[10] C. Benvenuti. Molecular surface pumping : the getter pumps. In *CAS - CERN Accelerator School : Vacuum Technology*, 1999. (Cited at page 28)

[11] L.M. Berger, W. Gruner, E. Langholf, and S. Stolle. On the mechanism of carbothermal reduction processes of TiO_2 and ZrO_2. *International Journal of Refractory Metals and Hard Materials*, 1999. (Cited at pages 54 and 55)

[12] L. Biasetto, P. Zanonato, S. Carturan, P. Di Bernardo, P. Colombo, A. Andrighetto, and G. Prete. Lanthanum carbide-based porous materials from carburization of lanthanum oxide and lanthanum oxalate mixtures. *Elsevier*, 2008. (Cited at page 46)

[13] L. Biasetto, P. Zanonato, S. Carturan, P. Di Bernardo, P. Colombo, A. Andrighetto, and G. Prete. Developing uranium dicarbide–graphite porous materials for the SPES project. *Elsevier*, 2010. (Cited at pages 46 and 65)

[14] L. Biasetto, M. Innocentini, W.S. Chacon, S. Corradetti, S. Carturan, P. Colombo, and A. Andrighetto. Gas permeability of lanthanum oxycarbide targets for the SPES project. *Elsevier*, 2013. (Cited at pages 46, 127 and 128)

[15] R. S. Biryukova and O. I. Popova. Preparation of transition metal germanides. *Soviet Powder Metallurgy and Metal Ceramics*, 1984. (Cited at pages 57, 93 and 94)

[16] Dario Bisello, Andrea Candelori, Natalia Dzysiuk, Juan Esposito, Pierfrancesco Mastinu, Serena Mattiazzo, Gianfranco Prete, Luca Silvestrin, and Jeffery Wyss. Neutron production targets for a new single event effects facility at the 70 MeV cyclotron of LNL-INFN. *Elsevier*, 2012. (Cited at page 5)

[17] Jane R. Blackford. Sintering and microstructure of ice: a review. *Elsevier*, 2007. (Cited at page 32)

[18] F. Borgna, M. Ballanb, S. Corradetti, A. Monetti E. Vettorato, M. Rossignoli, M. Manzolaro, D. Scarpa, U. Mazzia, N. Realdon, and A. Andrighetto. A preliminary study for the production of high specific activity radionuclide for nuclear medicine obtained with the isotope separation on line technique. *Elsevier*, 2017. (Cited at page 11)

[19] P. G. Bricault, M. Dombsky, P. W. Schmor, and A. Dowling. High power targets for ISOL radioactive ion beam facility. In *Proceedings of the 2003 Particle Accelerator Conference*, 2003. (Cited at page 28)

[20] V.P. Bulychev, R.A. Andrievskii, and L.B. Nezhevenko. Theory and technology of sintering, thermal, and cemicothermal treatment process. *Poroshkovaya Metallurgiya*, 1976. (Cited at page 54)

[21] L.C. Carraz, S. Sundell, H.L. Ravn, M. Skarestad, and L. Westgaard. High-temperature carbide targets for fast on-line mass separation of alkali and noble gas elements. *Elsevier*, 1979. (Cited at page 27)

[22] S. Carturan, M. Tonezzer, L. Piga, P. Zanonato, P. Colombo, A. Andrighetto, L. Biasetto, P. Di Bernardo, G. Maggioni, F. Gramegna, and G. Prete. Synthesis and characterization of lanthanum dicarbide-carbon targets for radioactive ion beams generation via the carbothermal reaction. *Nuclear Instruments and Methods in Physics Research Section A*, 2007. (Cited at page 46)

[23] Stefano Corradetti. Produzione e caratterizzazione di carburi porosi per il progetto SPES, 2009. (Cited at pages 59, 62 and 65)

[24] Stefano Corradetti. *Study and development of high release refractory materials for the* SPES *project*. PhD thesis, 2013. (Cited at pages 39, 44, 45, 46, 48 and 62)

[25] M. Dombsky, P. Bricault, T. Hodges, A. Hurst, and P. Schmor. Online isotope separation at ISAC with a 10 μ A proton driver beam. *Elsevier*, 2002. (Cited at page 28)

[26] P. Van Duppen. The euroschool lectures on physics with exotic beams. In *Isotope Separation On Line and Post Acceleration*, 2006. (Cited at pages 8 and 21)

[27] Valentin Fedosseev, Katerina Chrysalidis, Thomas Day Goodacre, Bruce Marsh, Sebastian Rothe, Christoph Seiffert, and Klaus Wendt. Ion beam production and study of radioactive isotopes with the laser ion source at ISOLDE. *Journal of Physics G*, 2017. (Cited at page 9)

[28] Giorgia Franchin. *Additive Manufacturing of Ceramics*. PhD thesis, 2017. (Cited at page 116)

[29] G. Gilmore. *Pratical Gamma-ray Spectroscopy*. John Wiley & Sons, 2008. (Cited at page 3)

[30] R. W. Harrison and W. E. Lee. Processing and properties of ZrC, ZrN and ZrCN ceramics: a review. *Advances in Applied Ceramics*, 2016. (Cited at pages 53 and 55)

[31] A.C. Hayes. Applications of nuclear physics. Technical report, Theoretical Division, Los Alamos National Laboratory, Los Alamos, New Mexico, 87545, USA. (Cited at pages 15 and 16)

[32] P. Hoff, O.C. Jonsson, E. Kugler, and H.L. Ravn. Release of nuclear reaction products from refractory compounds. *Elsevier*, 1984. (Cited at page 56)

[33] H. Holleck and H. Kleykamp. *Gmelin Handbook of Inorganic Chemistry*. Springer-Verlag Berlin Heidelberg GmbH, 8th. edition, 1987. (Cited at pages 44 and 45)

[34] B. Hy, N. Barré-Boscher, A. Özgümüs, B. Roussière, S. Tusseau-Nenez, C. Lau, M. Cheikh Mhamed, M. Raynaud, A. Said, K. Kolos, E. Cottereau, S. Essabaa, O. Tougait, and M. Pasturel. An off-line method to characterize the fission product release from uranium carbide-target prototypes developed for SPIRAL2 project. *Elsevier*, 2012. (Cited at pages 46 and 128)

[35] M.D.M. Innocentini, P. Sepulveda, and F. Ortega. *Permeability. In Cellular Ceramics: Structure, Manufacturing, Properties and Applications*. Wiley-VCH, Weinheim (Germany), 2005. (Cited at page 126)

[36] R. Kirchner. On the release and ionization efficiency of catcher-ion-source systems in isotope separation on-line. *Elsevier*, 1992. (Cited at pages 25 and 28)

[37] M. H. C. Knudsen. *The kinetic theory of gases; some modern aspects*. Methuen and Co., Ltd., London, 3rd. edition, 1934. (Cited at page 127)

[38] C. Koerner. Additive manufacturing of metallic components by selective electron beam melting: a review. *International Materials Reviews*, 2016. (Cited at page 113)

[39] U. Köster. Intense radioactive-ion beams produced with the ISOL method. *The European Physical Journal A (EPJA)*, 2002. (Cited at page 8)

[40] Karlheinz Langanke, Friedrich-Karl Thielemann, and Michael Wiescher. Nuclear astrophysicsand nuclei far from stability. In *The Euroschool Lectures on Physics with Exotic Beams, Vol. I*, 2004. (Cited at page 16)

[41] Mike Lawrence and Yunhong Jiang. *Porosity, Pore Size Distribution, Micro-structure*, pages 39–71. Springer Netherlands, Dordrecht, 2017. (Cited at pages 88 and 90)

[42] Po-Han Lee and Wan-Sheng Su. Calculated magnetism on Mn1-xFe_xB alloys. 2, 01 2017. (Cited at page 56)

[43] M. Santana Leitner. *A Monte Carlo Code to Optimize the Production of Radioactive Ion Beams by the* ISOL *Technique*. PhD thesis, 2005. (Cited at page 28)

[44] J. Lewis, J. Smay, J. Stuecker, J. Cesarano, and J. Cesarano. Direct ink writing of three dimensional ceramic structures. *Journal of the American Ceramic Society*, 12 2006. (Cited at page 114)

[45] J.A. Lewis. Direct ink writing of 3D functional materials. *Advanced Functional Materials*, 2006. (Cited at page 114)

[46] M. Manzolaro. *Study, design and test of the Target - Ion Source system for the* INFN SPES *facility*. PhD thesis, 2011. (Cited at pages 36 and 37)

[47] D. Mella. Sintesi di target refrattari ad elevata permeabilità per il progetto SPES, 2013. (Cited at page 128)

[48] Masahiro Notani. *Projectile fragmentation reactions and production of nuclei near the neutron drip-line*. PhD thesis, 2000. (Cited at page 23)

[49] H. Okamoto. C-Zr (carbon-zirconium). *Journal of Phase Equilibria*, 1996. (Cited at page 53)

[50] H. Okamoto. C-Ti (carbon-titanium). *Journal of Phase Equilibria*, 1998. (Cited at page 50)

[51] E. Parthé and J. T. Norton. Crystal structures of Zr_5Ge_3, Ta_5Ge_3 and Cr_5Ge_3. *Acta Crystallographica*, 1958. (Cited at pages 57 and 101)

[52] Hugh O. Pierson. *Handbook of refractory carbides and nitrides*. Noyes Publications, 1st. edition, 1996. (Cited at pages 42, 43, 50, 51, 52 and 54)

[53] M. Portillo, J. Nolen, I. Gomes, V.N. Panteleev, D.V. Fedorov, A.E. Barzakh, V.I. Beznosjuk, F.V. Moroz, S.Yu. Orlov, and Yu.M. Volkov. Production of neutron-rich isotopes by one- and two-step processes in ISOL targets. *Elsevier*, 2002. (Cited at pages 25 and 29)

[54] H.L. Ravn, T. Bjørnstad, P. Hoff, O.C. Jonsson, E. Kugler, S. Sundell, and B. Vosički. Use of refractory oxides and carbides and borides as targets for on-line mass separation. *Elsevier*, 1987. (Cited at pages 40 and 42)

[55] Michael D. Sacks, Chang-An Wang, Zhaohui Yang, and Anubhav Jain. Carbothermal reduction synthesis of nanocrystalline zirconium carbide and hafnium carbide powders using solution-derived precursors. *Journal of Materials Science*, 2004. (Cited at page 54)

[56] G.V. Samsonov. *Chemical properties and analysis of refractory compounds*. Consultants Bureau, 1st. edition, 1972. (Cited at page 57)

[57] D. Scarpa, L. Biasetto, S. Corradetti, M. Manzolaro, A. Andrighetto, S. Carturan, G. Prete, P. Zanonato, and D. W. Stracener. Neutron-rich isotope production using the uranium carbide multi-foil SPES target prototype. 2011. (Cited at pages 48 and 65)

[58] Chunsheng Sha, Liangcai Zhou, Shuhong Liu, Yong Du, Tie Gang, and Honghui Xu. Phase equilibria and thermodynamic modeling in the Ge-Zr binary system. *Journal of Materials Science*, 2011. (Cited at page 56)

[59] K.S.W. Sing, R.A.W. Haul D.H. Everett, L. Moscou, R.A. Pierotti, J. Rouquérol, and T. Siemieniewska. Reporting physisorption data for gas/solid systems with particular reference to the determination of surface area and porosity. *Pure and Applied Chemistry*, 1985. (Cited at pages 89 and 90)

[60] J.M. Smith, H.C. Van Ness, and M.M. Abbott. *Introduction to chemical engineering thermodynamics*. McGraw-Hills, 7th. edition, 2005. (Cited at page 30)

[61] E.K. Storms. *The refractory carbides*. Academic Press, 1967. (Cited at page 46)

[62] D.W Stracener, G.D Alton, R.L Auble, J.R Beene, P.E Mueller, and J.C Bilheux. Targets used in the production of radioactive ion beams at the HRIBF. *Elsevier*, 2004. (Cited at pages 40 and 41)

[63] Elisa Vettorato. Studio dello scambiatore ionico nanoatitanato per la purificazione di un radiofarmaco a base di ^{90}Y dal contaminante ^{90}Sr prodotto con tecnologia ISOL. (Cited at pages 12, 13 and 14)

[64] X. Wang, I. Loa, K. Syassen, R. K. Kremer, A. Simon, M. Hanfland, , and K. Ahn. Structural properties of the sesquicarbide superconductor La_2c_3 at high pressure. *American Physical Society*, 2005. (Cited at page 45)

[65] L. Winsberg. The determination of transfer times in an on-line isotope separator. *Elsevier*, 1971. (Cited at page 25)

[66] H. Yang, J. Gao, and H. Nakashima. Investigation of ZrGe schottky source/drain on n-Ge substrates. In *2014 12th IEEE International Conference on Solid-State and Integrated Circuit Technology (ICSICT)*, 2014. (Cited at page 57)

[67] Alice Zanini. Manifattura additiva di paste ceramiche, 2017. (Cited at page 117)

[68] Y. Zhang and G.D. Alton. Design of high-power ISOL targets for radioactive ion beam generation. *Elsevier*, 2004. (Cited at pages 30 and 35)